

UC Berkeley

UC Berkeley Electronic Theses and Dissertations

Title

Advances in Sustainable Cements

Permalink

<https://escholarship.org/uc/item/4n67v8d6>

Author

Hargis, Craig Wyatt

Publication Date

2013

Peer reviewed|Thesis/dissertation

Advances in Sustainable Cements

By

Craig Wyatt Hargis

A dissertation submitted in partial satisfaction of the

requirements for the degree of

Doctor of Philosophy

in

Civil and Environmental Engineering

in the

Graduate Division

of the

University of California, Berkeley

Committee in charge:

Professor Paulo J.M. Monteiro, Chair

Professor Claudia P. Ostertag

Professor Hans-Rudolf Wenk

Fall 2013

Abstract
Advances in Sustainable Cements
by
Craig Wyatt Hargis
Doctor of Philosophy in Civil and Environmental Engineering
University of California, Berkeley
Professor Paulo J.M. Monteiro, Chair

Concrete is crucial for infrastructure development and is the most widely used construction material in the world by mass. Concrete's use will only continue to increase as rapidly developing countries like India and China invest in their infrastructure and developed countries like the United States have to repair an aging infrastructure. However, the concrete industry accounts for 7-8% of the anthropogenic CO₂ emissions worldwide and the production of portland cement account for 5% of the anthropogenic CO₂ emissions. Anyone trying to improve the sustainability of concrete would do well to try and lower cement's environmental impact. Calcium sulfoaluminate cement is promoted as a sustainable alternative to portland cement because of its lower energy demand and CO₂ emissions during production. However, calcium sulfoaluminate cement is not as well studied as portland cement and it could potentially be made even more sustainable if more fundamental knowledge was known about it. For instance the expansive mechanism for calcium sulfoaluminate cement which can cause deleterious cracking and shortened life spans for structures is still debated and not fully understood.

This study utilized a wide variety of analytical, microscopy, and physical techniques to study calcium sulfoaluminate cement and its hydration reactions in order to more fundamentally understand the hydration reactions taking place and to determine calcium sulfoaluminate's elastic properties. High pressure X-ray diffraction was performed at the Advanced Light Source in the Lawrence Berkeley National Laboratory to determine calcium sulfoaluminate's bulk modulus and crystal structure. In-situ hydration reactions were followed using transmission X-ray microscopy at the Advanced Light Source. The hydration reactions were also monitored ex-situ with scanning electron microscopy, X-ray diffraction, and thermogravimetric analysis. The mechanical properties of the cement were studied with compression tests and dimensional stability bars.

The best fitting crystal structure for calcium sulfoaluminate was determined to be orthorhombic and its bulk modulus was calculated to be 69(6) GPa. Calcium sulfoaluminate was found to produce stellated structures during its hydration in dilute suspensions and it is hypothesized that the mechanical interlocking of adjacent stellated structures could contribute significantly to the strength of calcium sulfoaluminate cements. Calcium hydroxide was found to promote the formation of a poorly crystalline solid solution (SO₄²⁻/OH⁻) AFm on the surface of the hydrating calcium sulfoaluminate grains. This coating delays the formation of ettringite and is believed to play an important role in the expansion mechanism of calcium sulfoaluminate cement. Although calcium carbonate's low solubility prevent them from taking part in the early-age hydration reactions, calcite and vaterite did react with monosulfate to yield ettringite and monocarboaluminate. Vaterite was found to be approximately three times faster at converting monosulfate than calcite. Strength increases correlated in timing to the conversion of

monosulfate to ettringite and monocarboaluminate. Both calcite and vaterite were shown to decrease the set times of calcium sulfoaluminate cement and decrease the magnitude of expansion. Incorporating calcium carbonates into calcium sulfoaluminate cements appears to be very promising from both an environmental and performance standpoint. Particularly, if a cement plant could capture its CO₂ emissions and utilize them to make vaterite, the sustainability of the cement could be greatly advanced.

To my parents, Elaine and Terry Hargis, who always encouraged me to pursue my goals.
&
To my Wife, Jean Kim-Hargis, and daughter, Victoria Valentine Hargis, you are my moon and
stars that light up my path.

Contents

CHAPTER 1: INTRODUCTION	1
1.1 Need for Sustainable Cement.....	1
1.2 CSA Cement Development and C_4A_3S Crystal Structure.....	3
1.3 CSA Cement Properties	7
1.3.1 Hydration of CSA Cement.....	7
1.3.2 Dimensional Stability of CSA Cement	9
1.3.3 Mechanical Properties of CSA Cement	16
1.3.4 Durability of CSA Cement.....	17
1.4 Research Scope and Motivation.....	18
1.4.1 C_4A_3S Structure Evaluation and Bulk Modulus Determination	18
1.4.2 CSA Hydration in the Presence of Gypsum and Calcium Hydroxide.....	19
1.4.3 CSA Hydration in the Presence of Calcite and Vaterite with Varying Gypsum	19
CHAPTER 2: MATERIALS AND METHODS	20
2.1 Materials	20
2.1.1 C_4A_3S Structure Evaluation and Bulk Modulus Determination	20
2.1.2 C_4A_3S Hydration in the Presence of Gypsum and Calcium Hydroxide.....	20
2.1.3 C_4A_3S Hydration in the Presence of Calcite and Vaterite with Varying Gypsum.....	21
2.2 Methods.....	22
2.2.1 C_4A_3S Structure Evaluation and Bulk Modulus Determination	22
2.2.2 C_4A_3S Hydration in the Presence of Gypsum and Calcium Hydroxide.....	23
2.2.3 C_4A_3S Hydration in the Presence of Calcite and Vaterite with Varying Gypsum.....	27
CHAPTER 3: C_4A_3S STRUCTURE EVALUATION AND BULK MODULUS DETERMINATION	28
3.1 C_4A_3S Structure Evaluation	28
3.2 C_4A_3S Bulk Modulus Determination	29
CHAPTER 4: C_4A_3S HYDRATION IN THE PRESENCE OF GYPSUM AND CALCIUM HYDROXIDE.....	34
4.1 Dilute Suspension Experiments	34
4.1.1 Soft X-ray Microscopy	34
4.1.2 Scanning Electron Microscopy	38
4.1.3 X-ray Diffraction	44
4.2 Paste Experiments.....	45
4.2.1 X-ray Diffraction	45

4.2.2 Isothermal Conduction Calorimetry	48
4.2.3 Dimensional Stability.....	49
CHAPTER 5: C ₄ A ₃ \$ HYDRATION IN THE PRESENCE OF CALCITE AND VATERITE WITH VARYING GYPSUM.....	51
5.1 Early-Age Hydration.....	51
5.2 Mechanical Properties.....	53
5.3 Chemical Reactions	54
CHAPTER 6: CONCLUSION	58
REFERENCES	61

Figures

Figure 1: Perspective view of the pseudo-cubic sodalite cage	4
Figure 2: Backscattered electron images for the hydrated high $C_4A_3\$$ content CSA cement	14
Figure 3: Particle size distribution of the $C_4A_3\$$, CH, and $C\$H_2$ used in all experiments.	21
Figure 4: Two screw diamond anvil cell schematic.....	22
Figure 5: Transmission X-ray microscope schematic.....	24
Figure 6: Schematic of quantitative stereo SEM setup after [126].....	25
Figure 7: Comparison of calculated peak positions and intensities for a) cubic subcell [34], b) orthorhombic unit-cell [35], and c) tetragonal unit-cell [36].....	29
Figure 8: Ambient $C_4A_3\$$ X-ray powder diffraction pattern.	30
Figure 9: Integrated X-ray powder diffraction pattern for $C_4A_3\$$	30
Figure 10: Change in lattice parameters as a function of pressure.	31
Figure 11: Pressure dependent unit-cell volume change normalized to the ambient volume.	32
Figure 12: Normalized pressure, F, as a function of Eulerian strain, f.....	33
Figure 13: In-situ soft X-ray images of hydrating $C_4A_3\$$ particles	34
Figure 14: In-situ soft X-ray images of hydrating $C_4A_3\$$ particles plus 10% solid CH.....	37
Figure 15: Ex-situ secondary electron (SE) SEM images of hydrating $C_4A_3\$$ particles	38
Figure 16: Ex-situ SE SEM images of hydrating $C_4A_3\$$ particles plus 10% solid CH	39
Figure 17: EDS Spectrum of stellate ettringite cluster	40
Figure 18: Ex-situ SE SEM images of hydrating $C_4A_3\$$ particles plus 10% solid CH	40
Figure 19: Ex-situ SE SEM images of hydrating $C_4A_3\$$ particles plus 10% solid CH	41
Figure 20: Stereo pair of SE SEM images	42
Figure 21: Ex-situ SE SEM image of hydrating $C_4A_3\$$ particles plus 10% solid CH.....	43
Figure 22: Ex-situ SE SEM image of hydrating $C_4A_3\$$ particles	44
Figure 23: In-situ synchrotron X-ray diffraction recording the evolution of ettringite	45
Figure 24: X-ray diffraction patterns for hydrated pastes P0 - P10 from 0.5 h to 7 d.....	47
Figure 25: Influence of increasing CH on the initial rate of heat flow due to $C_4A_3\$$ hydration...	48
Figure 26: Influence of increasing CH on the rate of heat flow due to $C_4A_3\$$ hydration.....	49
Figure 27: Dimensional stability changes with CH content and curing condition.	51
Figure 28: Rate of heat evolution for $C_4A_3\$$ with varying replacements.	52
Figure 29: Dimensional stability of $C_4A_3\$$ with varying replacements.....	54
Figure 30: XRD results highlighting monocarboaluminate and ettringite formation.....	55
Figure 31: DTA results for specimens without $C\$H_2$ at 7 and 28 d.	57

Tables

Table 1: Comparison of cement composition and strength development for a variety of cements.	17
Table 2: C_4A_3 paste mix proportions.	26
Table 3: Initial unit-cell parameters for the crystal structures.	28
Table 4: Set times for C_4A_3 with varying replacements.	52
Table 5: Compressive strength development of mortar cubes with time.....	53
Table 6: Quantitative XRD results in percent.	56

Symbols

AFm	monosulfate
AFt	ettringite
CSA	calcium sulfoaluminate
DTA	differential thermal analysis
EDS	energy dispersive spectroscopy
GGBFS	ground granulated blast furnace slag
HAC	high alumina cement
HCP	hydrated cement paste
ICSD	Inorganic Crystal Structure Database
PC	portland cement
SCM	supplementary cementing material
SE	secondary electron
SEM	scanning electron microscope
TEM	transmission electron microscopy
TGA	thermogravimetric analysis
XRD	X-ray diffraction

AH ₃	Al ₂ O ₃ ·3H ₂ O
CA	CaO·Al ₂ O ₃
CA ₂	CaO·2Al ₂ O ₃
C ₃ A	3CaO·Al ₂ O ₃
C ₁₂ A ₇	12CaO·7Al ₂ O ₃
C ₂ AS	2CaO·Al ₂ O ₃ ·SiO ₂
C ₄ AF	4CaO·Al ₂ O ₃ ·Fe ₂ O ₃
C ₄ A ₃ \$	3CaO·3Al ₂ O ₃ ·CaSO ₄
CH	Ca(OH) ₂
C\$	CaSO ₄
C\$H ₂	CaSO ₄ ·2H ₂ O
C ₃ S	3CaO·SiO ₂
C ₂ S	2CaO·SiO ₂

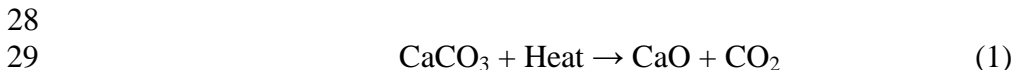
1 CHAPTER 1: INTRODUCTION

2 1.1 Need for Sustainable Cement

3 The earth continues to come under constantly heavier pressure from human activity as a result
4 of global population increases and industrialization in developing countries. Some of the threats
5 to the environment include: (1) eutrophication of streams, lakes, and oceans due to run off of
6 fertilizers and livestock manure, (2) acid rain, (3) poor air quality due to factory and vehicle
7 emissions, (4) deforestation, (5) depletion of fisheries, (6) collapse of coral reefs, (7) climate
8 change, (8) acidification of the oceans, (9) holes in the ozone layer, (10) species extinction and
9 (11) depletion of natural resources. As long as this list is, it is by no means exhaustive, and the
10 problems facing the earth will continue to grow until the global community adopts the concepts
11 of sustainable development.

12
13 With the current CO₂ concentration in the atmosphere being 398.58 ppm [1] up from the
14 preindustrial revolution value of 260-270 ppm [2] and projected to be above 800 ppm by the end
15 of the century without major changes causing deviations from current trends [3], all people and
16 industry need to reflect on their current behavior and activities to see where they can make
17 improvements and help reverse this trend. For civil engineers and society, the cement industry
18 is crucial to construction and infrastructure development. Concrete is the most widely used
19 construction material in the world by mass, and cement production accounts for approximately
20 5% of the anthropogenic CO₂ emissions, which is a sizable environmental footprint for a single
21 industry [4, 5].

22
23 Concrete is composed of approximately 12% portland cement (PC), 8% water, and 80%
24 aggregate [6]. Each tonne of PC produced consumes 4 GJ of energy and causes the release of
25 approximately one tonne of CO₂ into the atmosphere. Carbon dioxide is released from the PC
26 kiln because of the combustion of the fuel burned to keep the kiln at approximately 1450 °C and
27 due to the calcination (decomposition) of limestone in the kiln, see Eqn. 1.



29
30
31 In addition to the energy demand and CO₂ emissions associated with PC manufacturing, the
32 production of PC requires mining of non renewable natural resources, clay and limestone. The
33 result of these mining operations is generally a vast pit, which is generally partially abated by
34 flooding with water making an artificial lake and landscaping any exposed scars. Additionally
35 while the mine is in production, noise from blasting and heavy machinery, transient dust, and
36 kiln emissions which can contain heavy metals are environmental problems for the surrounding
37 communities. After the PC is manufactured it is transported to ready mix facilities, distribution
38 centers, and retail stores which adds to its environmental impact. Once at the mixing facility,
39 PC is combined with aggregate, supplementary cementing materials (SCM), water and chemical
40 admixtures to produce concrete. The components added to cement to make concrete also have
41 environmental impacts associated with them. The aggregate has to be mined and transported,
42 resulting in quarry scars, emissions, and nonrenewable resource depletion. Mix water is usually

43 taken from municipal drinking supplies and consequently has a substantial trade off cost and
44 energy cost associated with it. The true cost of the concrete industry on the environment is a
45 result of its scale. In 2010, the global concrete industry consumed approximately 3.7 billion
46 tonnes PC, 27 billion tonnes of aggregate, and 2.7 billion tonnes of mixing water [6]. In total,
47 the concrete industry including aggregate mining, materials transportation, and instillation
48 accounts for 7-8% of the anthropogenic CO₂ emissions.

49
50 Concrete does have some environmental benefits as well. For instance, many SCMs are
51 industrial byproducts that can be recycled into concrete preventing them from being dumped
52 into landfills or detention ponds where they can leach toxic heavy metals into the ground water.
53 Two examples of industrial byproducts that are used as SCMs are fly ash and ground granulated
54 blast furnace slag (GGBFS) which are byproducts of coal fired powered plants and steel
55 production, respectively. Additionally the hydration reactions of PC have been shown to
56 stabilize toxic heavy metals enabling the safe disposal of many toxic wastes [7].

57
58 PC is made from clay and limestone which upon firing combine to form new cementing phases.
59 The principal cementing phases in PC (given in cement chemistry) are alite (C₃S), belite (C₂S),
60 aluminat (C₃A) and ferrite (C₄AF). Cement chemistry utilizes a shorthand oxide notation (C =
61 CaO, S = SiO₂, A = Al₂O₃, F = Fe₂O₃, \$ = SO₃, H = H₂O). The hydration of C₃S provides PC
62 with the majority of its early strength gain. Unfortunately of the primary cementing phases, C₃S
63 requires the highest firing temperature and releases the most CO₂ during formation, so replacing
64 C₃S with an alternative phase that requires less energy and releases less CO₂ provides the
65 opportunity to make a more sustainable cement.

66
67 Calcium sulfoaluminat (CSA) cement is promoted as a sustainable alternative to PC because of
68 its lower energy demand and CO₂ emissions during production. Accordingly, academic and
69 industry research in CSA cement has experienced a renaissance because of its performance
70 advantages in special applications and its four main potential environmental and monetary
71 benefits. First, all phases in CSA cement can form and are stable at a temperature of
72 approximately 1250°C, which is about 100-200°C lower than PC clinker [8, 9]. The lower
73 formation temperature also lowers the energy requirement and CO₂ emissions from fossil fuel
74 burning. This saves money on fuel and could lead to additional savings if CO₂ is treated as a
75 pollutant and emitters are charged in the future. Second, CSA cement principally utilizes
76 C₄A₃\$¹ (Ye'elimate), instead of C₃S, as the primary early-age strength gaining phase and utilizes
77 C₂S to develop additional long-term strength. Of the major cement phases, C₄A₃\$ has one of the
78 lowest CaO contents. To illustrate the wide variation in CaO content in cement phases, the CaO
79 content by weight of several cement phases are listed: C₃S 73.7%, C₂S 65.1%, C₃A 62.2%,
80 C₄AF 46.2%, C₄A₃\$ 36.7%. C₄A₃\$'s low CaO contents makes it an attractive option for
81 developing a sustainable cement. The lower CaO content equates to a lower CaCO₃ demand in
82 the kiln, which results in less CO₂ emissions during calcination (Eqn. 1). Third, CSA clinker is
83 more friable than PC, due to high porosity; therefore, it requires less energy to grind [8].
84 Finally, CSA clinker can be manufactured from a wide variety of industrial byproducts
85 including: fly ash, flue gas desulfurization sludge, fluidized bed ash, blast furnace slag,

¹Cement chemistry notation used (C=CaO, \$=SO₃, A=Al₂O₃, F=Fe₂O₃, S=SiO₂, & H=H₂O)

86 phosphogypsum, incinerated municipal waste, red mud, and anodization muds [10-18].

87 **1.2 CSA Cement Development and C_4A_3S Crystal Structure**

88 CSA cement was first developed in the 1960s at the University of California at Berkeley by
89 Alexander Klein; consequently, C_4A_3S is often called Klein's compound [19-21]. CSA cements
90 have been used in China for approximately 40 years where they are referred to as the "third
91 cement series" with PC and calcium aluminate cements being the first and second cement series,
92 respectively [22-25]. Interest in CSA cements waned in Europe and the Americas after their
93 initial development; however, industry and the research community has renewed interest in
94 C_4A_3S bearing clinkers due to its many potential environmental and property benefits.

95
96 CSA clinker generally contains a high proportion of C_4A_3S , which can be accompanied by a
97 wide variety of other phases (C_3S , C_2S , C_4AF , $C\$, CA$, and $C_{12}A_7$) depending on the kiln feed
98 and operating conditions [26]. CSA clinker can be used to make cements with a variety of
99 properties including: high early strength, rapid setting, shrinkage compensating, or self stressing.
100 CSA clinker can also be blended with PC to make Type K cement, which is expansive. The
101 amount of expansion induced by CSA cement can be controlled by varying the water to cement
102 ratio (w/c), amount of calcium sulfate added, the particle size distribution, lime content, and the
103 C_4A_3S content [8, 27-29]. By varying cement phase proportions and the concrete mix
104 proportions a wide range of properties can be developed including: self stressing, shrinkage
105 compensating, non-expansive, rapid setting, and high early strength [8, 19, 20, 26-32].

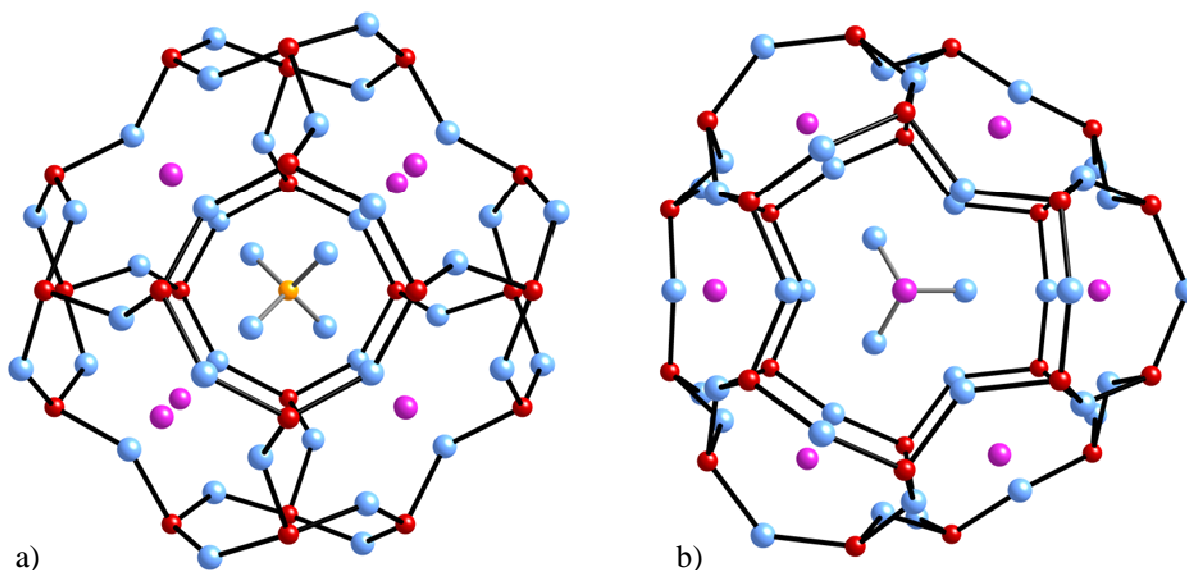
106
107 Although preliminary models for the structure of C_4A_3S have been developed, there is ongoing
108 research in this area due to the complexity of the structure. At the current time, it is unclear if
109 C_4A_3S is cubic [33, 34], orthorhombic [35], or tetragonal [36, 37], although there is a generally
110 well agreed upon cubic subcell with space group $\bar{I}43m$. In the following paragraphs, the work
111 that has been done to determine the structure of C_4A_3S will be discussed chronologically.

112
113 The synthesis of CSA was first reported by Ragozina in 1957 [38]. Ragozina prepared the
114 compound by heating tricalcium aluminate (C_3A) with gypsum ($C\$\text{H}_2$) at 1200°C; the
115 composition was reported as 1.6-3.6(CA)·C\$. In 1958 during the course of producing expansive
116 cements, Klein and Troxell reported composition estimates of C_5A_2S and $C_9A_4S_3$ [39]. They
117 produced their samples by firing CH or CaCO_3 , $C\$\text{H}_2$, and bauxite or aluminum sulfate at
118 1350°C. In 1961, Fukuda correctly identified the composition of C_4A_3S after firing bauxite,
119 lime, and $C\$\text{H}_2$ at 1350°C [40].

120
121 In 1962, Halstead and Moore suggested the cubic space group $I4_132$ for C_4A_3S , based on
122 systematic absences in their powder patterns [33]. They determined the refractive index to be
123 1.57 and the density to be 2.61 g/cm³. Additionally, they observe that all reflections that cannot
124 be indexed on a body-centered cubic cell ($a = 9.195$) are weak, and the strong reflections are
125 consistent with the space group $\bar{I}43m$. These observations suggested that C_4A_3S is an end
126 member of the sodalite ($\text{Na}_8[\text{Al}_6\text{Si}_6\text{O}_{24}]\text{Cl}_2$), noselite ($\text{Na}_8[\text{Al}_6\text{Si}_6\text{O}_{24}]\text{SO}_4$), hauynite ($[\text{Na,Ca}]_4$ -
127 $8[\text{Al}_6\text{Si}_6\{\text{O,S}\}_{24}[\text{SO}_4,\text{Cl}]_{1-2}$) series with all the Na^+ replaced by Ca^{2+} and the Si^{4+} replaced by
128 Al^{3+} .

129
130
131
132
133
134
135
136
137
138
139
140
141

Sodalites have the general formula $M_8(T_{12}O_{24})X_2$, where M is a relatively low charge caged cation (Na^+ , K^+ , Ca^{2+} , Sr^{2+} , etc...), T (usually Si^{4+} or Al^{3+}) is a cation, tetrahedrally coordinated with oxygen to form the framework, and X is the caged anion (either a single atom anion such as Cl^- or a tetrahedrally shaped oxyanion XO_4^{2-}) [41]. In C_4A_3S , the chemical formula denoting the aluminite sodalite structure is $Ca_8(Al_{12}O_{24})(SO_4)_2$. The excess charge of the framework, $(Al_{12}O_{24})^{12-}$, is charge balanced by the caged Ca^{2+} and SO_4^{2-} . Based on a pseudo-cubic cell of approx. 9 Å, the Al tetrahedra form 4 member rings in the $\langle 100 \rangle$ direction (Figure 1a) and 6 member rings in the $\langle 111 \rangle$ direction through corner sharing (Figure 1b). Figure 1 shows how Al-O bonds form the framework, Ca^{2+} tends to take up positions near the center of the 6-member rings, and the SO_4^{2-} tetrahedron resides in the center of the cage. Dangling and Ca-O bonds are omitted for clarity.



142
143
144
145

Figure 1: Perspective view of the pseudo-cubic sodalite cage. a) 4 member ring in the $\langle 100 \rangle$ direction and b) 6 member ring in the $\langle 111 \rangle$ direction. Al (red), Ca (purple), O (blue), and S (orange).

146 In 1965, Kondo ascribed the cubic space group $I23$ to C_4A_3S [42]; however, Fischer et al. [43]
147 state, “[T]he coordinates as given there conform completely to space group $\bar{I}43m$.” In 1972,
148 Saalfeld and Depmeier produced a crystal structure for the subcell based on the cubic space
149 group $\bar{I}43m$ [34], and they, like Halstead and Moore, explain the superstructure and weak
150 reflections by using the space group $I4_132$. Additionally, they proposed that the sulfate groups
151 rotate approximately 90° in alternating positions and the Ca^{2+} occupy 2 different positions among
152 the equipoints x,x,x and \bar{x},\bar{x},\bar{x} .

153
154
155
156

In 1991, Feng et al. [44] produced a single crystal of C_4A_3S by first firing calcite, alumina, and C_2H_2 at $1350^\circ C$ for 2 hours and then combining the resultant C_4A_3S with lead chloride in a ratio of 5:100. The mixture was then heated at $850^\circ C$ for 24 hours and $950^\circ C$ for 48 hours. This

157 seems like an unusually low temperature to produce a single crystal even with a flux since most
158 prior research produced C_4A_3S at approximately 1350°C. Feng et al. chose the same cubic space
159 group, $I\bar{4}3m$, as Saalfeld and Depmeier, but some atomic positions and calcium occupancy
160 factors differ. Feng et al. also reported two cubic, an orthorhombic, and a tetragonal
161 superstructure in their data.

162
163 Between 1990 and 1991, Wang et al. [45-48] published a series of transmission electron
164 microscopy (TEM) studies on C_4A_3S with much of their data interpretation being based on the
165 cubic crystal structure proposed by Feng et al. [44] who were coauthors of the TEM studies. The
166 studies propose explanations for multiple superstructures (orthorhombic, tetragonal, monoclinic,
167 and rhombohedral) by ordering the occupancy of the calcium atoms and performing image
168 simulations to test their hypotheses. They do not test the hypothesis of ordering the sulfate
169 groups in different orientations as proposed by Saalfeld and Depmeier [34] to explain the
170 superstructures. Wang et al. [46] showed a TEM image of C_4A_3S and mark a superstructure with
171 spacings of 1.4 nm, but the dark bands measured could be Moiré patterns [49]. They also
172 claimed to have found a new cubic phase with a lattice parameter of about 15 Å; they state,
173 “[Q]ualitative estimation of EDAX on this phase shows it has nearly the same composition as the
174 matrix.” Tricalcium aluminate (C_3A) can be an impurity phase when attempting to synthesis
175 pure C_4A_3S ; likewise, C_3A can be cubic and has a lattice parameter of 15.263(3) Å [50]. Last,
176 Wang et al. [48] presented multiple cases of twinning in C_4A_3S .

177
178 In 1992, two tetragonal structures were proposed for C_4A_3S , independently; however, they have
179 essentially the same lattice parameters of $a = 13.031$ Å and $c = 9.163$ Å [36, 37]. Peixing et al.
180 [36] used infrared spectroscopy to determine the tetrahedral coordination of aluminum and sulfur
181 and utilized electron diffraction to place C_4A_3S in the tetragonal crystal system. They determined
182 the space group to be $P\bar{4}c2$ and gave a full set of atomic positions. Their Fig. 4 shows ordering
183 of the caged sulfate ions, which breaks down the cubic symmetry. Krstanović et al. [37] give
184 possible space groups of $P4_1$ or $P4_122$ but do not give atomic positions.

185
186 In 1995, Calos et al. [35] published an orthorhombic crystal structure using space group $Pcc2$
187 and lattice parameters $a = 13.028(3)$, $b = 13.037(3)$, and $c = 9.161(2)$. They utilized infrared
188 spectroscopy, aluminum magic angle solid state nuclear magnetic resonance spectroscopy,
189 electron diffraction, and neutron diffraction to give evidence on the crystal structure. Moreover,
190 they utilized Depmeier’s probable symmetry breakdowns from the space group $I\bar{4}3m$ (which
191 describes the maximal symmetry of a collapsed aluminate sodalite cage) through the maximal
192 subgroups that result from symmetry reductions to select $Pcc2$ [51]. Likewise, the various
193 distortions that aluminate sodalites can undergo in order to accommodate various caged ions
194 were considered including: partial collapse and tilting of the alumina framework tetrahedra,
195 tetragonal orientation of the caged XO_4^{2-} anion, twinning (which Calos et al. did observe with
196 electron diffraction, as did Wang et al. [48]), and modulation of the structures [41]. Fischer et al.
197 [43] cast doubt on the orthorhombic space group $Pcc2$ proposed by Calos et al. [35] stating
198 “refinements with such large estimated standard deviations are unlikely to prove clearly
199 deviations from higher symmetry.”

200
201 In 1996 utilizing X-ray powder diffraction data, Ikeda et al. [52] performed a structure

202 refinement of C_4A_3 utilizing space group $I\bar{2}3$. They found an abnormally low density of 2.53
203 g/cm^3 (compare to 2.61 g/cm^3 [33]) and attributed the lower density to oxygen vacancies. Their
204 structural refinement resulted in the oxygen atoms in the Wyckoff positions 24f and 8c to have
205 occupancy values of 0.80 and 0.79, respectively; however, they do not offset the anion
206 deficiencies with cation deficiencies. Consequently, each of their unit cells has an excess
207 positive charge of 12.96. This result does not make physical sense and highlights the pitfalls
208 present in refinements.

209
210 Álvarez-Pinazo et al. [53], during their recent work using Rietveld quantitative phase analysis on
211 various CSA cements, state, “It is worth to highlight the importance of having accurate structural
212 descriptions for every phase in the cements to be analyzed.” Their work used two of the three
213 C_4A_3 crystal structures in the Inorganic Crystal Structure Database (ICSD), the cubic $I\bar{4}3m$
214 from Saalfeld et al. [34] and the orthorhombic $Pcc2$ of Calos et al. [35]. It is important to note
215 that the information in the ICSD for the space group c given by Saalfeld et al. is for the subcell,
216 and Saalfeld et al. actually propose the space group $I_4,32$ to explain the entire structure, which is
217 the same space group selected by Halstead et al. [33] which is not in the ICSD. Additionally, the
218 crystal structure from Saalfeld and Depmeier [34] in the ICSD is from 1972, and W. Depmeier
219 performed many studies that furthered the understanding of aluminat sodalites’ structures after
220 that initial work. Álvarez-Pinazo et al. [53] found that in their BCSAF_B2 sample (CSA cement
221 with iron and 2% boron oxide) the C_4A_3 phase was cubic, and “[They] speculate that this might
222 be due to the simultaneous presence of Na, Fe, and Si.” In the rest of their samples they found
223 that peak intensities in the XRD patterns could be attributed to a combination of cubic and
224 orthorhombic intensities. From a review on aluminat sodalites’ crystal structures, it is
225 improbable that a pure C_4A_3 would have a cubic structure at ambient temperature and pressure,
226 but with substitutions of larger caged ions for Ca^{2+} or SO_4^{2-} to expand the framework to a non-
227 collapsed state or with substitutions of smaller framework cations such as B^{3+} or Si^{4+} for Al^{3+} the
228 cubic symmetry could be restored. Ion substitutions are highly likely to occur in CSA clinker
229 produced from impure starting materials like what is found in commercial clinker production.
230 Additional resources for C_4A_3 synthesis and the structure of aluminat sodalites include [54-
231 59].

232
233 A note on synthesizing C_4A_3 . Many of the studies reviewed utilized $CaCO_3$, AlH_3 , or CSH_2 to
234 synthesize C_4A_3 ; however, hydrated or carbonated reagents will release H_2O or CO_2 when
235 heated, leaving behind porosity and hindering the sintering reaction; therefore, reagents should
236 be pre-fired before using them to synthesize C_4A_3 . Likewise, sulfate can volatilize during
237 firing, encouraging the formation of impurity phases such as C_3A . When possible, it would be
238 beneficial to either control the SO_x vapor pressure or use sealed containers to reduce the amount
239 of SO_x escaping. Reducing conditions should be avoided in the furnace as Brenchley and Weller
240 [60] showed that reducing conditions will convert the caged SO_4^{2-} tetrahedra to S^{2-} and restore
241 the cubic symmetry to $I\bar{4}3m$. Depmeier [41] gives some guidelines on how to grow adequately
242 large single crystals of aluminat sodalites utilizing a Bi_2O_3 flux; however, this technique proved
243 unsuccessful for C_4A_3 [W. Depmeier, Personal Communication, 11/27/2012]. Potential
244 candidates for an alternative flux include $Bi_2(SO_4)_3$, $VOSO_4$, or rare earth sulfates. A single
245 crystal XRD experiment of C_4A_3 is needed to confirm and/or determine the crystal structure, or
246 range of crystal structures, depending on the synthesis conditions and starting materials as

247 highlighted by Álvarez-Pinazo et al. [53].

248

249 Despite great effort put into the determination of C_4A_3S 's crystal structure by both
250 crystallographers and material scientists, the correct crystal structure for C_4A_3S has probably yet
251 to be determined. The uncertainty in the structure arises from nuances in the structure potentially
252 brought about by partial collapse and tilting of the alumina framework tetrahedra, tetragonal
253 orientation of the caged XO_4^{2-} anion, twinning, and modulation of the structures. These factors
254 affect the symmetries present in the crystal structure and hence affect the space group
255 determination. Although all of C_4A_3S 's symmetries are not known, the basic framework and
256 general positions of the charge balancing cations are fairly well understood as evidenced by the
257 agreement by the majority of the proposed crystal structures. The present research will further
258 elucidate which of the currently proposed crystal structures best fits experimental data.

259 **1.3 CSA Cement Properties**

260 **1.3.1 Hydration of CSA Cement**

261 CSA cements contain a significant fraction of synthetic ye'elimite (C_4A_3S). In fact, C_4A_3S is
262 chemically equivalent to three units of monocalcium aluminate (CA) plus anhydrous calcium
263 sulfate (C\$), and in most applications C_4A_3S plays roughly the same role in hydration as CA
264 does in high alumina cement (HAC). C_4A_3S has the advantage, however, that it is more
265 compatible with PC clinker phases at high temperatures and can thus be used to stabilize high-
266 alumina clinker compositions in the presence of calcium silicates under normal clinkering
267 conditions, thus permitting CSA clinkers to be manufactured in conventional rotary-kiln
268 systems as used for PC clinkers, which significantly reduces the manufacturing costs relative to
269 HAC.

270

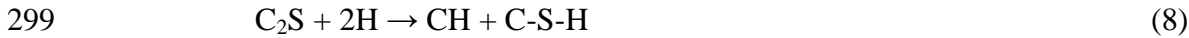
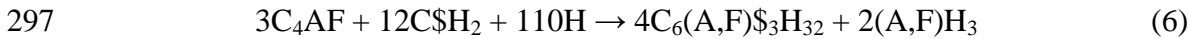
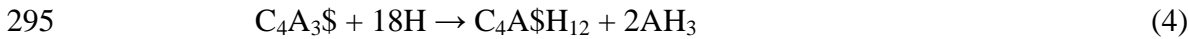
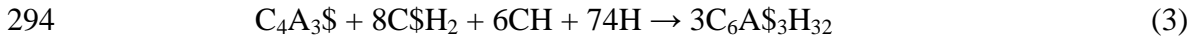
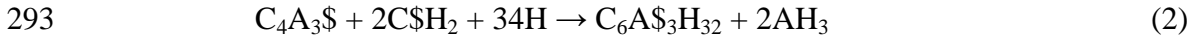
271 Depending on the CSA clinker composition, particle size distribution, w/c, and the amount of
272 $C\$H_2$ added, the CSA cement can have similar rheology, workability, set time, dimensional
273 stability, and strength gain to PC, or the CSA cement can be formulated to develop high early
274 strength, or to be shrinkage-compensating or self stressing [26-28, 31, 32].

275

276 It is well known that the most voluminous early hydration product in most CSA cement
277 formulations with $C\$H_2$ is ettringite ($C_6A_3H_{32}$). The hydration reactions of C_4A_3S with calcium
278 sulfates (C\$ and $C\$H_2$) initiates rapidly and forms ettringite and AH_3 , which contribute to the
279 early-age property development in CSA cement. In the absence of excess calcium hydroxide
280 (CH), crystalline ettringite is usually found together with smaller amounts of a largely
281 amorphous hydrated alumina gel (AH_3) [61, 62], see Eqn. 2. If both $C\$H_2$ and CH are present to
282 react with C_4A_3S , then hydration can produce ettringite without also producing AH_3 (Eqn. 3). CH
283 accelerates the hydration of C_4A_3S and produces a sulfate/hydroxy solid solution AFm phase at
284 early ages and ettringite at later ages (Eqn. 3) [63, 64]. When $C\$H_2$ is absent or depleted, the
285 formation of monosulphate ($C_4A\$H_{12-18}$) becomes the dominant reaction (Eqn. 4). The AH_3
286 produced during hydration can further react with additional CH and $C\$H_2$ to form ettringite
287 (Eqn. 5). Often Fe^{3+} is substituted for Al^{3+} in clinker phases and can play much the same role in
288 hydration as Al^{3+} . Eqn. 6 shows one such reaction for the hydration of C_4AF with $C\$H_2$. The
289 reaction of two other common CSA clinker phases are anhydrite (C\$) hydrating to form $C\$H_2$
290 and C_2S hydrating to form calcium silicate hydrate (C-S-H) which are Eqns. 7 and 8,

291 respectively.

292



300

301 PC manufacturers have used calcium carbonate (limestone, principally calcite) as filler for
302 decades. Limestone filler reduces the cost, energy demands, and CO₂ emissions associated with
303 cement production. Additionally, fine calcite benefits the cement in many ways, such as
304 increasing early age strength by providing nucleation sites, reacting with calcium aluminates to
305 form monocarboaluminate, imparting favorable rheological properties for the production of self
306 consolidating concrete, and stabilizing ettringite by favoring the formation of
307 monocarboaluminate instead of monosulfate [65-71]. Increasing the amount of limestone filler,
308 lowers the peak rate of heat evolution and the total heat evolved due to a decrease in the amount
309 of cement reacting [72]. Coarser grained limestone filler tends to delay the occurrence of the
310 main heat evolution peak; whereas, limestone filler that is significantly finer than the cement
311 advances the occurrence of the main heat evolution peak. Durability is directly linked to
312 permeability. Since many researchers have found limestone powder to act as a nucleation site,
313 this would have the effect of disrupting the pore continuity, consequently improving durability.
314 Schmidt found that portland limestone cements had slightly lower permeability than the
315 corresponding PCs [73]. Using mercury intrusion porosimetry, Sellevold et al. found that
316 cements containing a 12% limestone addition had a finer pore structure and slightly less total
317 porosity [74].

318

319 Calcite additions to PC can have some negative effects on PC. With calcite additions over
320 approximately 10% by mass, the strength of the blended cement begins to decline due to
321 dilutionary affects beginning to outweigh the nucleation benefits [75]. The addition of
322 limestone powder to PC can increase drying shrinkage as much as 15% [76]. In the past decade,
323 a lot of research has been done on the thaumasite form of sulfate attack. Unlike the classical
324 form of sulfate attack where hydration products are converted to ettringite and CSH₂ by the
325 ingress of sulfate ions, the thaumasite form of sulfate attack also requires carbonate ions. Due
326 to the higher solubility of carbonate ions at lower temperatures, thaumasite formation occurs
327 much faster at lower temperatures. Typically the carbonate ions came from carbonate bearing
328 aggregates and dissolved CO₂ in the water; however, when limestone powder is added to cement
329 an additional more soluble (due to higher surface area) source of carbonate ions is available.
330 This could make limestone addition to PC in cold environments very detrimental. Indeed,
331 Barker and Hobbs demonstrated that when portland limestone cement (Type I) is exposed to
332 sulfate and maintained at 5°C, ettringite and thaumasite are formed [77].

333

334 Calcite has also been shown to affect CSA cement (63% C₄A₃S, 8% CA, 3% CA₂, 18% C₂AS)
335 hydration and property development in many ways [70]. Fine calcite additions (46.9% of total
336 fines) generally reduce the set time and enhanced early age heat evolution in CSA cement.

337 Second, calcite promotes the formation of hemicarboaluminate and monocarboaluminate over
338 monosulfate. Finally, calcite additions to CSA cement promote higher compressive strengths at
339 later ages compared to quartz additions, which can be attributed to the calcium carbonate
340 reacting and reducing the porosity.

341
342 Many CSA cements give very rapid strength development, and, since ettringite is usually the
343 major hydration phase in the early-age microstructure, the question arises as to how this early
344 strength is generated. The strength of PC systems is generally ascribed to bonding by the C-S-H
345 phase, which like AH_3 , is largely amorphous. However, at early ages the AH_3 gel appears very
346 tenuous and seems unlikely to contribute significantly to strength; therefore, bonding and
347 interlocking between ettringite crystals probably makes the major contribution to the strength of
348 the CSA paste. In fact, many quite strong hydraulic cementing systems exist based entirely on
349 crystalline hydrates, for example: C_2H_2 plasters, HAC, magnesium phosphate cements, Sorel
350 cements, etc.

351 1.3.2 Dimensional Stability of CSA Cement

352 Due to the fast reacting C_4A_3 and the expansive nature of ettringite, CSA cements can be
353 manufactured with a variety of properties including: high early strength, rapid setting, shrinkage
354 compensating, or self stressing [8]. CSA clinker can also be blended with PC to make Type K
355 cement, which is expansive. The degree of expansion induced by CSA cement can be
356 controlled by varying the $3CaO \cdot 3Al_2O_3 \cdot CaSO_4$ content, amount of calcium sulfate added, the
357 particle size distribution, lime content, and the w/c [8, 27-29]. By varying cement phase
358 proportions and the concrete mix proportions a wide range of properties can be developed
359 including: self stressing, shrinkage compensating, non-expansive, rapid setting, and high early
360 strength [8, 19, 20, 26-32]. In field practices, CSA cements have been used mainly in pre-cast
361 concrete applications and cold environments and have shown good dimensional stability, low
362 permeability, low alkalinity, good durability, and comparable compressive strength to PC [78-
363 81]. However, despite the increasing interests in CSA cement, industrial scale production and
364 usage are mostly limited to China [82].

365
366 Since ettringite formation in PC has been linked to expansion and degradation in several forms
367 of sulfate attack including delayed ettringite formation and external sulfate attack [83, 84], the
368 dimensional stability and durability of any particular CSA cement formulation, which relies on
369 ettringite to provide early strength, needs to be extensively studied.

370
371 The formation of ettringite from the hydration reactions of C_4A_3 with calcium sulfates can be
372 expansive [62]. It has been suggested that if most of the ettringite forms before hardening, then
373 non-expansive and rapid hardening CSA cement can be achieved, but significant ettringite
374 formation after hardening can cause expansion and cracking [85]. Specific factors that have
375 been shown to affect expansion in CSA cements have been identified as: C_4A_3 content, pore
376 structure, w/c, sulfate content, free lime content, alkali hydroxide content, and particle fineness.
377 These factors are discussed in more detail next.

378
379 The phase assemblage in CSA clinker has been shown to affect expansion; specifically, higher
380 amounts of C_4A_3 have been linked to higher expansions. Beretka et al. [29] showed that CSA

381 cements containing mainly C_4A_3S , C_5S_2 , and C expanded and cracked with C_4A_3S contents
382 higher than 50% using a w/c of 0.4. These results agree with those of Janotka et al. [86] who
383 found that CSA cement with a low C_4A_3S content (20.2% C_4A_3S , 50.3% C_2S , 9.7% C , and
384 19.5% C_4AF) and a w/c of 0.5 had limited expansion (0.25%), although it expanded more than
385 PC mortar (-0.10%).

386
387 The effect of C_4A_3S content on expansion is mainly dependent on the amount of ettringite that
388 formed after cement hardened according to Equation 2, but the cement pore structure at the time
389 of ettringite formation also plays an important role [85, 87]. The cement pore structure affects
390 the mobility of ions and the amount of space for reaction products to form. It has been
391 suggested that the formation of ettringite confined to the vicinity of aluminum-bearing grains
392 results in large expansions [87]. Therefore, ettringite formation in pastes with denser pore
393 structures could cause more expansion. Bernardo et al. [88] showed that CSA cement that
394 contained a relatively high amount of C_4A_3S (53.0% C_4A_3S , 13.2% C_2S , 18.6% C , and 10.3%
395 $C_{12}A_7$) using a w/c of 0.5 hardened rapidly due to the fast formation of ettringite. The initial
396 hydration products quickly reduced the internal pore space. After 6 hours of hydration, the
397 smaller pores (~25 nm) dominated over the capillary pores (~200 nm) and the system developed
398 a bimodal pore structure, which generally correlates to a disconnected pore structure and a
399 denser microstructure. PC, on the other hand, showed a unimodal or continuous pore structure
400 at early ages, which generally correlates to a more porous microstructure. PC only developed a
401 bimodal pore structure after 7 days of hydration, demonstrating the disconnected nature of the
402 pore system as the larger pore volume decreased. These results suggest that the high C_4A_3S
403 cement examined by Bernardo et al. [88] should be expansive. While Bernardo et al. [88] did
404 not measure expansion on their specimens, the high C_4A_3S cements tested by Beretka et al. [29]
405 earlier would presumably have a similarly dense microstructure and these did expand. On the
406 other side of the spectrum, Janotka et al. [86] found that their low C_4A_3S content CSA cement
407 (20.2% C_4A_3S , 50.3% C_2S , 9.7% C , and 19.5% C_4AF) with a w/c of 0.5 had higher porosity
408 and coarser pore structure than PC mortar at 90 days of hydration and both were non-expansive,
409 as discussed earlier.

410
411 The w/c affects the amount of space (porosity) available for hydration product formation and the
412 amount of water available to hydrate the cement phases, both of which can alter expansion in
413 CSA cements. At lower w/c, the cement matrix develops a denser pore structure, which affects
414 the mobility of ions and the amount of space for reaction products to form that could lead to
415 expansive behavior in CSA cements, as discussed in the previous paragraph. Furthermore, at
416 lower w/c, high C_4A_3S -bearing CSA cements can undergo self-desiccation because the
417 formation of ettringite requires large amounts of water according to Equation 2 [8]. Therefore,
418 more cement particles remain unhydrated, even at later ages. Having large amounts of
419 unhydrated cement after setting can lead to expansion if the cement is later exposed to external
420 water from the environment, since unhydrated phases can react to form secondary ettringite.
421 Beretka et al. [29] tested a range of w/c with CSA cements that mainly contained C_4A_3S , C_5S_2 ,
422 and C . It was observed that when using a w/c of 0.4, the CSA cements with C_4A_3S content
423 higher than 50% expanded and cracked after curing in 100% relative humidity (RH). At w/c of
424 0.4, the initial water content was not enough for the large amount of C_4A_3S to completely react
425 according to Equation B2. Therefore, the secondary ettringite formed from the unhydrated
426 C_4A_3S and C during curing after the paste hardened combined with the denser pore structure

427 from the low w/c and high C_4A_3 content (more ettringite formation) resulted in the expansion
428 and cracking at later ages. However, when using higher w/c of 0.65-0.7, the high C_4A_3
429 cements remained dimensionally stable during curing in 100% relative humidity because water
430 in the system was sufficient for C_4A_3 to fully react at early ages and the microstructure is more
431 porous. It should be noted that secondary ettringite formation and associated expansion depends
432 on the curing environment [89]. When curing at low humidity, ettringite formation stops after a
433 few days of hydration due to the loss of free water in the system.

434
435 Dimensional stability of commercial CSA cement has been shown to be dependent on the
436 amount of C_2H_2 available in the system, with higher C_2H_2 contents linked to higher expansions
437 [8, 90]. Yanmou et al. [90] experienced ~0.15% and ~0.70% expansion with 15% and 35%
438 C_2H_2 , respectively, with a CSA clinker that contained 58.4% C_4A_3 and 11.6% C_2S . Glasser
439 and Zhang [8] showed that a different commercial CSA cement (unreported phase assemblage)
440 shrunk slightly at 18% C_2H_2 addition, showed zero dimensional change at 22-24% C_2H_2
441 addition, and became expansive at 24-25% of C_2H_2 addition.

442
443 Type K cements [91] contain CSA cement as an additive to PC and are designed to be
444 expansive. The degree of expansion in Type K cement has been linked to free lime content
445 (CaO in the PC clinker). While investigating Type K cements, Kurdowski and Thiel [92] found
446 that a cement containing 3.9% free lime produced much greater expansion than a low free lime
447 cement (0.8%). When the two pastes were examined in a scanning electron microscope (SEM)
448 at 1 and 7 days of hydration, the free lime accelerated the formation of ettringite but did not
449 appear to affect the size of the ettringite crystals. In contrast, Mehta [93] found that the
450 hydration of C_4A_3 in the presence of C_2H_2 and free lime resulted in ettringite crystals that were
451 significantly smaller than ettringite crystals formed from the hydration of C_4A_3 in the presence
452 of C_2H_2 only, suggesting a faster ettringite crystal formation rate when free lime is available.
453 The presence of free lime may make the reaction pathway in Equation 3 more favorable than the
454 reaction pathway of Equation 2; consequently, each unit of C_4A_3 would produce 3 units of
455 ettringite instead of 1. The larger amount of ettringite produced per unit of C_4A_3 in Equation 3
456 would result in a larger potential for expansion.

457
458 Alkali hydroxides have been shown to increase the dissolution rate of the aluminate phases in
459 PC [94], and Min and Mingshu [87] found that alkali hydroxides increased the expansion in a
460 sulfoaluminate cement, presumably through increasing the dissolution rate of C_4A_3 and
461 formation of ettringite.

462
463 Cement particles can remain unhydrated through means other than self-desiccation. If the CSA
464 cement contains high quantities of coarser particles, then those larger particles will be slow to
465 hydrate [95]. In Type K cements, the particle size of the C_4A_3 -bearing cement has been shown
466 to affect the amount and timing of the expansion [28]. When finer ground expansive Type K
467 clinker was added to PC, the C_4A_3 particles reacted faster with calcium sulfates to form
468 ettringite and the cement paste expanded at a high early rate for only a few days. However,
469 when coarser ground expansive Type K clinker was used, the C_4A_3 particles reacted slower
470 with calcium sulfates to form ettringite and the cement paste expanded at a slower rate for a
471 longer period of time, which led to abnormal behavior. The delayed expansion and strength
472 drop in coarser blends could be attributed to the formation of ettringite crystals on larger grains

473 of C_4A_3 after the C-S-H matrix had formed, which caused localized mechanical failures in the
474 matrix.

475

476 While previously discussed research identified variables that contribute to CSA cement
477 expansion, each study attributed expansion of the system to individual factors. Oftentimes
478 identifying the cause of expansion was not the goal of the research; consequently, factors
479 affecting expansion were not controlled in these studies. Also, many published studies do not
480 give the phase composition of the CSA cements tested. The results of the study discussed next
481 attempted to elucidate the interdependency of C_4A_3 content, particle fineness, w/c, and calcium
482 sulfate content and show how CSA cement expansion can be controlled by altering chemical
483 and physical factors in CSA clinker, cement, and pastes [27]. The results provide insights for
484 future usage of CSA cements as potential direct alternatives to PC in specialty applications.

485

486 Three CSA cements synthesized from reagent grade materials with different phase assemblages
487 were examined for dimensional stability in water and sulfate solutions. The reactions were
488 tracked using X-ray diffraction (XRD), and the microstructure development was observed
489 utilizing a SEM. Hydration product development showed that C_4A_3 and $C\$H_2$ reacted quickly
490 and contributed to the formation of ettringite and amorphous phases (mainly AH_3). Most of the
491 C_4A_3 and $C\$H_2$ reacted by 7 days of hydration. However, C_2S remained mostly unhydrated at
492 90 days of hydration in all the CSA cements.

493

494 The dimensional stability tests and companion XRD and SEM studies showed that expansion in
495 CSA cement increases with the following: (1) Increasing C_4A_3 content. As the C_4A_3 content
496 increases, the amounts of ettringite and amorphous phases (mainly AH_3) that can be formed
497 increase. The large store of “potential” ettringite and amorphous phases (mainly AH_3) that can
498 be formed increases the sensitivity of the cement to other factors that cause expansion. (2)
499 Decreasing w/c. As the w/c decreases, there is less space for the formation of hydration
500 products, including ettringite and amorphous phases (mainly AH_3). The expansive pressure
501 from ettringite increases when space is restricted. Also, since there is less water available for
502 hydration reactions, fewer hydration products can form prior to self-desiccation, which could
503 lead to expansion later when external water is supplied. (3) Increasing $C\$H_2$ content.
504 Increasing the amount of $C\$H_2$ provides the calcium and sulfate ions necessary for the
505 formation of ettringite and amorphous phases (mainly AH_3), increasing the amounts that can be
506 formed and the risk for expansion. (4) Increasing PSD. Coarser cement grains result in the
507 production of reaction rims around the hydrating C_4A_3 particles, confining the formation of
508 ettringite and amorphous phases (mainly AH_3) to around the surface of the hydrating grains,
509 resulting in localized expansion. Furthermore, since large grains hydrate slowly they can cause
510 expansion for a longer period of time. (5) Increasing sulfate content in the curing environment.
511 As more sulfate ions are available in the curing water, ettringite could form more rapidly and the
512 potential for expansion increases.

513

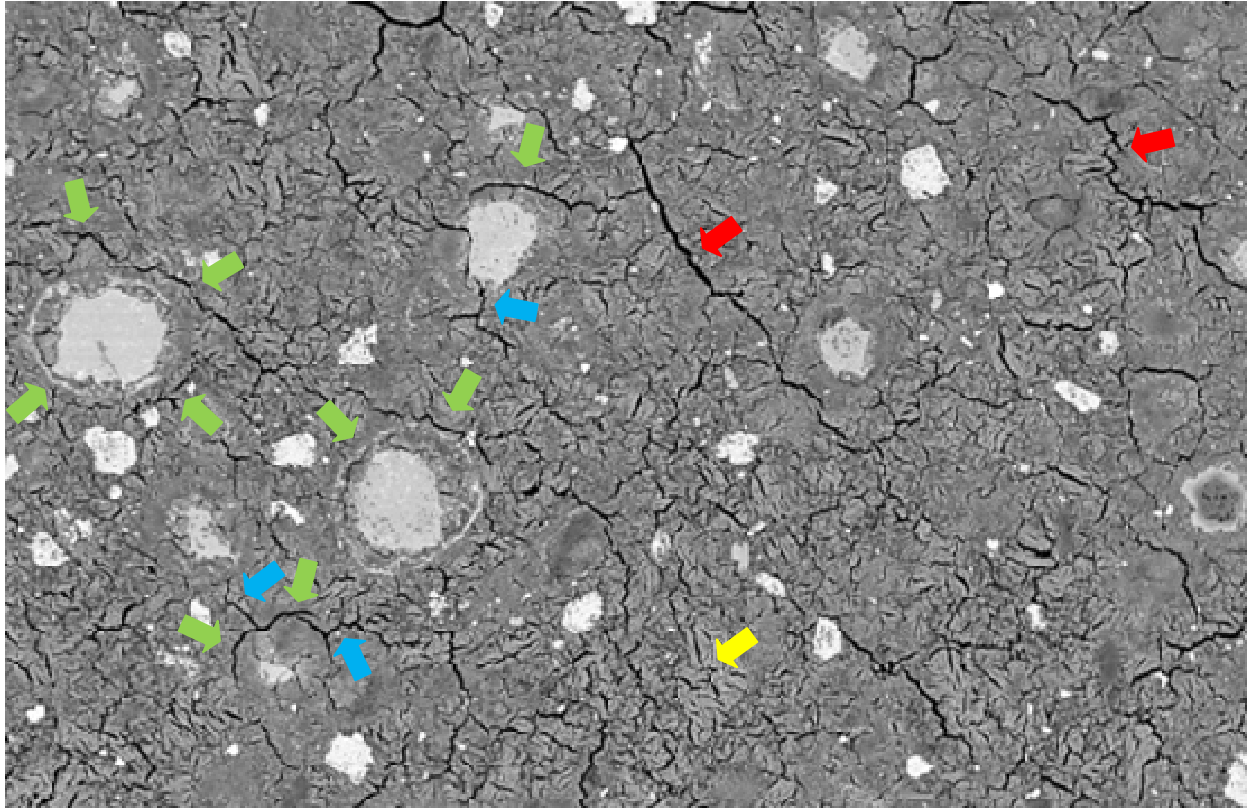
514 From the dimensional stability results presented in the study [27], the C_4A_3 content had the
515 most significant effect on CSA cements expansive behavior. However, expansion could be
516 mitigated even in high C_4A_3 content CSA cements when appropriate measures were taken
517 simultaneously. For example, providing enough initial internal water for the hydration reactions
518 provided more pore space for hydration products to form and prevented self-desiccation, adding

519 less $C_4A_3H_2$ reduced the formation of ettringite and amorphous phases (mainly AH_3), eliminating
520 exposure to high sulfate environments prevented free sulfate ions from entering the system that
521 could accelerate the formation of ettringite, and finally the most effective approach, reducing the
522 PSD of the cements prevented localized expansion around coarser $C_4A_3H_2$ particles. However, it
523 should be noted that increasing the w/c and reducing the $C_4A_3H_2$ content might adversely affect
524 other property development in CSA cements as the higher w/c results in a more porous
525 microstructure and the lower $C_4A_3H_2$ content prevents $C_4A_3H_2$ from reacting.
526

527 E.J. Garboczi quantified the stresses, displacements, and cracking around a single spherical
528 aggregate under different expansive conditions [96], and by analogy his results can be applied to
529 CSA cement expansion. To apply his results, one would need to consider the anhydrous $C_4A_3H_2$
530 core as the aggregate and then his results can be used to understand the microcracks that form
531 around hydrating $C_4A_3H_2$ cores. First, his results will be presented as applied to aggregates, and
532 then his results will be applied to CSA cement hydration. Garboczi presented three scenarios.
533 (1) Uniform matrix expansion, which includes the deleterious actions of certain kinds of sulfate
534 attack, freeze thaw, and hypothesized for delayed ettringite formation, results in tensile forces
535 that are their greatest at the aggregate-matrix interface. Consequently, the aggregate may break
536 free from the matrix leaving a circumferential gap or crack around the aggregate. In real
537 concrete systems, it is possible that some aggregates don't break free altering the stress field;
538 however, on average with uniform matrix expansion, gaps would be expected to form around
539 the aggregates that are approximately proportional to the radius of the aggregates. (2) A thin
540 expansive shell around the aggregate, which has been proposed as a mechanism for DEF
541 expansion, would also produce tensile radial stresses at the interface, causing the aggregate to
542 debond and form a rim of free space around the aggregate. In this case, however, the gap
543 produced is proportional to the thickness of the expansive rim and not the radius of the
544 aggregate. (3) Expansive aggregate, which could occur during alkali-silica reaction (ASR)
545 when the gel forms inside the aggregate, produces compressive radial stresses in both the
546 aggregate and the matrix, yet it produces tangential stresses that are compressive in the
547 aggregate and tensile in the matrix. As a consequence, radial cracks from the aggregate surface
548 into the matrix are expected. In real concrete systems where the aggregate is not expanding
549 uniformly then tensile stresses will also be produced within the aggregate causing cracking
550 inside the aggregate as well.
551

552 Figure 2 is a backscattered electron SEM image showing the typical crack patterns in CSA
553 cement and is adapted from Chen et al. [27]. The bright spots are the anhydrous $C_4A_3H_2$ cores.
554 Several different crack patterns can be observed and are highlighted by arrows of different
555 colors. The red arrows point out cracks that appear to have coalesced into macrocracks based
556 on their length and width compared to the other cracks in the field of view. The green arrows
557 mark cracks that are roughly circumferential or tangential and the blue arrows mark cracks that
558 are roughly radial from the $C_4A_3H_2$ cores. The yellow arrow points out cracks that are random in
559 nature and are typical of drying cracks that are common with ettringite shrinkage due to the loss
560 of free water. The circumferential/tangential cracks would indicate either bulk matrix expansion
561 or expansive shells around the $C_4A_3H_2$ cores. Reaction rims can be seen around the $C_4A_3H_2$ cores
562 that are microns to tens of microns thick. The radial cracking that is evidenced could be a result
563 of either drying shrinkage or from considering the reaction rim around the $C_4A_3H_2$ cores as a
564 zone that is expanding while new hydration products formed by the core reacting with water fill

565 any gaps that may have otherwise formed between the core and the reaction rim. It is possible
566 the small cracks are the former and the large cracks are the later.
567



568
569 Figure 2: Backscattered electron images for the hydrated high C_4A_3 content CSA cement from
570 [27]; field width: 1250 μm .

571 There are three predominant theories for the expansion mechanism in CSA cement: (1) crystal
572 growth theory [97], (2) swelling theory [97], (3) confined volumetric expansion theory (a name
573 I propose for the phenomena described by Scherer [98]). Historically, (1) and (3) have at times
574 been combined to varying degrees; however, here they will be separated to account for more
575 recent research, namely that of Scherer [98].
576

577 Crystal growth theory states that expansion is caused by the growth of ettringite crystals on the
578 surface of expansive particles (C_4A_3) or in the solution. The crystal growth is responsible for
579 the crystallization pressure and consequently the expansive force. The theory as applied by
580 Richards and Helmuth [99] states that the expansive cement is immediately covered by a dense
581 coating of ettringite and that further reaction proceeds topochemically increasing the thickness
582 of the coating layer. When the coating's thickness exceeds the surrounding solution's thickness,
583 then it will push other particles apart resulting in expansion. A micromechanical model was
584 developed to calculate geometrically the final magnitude of expansion. The expansion in the
585 model was dependent on the final thickness of the coating and the number of expansive sites.
586 The more expansive sites the lower the expansion. The chemical composition of the system,
587 w/c and particle size distribution affected the coating thickness and number of expansive sites.
588 Bentur and Ish-Shalom developed a very similar model relying on topochemical reaction but

589 instead of using a solid coating they utilized fine intermeshed crystallites of ettringite with pores
590 between the crystallites and instead of using a particle size distribution they utilized a single size
591 of expansive particles [100, 101]. Their model states that expansion initiates at a critical degree
592 of hydration occurring when hydrating spheres begin to come into contact and exert pressure on
593 each other causing expansion. Kalousek and Benton studied seawater attack on cement pastes
594 and concluded that it was ettringite crystals that grew in confined spaces and exerted pressure on
595 the surrounding walls that caused expansion [102]. Scherer showed that the stresses necessary
596 to crack cement paste (in the MPa range) could only be developed by crystals growing in the
597 nanometer pores under high supersaturation conditions [98]. Richards and Helmuth and Bentur
598 and Ish-Shalom's models are essentially geometrical in nature and assigning them the name of
599 crystal growth theory is perhaps unfortunate; since, many of the defenders of the theory simply
600 rely on the volume of the products being larger than the volume of the anhydrous expansive
601 cement and not on crystallization pressures. This concept will be further expanded when
602 discussing confined volumetric expansion a term developed to get away from this unfortunate
603 naming convention.

604
605 Mehta proposed a theory of expansion based on the uptake of water by ettringite which has been
606 called the swelling theory of expansion [103]. The theory relies on a through solution formation
607 of ettringite and that ettringite crystals formed in the presence of CH are gel-like and colloidal in
608 size. The large surface area of the colloidal ettringite adsorbs water causing swelling pressures.
609 In the absence of CH, C_4A_3S and C_3S will react to form ettringite that is large crystals have
610 less surface area and thus adsorb less water on their surfaces. To support this theory, Mehta
611 studied the microstructure of the reaction products of C_4A_3S with C_3S both with and without
612 CH [103]. The ettringite crystal formed in the presence of lime were about a $\frac{1}{4}$ μm wide and 1
613 μm long and without CH they were $\frac{1}{2}$ - 1 μm wide and 6 - 8 μm long. Mehta and Hu, also,
614 observed that the amount of water adsorbed correlated to increased expansion [104].

615
616 The confined volumetric expansion theory (a name proposed in the present work) simply relies
617 on the continued hydration of a confined anhydrous core after the formation of a rigid coating
618 and matrix has confined it [98]. The hydration products have larger volumes than their
619 anhydrous predecessors, so if hydration products are confined to form near the vicinity of the
620 anhydrous cores the localized volume increase will exert pressure on the confining matrix and
621 exert pressures that will eventually exceed the tensile strength of the hydrated cement paste
622 (HCP) matrix resulting in cracking and expansion. Ions would not be able to diffuse away into
623 open porosity if there were either (1) little to none open porosity, (2) discontinuous porosity, or
624 (3) the diffusion rate of water to the anhydrous core was more rapid than the diffusion rate of
625 ions away from the anhydrous core. Scherer makes the analogy of a water drop forming a
626 coating of ice and then the core of the water drop continues to freeze exerting pressure on the
627 confining ice around the core [98]. This is the phenomenon that creates the domes on top of the
628 ice in your freezer ice cube trays. The confined volumetric expansion theory relies only on
629 hydration of the confined core to cause a volume increase and expansion and does not rely on
630 crystallization pressure. However, that is not to say that crystallization pressure does not at
631 times contribute to expansion.

632 **1.3.3 Mechanical Properties of CSA Cement**

633 The mechanical properties of CSA cement can be altered by all the same variables that affect its
634 dimensional stability. Those variables are particle size distribution of the cement, curing
635 environment, w/c, clinker phase assemblage, and C₃H₂ addition level. In fact, all these same
636 variables affect PC strength development. A finer cement particle size distribution causes faster
637 strength gain because there is more surface area of the cement to react. Providing a proper
638 curing environment benefits any cement that utilizes hydration reactions to gain strength. A
639 proper curing environment can be achieved by either sealing in the moisture already present in
640 the hydrating cement paste with plastic or curing compounds, or even better by providing
641 external water by fogging, ponding, or covering with wet burlap. Without a proper curing
642 environment the cement paste dries out and the chemical reactions that take place with water
643 cease to occur and strength gain halts. A lower w/c increases strength by lowering the capillary
644 porosity. Since porosity cannot carry load reducing it results in a strength gain. However for a
645 given w/c ratio and degree of hydration, CSA cement will have a lower porosity than PC
646 because of the large volume of water consumed forming ettringite and monosulfate. In CSA
647 clinker, raising the C₄A₃ raises the early-age strength and increasing the C₂S raises the late age
648 strength. Increasing C₃H₂ content in the cement generally lowers the strength of the cement
649 [105]; however, C₃H₂ accelerates the hydration of CSA cements [106], so at early-ages CSA
650 cements with C₃H₂ would be expected to have higher strength. Rapid hardening cement can be
651 made with CSA clinker that has a high C₄A₃ (up to 70%) and utilizes 10-15% C₃H₂ [107].
652 The same cement could be made expansive (self stressing) by using 20-25% C₃H₂; however,
653 unrestrained expansive cements lose strength with time due to cracking, so adequate
654 reinforcement is required. Many different researchers have formulated CSA cements using
655 different formulations, feedstocks, burning conditions, and grinding schemes and the results of
656 their studies are just as varied, yet their results tend to follow the trends previously mentioned.
657 One such study [108] is here highlighted to illustrate how changes in the phase composition of
658 the cement can alter the strength development, see Table 1. Comparing the belite cement to the
659 belite CSA cement, it is clear that increasing the C₄A₃ content increases the early-age strength,
660 but the reduction in C₂S negatively affects the long-term strength. Additionally, changing from
661 C₂S to C₃S as the accompanying calcium silicate phase increases both early-age and late-age
662 strength in CSA cement. To produce C₃S bearing CSA cement, a CaF₂ mineralizer is necessary
663 to lower the firing temperature necessary to form C₃S below 1300 °C, since above that
664 temperature C₄A₃ decomposes.

665
666

667 Table 1: Comparison of cement composition and strength development for a variety of
 668 cements. Data from [108]

	PC	Belite Cement	Belite CSA	Alite CSA
Clinker Composition (%)				
C ₃ S	80	0	0	80
C ₂ S	0	80	60	0
C ₃ A	10	10	0	0
C ₄ A ₃ \$	0	0	20	10
C ₄ AF	10	10	20	10
C\$H ₂ Addition	3	3	7	5
Compressive Strength (MPa)				
1 d	22	9	21	35
3 d	50	12	27	59
7 d	73	23	29	77
28 d	82	35	33	86
365 d	85	96	78	102

669

670 1.3.4 Durability of CSA Cement

671 In the field, properly formulated CSA concrete has proven to be durable in regards to many of
 672 the chemical and physical attacks that it can undergo during service; however, CSA cement does
 673 perform more poorly than PC at times [78]. Like PC, CSA cement is susceptible to carbonation;
 674 however, CSA cement formulations that are higher in Fe and calcium silicates tend to perform
 675 better [26, 78]. During hydration, calcium silicates liberate CH and reduce the permeability of
 676 the HCP which helps slow carbonation. CH helps slow carbonation by reacting with CO₂ to
 677 form calcium carbonate which further densifies the paste since a unit of calcium carbonate
 678 occupies more volume than a unit of CH. Carbonation of ettringite yields calcium carbonate,
 679 C\$H₂, and alumina gel, resulting in a loss of strength [81, 109, 110]. Hydrated CSA cement's
 680 high ettringite content makes it more susceptible to carbonation and strength loss. Zhang et al.
 681 [78] showed strength losses of 2.5-7.1% for a variety of different CSA formulations after 28 d
 682 of accelerated carbonation (90% R.H. and 20% CO₂/80% Air).

683

684 Corrosion of steel reinforcing bars is a concern in CSA cement because CSA cements have a
 685 lower pH compared to PC; however, in practice CSA reinforced concrete has performed well
 686 [78]. The adequate corrosion resistance in CSA concretes has been attributed to its lower
 687 permeability compared to PC. Alkali-silica reaction has been shown to be worse in higher pH
 688 PC concrete, but due to its inherently lower pH, CSA concrete has not been shown to be
 689 susceptible to alkali-silica reaction [78, 107]. Additionally, CSA cement has been shown to be
 690 resistant to sulfate attack from seawater [78]. This can be attributed to the higher sulfate content
 691 initially present in CSA cements that causes the majority of the C₄A₃\$ to hydrate to form

692 ettringite leaving little monosulfate available to react with the sulfates from the seawater to form
693 ettringite, and hydrated CSA cement's lower CH compared to PC further reduces the quantity of
694 phases that are susceptible to sulfate attack. Any remaining anhydrous C_4A_3S would be
695 susceptible to attack and conversion to ettringite, but this can be overcome with grinding the
696 cement to a sufficient degree where little anhydrous C_4A_3S remains at later ages and by keeping
697 the w/c low enough to produce an impermeable HCP matrix. A durability concern and life-
698 safety issue with CSA cement is fire resistance. Upon heating to 120°C, ettringite loses its
699 bound water and turns amorphous, but its basic structural framework persists to approximately
700 400°C. Above 600°C, the amorphous calcium sulfoaluminate decomposes into C_4A_3S , CS, and
701 CaO [111]. In a high C_4A_3S bearing CSA cement, Su et al. [107] observed 15%, 45%, and 70%
702 strength losses upon heating to 100-150°C, 300°C, and 500°C, respectively.

703 **1.4 Research Scope and Motivation**

704 The literature review revealed that manufacturing PC consumes a lot of resources and places a
705 heavy burden on the environment through its CO₂ and other emissions and the geographic
706 footprints left behind by the mining operations. This study focuses on an alternative to PC,
707 CSA cement, in an effort to aid in the development and acceptance of a more sustainable
708 alternative to PC. Although CSA cement has been well studied, certain aspects of its hydration
709 and expansion mechanism are still not fully understood. Therefore, this work focused on those
710 aspects of CSA cement and also developed a way to make CSA cement perform better and be
711 more environmentally friendly by incorporating calcium carbonate into the cement blend. The
712 motivation behind the specific topics and how each of these topics is covered in detail is
713 discussed next.

714 **1.4.1 C_4A_3S Structure Evaluation and Bulk Modulus Determination**

715 As computational power of computers continues to grow, modeling of cementitious systems at
716 the microstructure scale will play an ever increasing role in cement and concrete research as
717 well as in the engineering of concrete structures, yet to utilize these models fundamental basic
718 parameters, such as bulk moduli, need to be determined for all the phases in the system.
719 Likewise, the growing interest in CSA cements warrants that more fundamental knowledge be
720 developed about this increasingly important material. A thorough literature review revealed
721 uncertainties about the correct crystal structure for C_4A_3S and determined that its elastic
722 properties were undetermined. To determine C_4A_3S 's bulk modulus, a high pressure XRD
723 experiment of C_4A_3S was performed at the U.S. Department of Energy's Advanced Light
724 Source (ALS) at Lawrence Berkeley National Laboratory. The determination of C_4A_3S 's elastic
725 properties is important to perform micromechanical models, particularly to determine the elastic
726 mismatch between the cement grain and the matrix. Enabling micromechanical modeling would
727 allow for previously presented expansion models to be validated or disproved ending a
728 longstanding debate and uncertainty among CSA cement researchers. Furthermore, enabling
729 micromechanical modeling would allow CSA cementitious systems to be formulated and
730 validated on the microscale which would allow more durable, sustainable, and high performance
731 systems to be engineered. C_4A_3S structure evaluation and bulk modulus determination will be
732 discussed in Chapter 3.

733 **1.4.2 CSA Hydration in the Presence of Gypsum and Calcium Hydroxide**

734 The hydration of CSA cement produces a much higher proportion of crystalline phases than
735 does the hydration of PC; consequently, understanding how poly-crystalline binder systems gain
736 strength is of the utmost importance in understanding how CSA cement develops strength.
737 Although, the subject of bonding in poly-crystalline hydraulic binders has been discussed in
738 some detail with respect to the properties of C_4A_3 based binders. How C_4A_3 hydration to
739 produce crystalline ettringite and monosulfate contributes to strength development is now well
740 understood. For the case of C_4A_3 plasters, it was suggested that the C_4A_3 crystals formed
741 initially from individual nuclei may bond together in preferred orientations at very early ages
742 when free rotation in the suspension can easily occur [112]. This study sought to determine
743 whether similar preferred orientations may develop in CSA cements and could contribute to
744 strength development. Such preferred crystal orientations are, however, very hard to observe by
745 the conventional techniques of scanning electron microscopy applied to dense hardened cement
746 pastes. This is because, due to the likely high porosity of such hypothetical domains, they may
747 well interpenetrate to a significant degree with other adjacent domains giving the impression of
748 a completely random microstructure. Therefore, the best chance to observe the formation of
749 preferred crystal orientations is probably at very early ages and/or in very dilute suspensions.

750
751 In this work, the hydration of C_4A_3 in dilute suspensions under conditions as close as possible
752 to those expected in CSA cements used for construction applications was studied utilizing wet
753 cells observed by transmission X-ray microscopy at the Advanced Light Source in the Lawrence
754 Berkeley National Laboratory. The reaction products from the dilute suspension were imaged
755 ex-situ as well using scanning electron microscopy to better understand any microstructure
756 domains that might develop and to improve the statistical significance of the findings by
757 allowing a larger number of sites to be observed than is practical at the Advanced Light Source.
758 Previous research has shown that CH both retarded the formation of ettringite and accelerated
759 the rate of heat release during C_4A_3 hydration. These two phenomena would seem to be at
760 odds with each other, so this study also sought to understand how both could occur
761 simultaneously. The transmission X-ray microscope allows in-situ imaging of the C_4A_3
762 hydration reaction and was utilized to provide visual evidence of how this dichotomy might
763 arise and to provide kinetic information about the reaction. Additionally, C_4A_3 pastes with
764 15% C_4A_3 and varying amounts of CH were investigated with isothermal conduction
765 calorimetry and XRD to better understand CH's effect on the hydration kinetics and hydration
766 products formed. The microstructural and product development during C_4A_3 hydration in the
767 presence of varying amounts of CH and what implications that has on CSA cement dimensional
768 stability will be discussed in Chapter 4.

769 **1.4.3 CSA Hydration in the Presence of Calcite and Vaterite with Varying Gypsum**

770 Although CSA cements are promoted as a more environmentally friendly alternative to PC, their
771 manufacture still consumes a large quantity of resources and energy. One way to reduce CSA
772 cement's environmental impact is to blend it with calcium carbonate. Prior research showed
773 that calcium carbonate additions also improved many of the hydration characteristics and
774 mechanical properties of the CSA cement as well [70]. The previous research used a CSA
775 cement with a mixed phase assemblage. The present study utilized a pure CSA clinker (C_4A_3)
776 to simplify the system and further elucidate the chemical reactions that occur. Additionally, the

777 current work sought to enhance the reactivity of calcium carbonate with CSA, both in the
778 presence and absence of C_2H_2 , by testing vaterite as well as calcite replacements of $\text{C}_4\text{A}_3\text{S}$.
779 Vaterite is a less stable form of calcium carbonate in ambient conditions; consequently, we
780 hypothesized it would be more reactive with $\text{C}_4\text{A}_3\text{S}$. Recently, Calera, a startup company in
781 California, has developed the ability to produce vaterite by combining a waste source of calcium
782 with the CO_2 exhaust from power plants [113]. In principal, this technology could be adapted to
783 capture the CO_2 from a cement kiln and produce vaterite on site, which could potentially
784 improve cement production's sustainability. The chemical reactions were monitored with XRD
785 and thermal gravimetric analysis (TGA). Dimensional stability and compressive strength were
786 tested on mortars to understand how the chemical reactions affected the mechanical properties.
787 $\text{C}_4\text{A}_3\text{S}$'s reaction with calcite and vaterite will be discussed in Chapter 5.

788 **CHAPTER 2: MATERIALS AND METHODS**

789 **2.1 Materials**

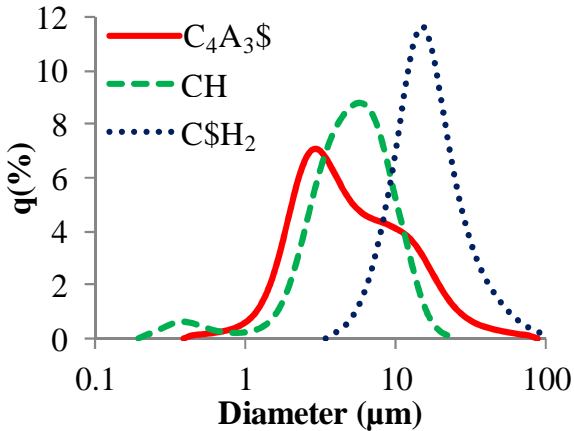
790 **2.1.1 $\text{C}_4\text{A}_3\text{S}$ Structure Evaluation and Bulk Modulus Determination**

791 $\text{C}_4\text{A}_3\text{S}$ was synthesized from a stoichiometric mixture of analytical grade (Fluka) calcite,
792 aluminum oxide, and C_2H_2 . The materials were homogenized with water, pelletized, then fired
793 in a laboratory kiln at $1,300^\circ\text{C}$ for 4 h. The $\text{C}_4\text{A}_3\text{S}$ was ground in an automatic agate mortar
794 grinder mill (Retsch RM100). The ground $\text{C}_4\text{A}_3\text{S}$ had a Blaine fineness of $5,520\text{ cm}^2/\text{g}$ and a
795 density of 2.60 g/cm^3 . The synthesized material was confirmed to be pure by XRD utilizing a
796 Panalytical X'Pert PRO Diffractometer with X'Celerator detector, goniometer radius of 240
797 mm, $\text{Cu K}\alpha_1$ radiation, step size of 0.017° , a dwell time of 24.765 sec/step, and a fixed
798 divergence slit of 0.25° . Using the extraction method [114], a free calcium oxide of 0.2 mass%
799 was determined.

800 **2.1.2 $\text{C}_4\text{A}_3\text{S}$ Hydration in the Presence of Gypsum and Calcium Hydroxide**

801 A sample of $\text{C}_4\text{A}_3\text{S}$ was obtained from Construction Technology Laboratories, Inc., Skokie, IL,
802 USA. It was synthesized by heating a stoichiometric blend of finely-ground reagent grade
803 alumina, calcium carbonate and calcium sulfate in an electric furnace at $1000\text{-}1100^\circ\text{C}$, followed
804 by quenching in air. After cooling, it was ground in a ceramic mill to pass a $75\text{ }\mu\text{m}$ (#200) mesh
805 sieve. Its particle size distribution was measured in an isopropyl alcohol suspension using a
806 Horiba Partica LA-950[®] Laser Diffraction Particle Size Distribution Analyzer. Refractive
807 indices of 1.568, 1.525, and 1.574 were used for $\text{C}_4\text{A}_3\text{S}$, C_2H_2 , and CH , respectively [115]. The
808 $\text{C}_4\text{A}_3\text{S}$ had a mean diameter of $6.9\text{ }\mu\text{m}$ with a standard deviation of $7.7\text{ }\mu\text{m}$ and 90% of the
809 particles had an effective diameter less than $15\text{ }\mu\text{m}$, see Figure 3.

810
811



812
813 Figure 3: Particle size distribution of the C₄A₃\$, CH, and C\$H₂ used in all experiments.

814 The phase-purity of C₄A₃\$ was confirmed by XRD, using a PANalytical XPert Pro[®]
815 diffractometer and by thermogravimetric analysis (TGA) using a TA Instruments[®] TGA, model
816 SDT 2960. Freshly boiled de-ionized water was mixed with reagent grade CH and C\$H₂ at
817 room temperature for 24 hours to make the solution used for all X-ray microscopy experiments.
818 The solution was then filtered twice [116]. To avoid carbonation, the solution was prepared and
819 stored in a glove bag filled with nitrogen gas [117]. To avoid silica contamination, which might
820 influence the hydration processes, only polyethylene or Teflon beakers, flasks, and pipettes were
821 used.

822 2.1.3 C₄A₃\$ Hydration in the Presence of Calcite and Vaterite with Varying Gypsum

823 C₄A₃\$ was synthesized from analytical grade chemicals, namely alumina, calcium carbonate,
824 and calcium sulfate dihydrate which were homogenized in a laboratory mixer. The three
825 compounds were proportioned assuming that (i) CaO, Al₂O₃, and CaSO₄ react to give only
826 C₄A₃\$ and (ii) solid solution effects were absent. The C₄A₃\$-generating mixture was heated in
827 an electric oven for 3 hours at 1250°C; the burnt product was then analyzed using XRD to study
828 the reacting system behavior in terms of conversion and selectivity towards C₄A₃\$. XRD results
829 revealed only the presence of C₄A₃\$, while reagents and/or secondary phases were absent. The
830 C₄A₃\$ was then further ground in an alumina shatter box until it passed a 45 micron sieve.
831 XRD also confirmed the calcite and C\$H₂ reagents to be pure, and the vaterite (Calera) was
832 found to be 92% vaterite and 8% calcite.

833
834 The particle size distributions of all reagents used to produce pastes and mortars were measured
835 in an isopropyl alcohol suspension using a Horiba Partica LA-950[®] Laser Diffraction Particle
836 Size Distribution Analyzer. Refractive indices of 1.378, 1.525, 1.580, 1.580, and 1.568 were
837 utilized for isopropyl alcohol, C\$H₂, calcite, vaterite, and C₄A₃\$, respectively [115]. The ground
838 C₄A₃\$ had a D₅₀ and D₉₀ of 4.1 and 13.5 μm, respectively. C\$H₂, calcite, and vaterite had D₅₀ of
839 14.6, 4.5, and 2.0 μm, respectively.

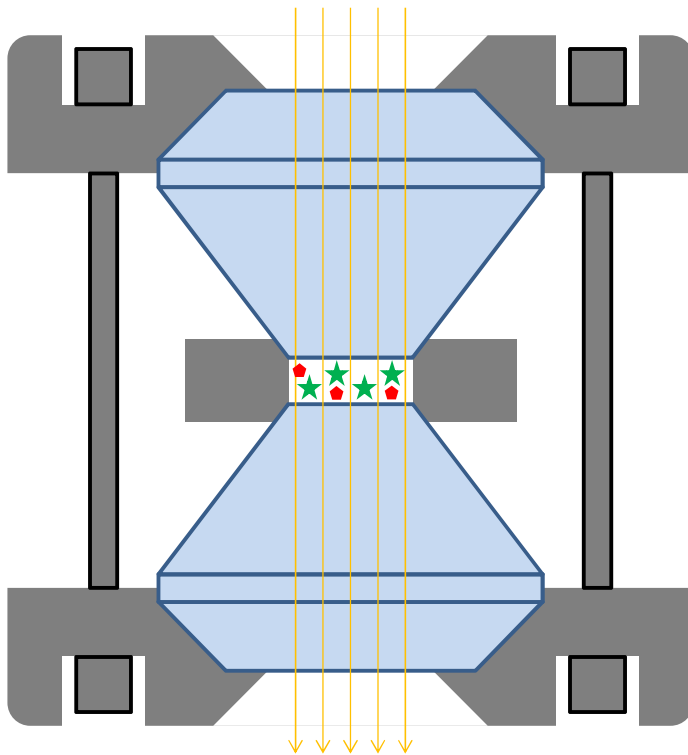
840

841 **2.2 Methods**

842 **2.2.1 C_4A_3 Structure Evaluation and Bulk Modulus Determination**

843 Using a synchrotron monochromatic X-ray beam, ambient and high pressure XRD experiments
844 were performed on beamline 12.2.2 of the Advanced Light Source of Lawrence Berkeley
845 National Laboratory [118]. The working distance between the sample and detector were
846 calibrated using the National Bureau of Standard's LaB_6 powder diffraction standard. A sample
847 to detector distances of 285.4270 mm and 282.6159 mm were utilized for the ambient and high-
848 pressure experiments, respectively. The X-ray wavelengths were 0.6199 and 0.4133 Å for the
849 ambient and high-pressure experiments, respectively. All patterns were collected on a MAR345
850 image plate with a 600 s exposure time.

851
852 The C_4A_3 was mixed with a silicone oil pressure medium (polysiloxane chains with methyl and
853 phenyl groups) and ruby [119]. The mixed sample was placed in the hole (180 μm diameter, 75
854 μm thickness) of a steel-gasketed two-screw diamond anvil cell which was used to generate the
855 high pressures and analyzed in axial geometry, see Figure 4. The schematic shows the X-rays
856 (orange arrows) first passing through a diamond anvil, then through mixture of the pressure
857 medium, ruby (red pentagons), and sample (green stars), then passing out of the second diamond
858 anvil before proceeding to the image plate. For each pressure, the sample pressure was allowed
859 to equilibrate for 20 min before collecting the pattern. The pressures ranged from ambient
860 (101.3 KPa) to 4.75 GPa. The ruby fluorescence technique was used offline to determine the
861 pressure [119]. The collected two-dimensional images were radially integrated using the Fit2D
862 program to produce 2θ vs. relative intensity plots [120].
863



864
865 Figure 4: Two screw diamond anvil cell schematic.

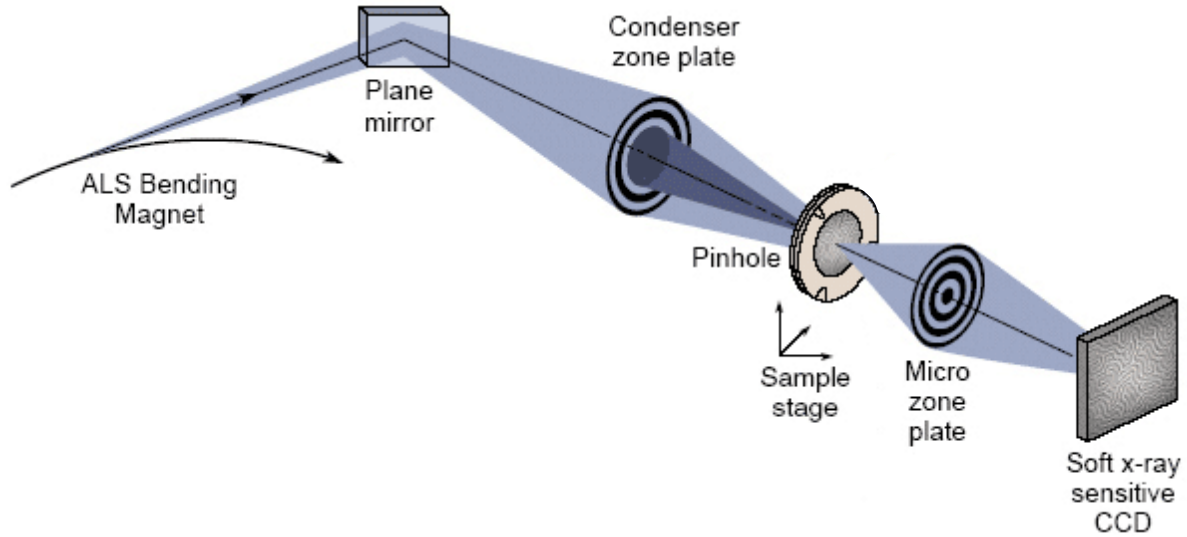
866
867 After radially integrating the diffraction patterns, the data was imported into the MAUD
868 program [121]. First, the LaB₆ pattern was refined to determine the diffraction instrument's
869 parameters. The first parameters were refined the background, scale, and anisotropic
870 temperature factors. Crystallite size and microstrain was set to 5,000 Å and 1.0E-5,
871 respectively, because the LaB₆ standard was known to have large crystallites and low
872 microstrains. Arbitrary texture was selected to provide a full Le Bail fit. Next, the detector
873 distance, center displacement in x and y, and tilting error in x and y were refined. Then, the
874 instrument broadening parameters (peak width, asymmetry, Gaussianity) were refined [122].
875 Wenk et al. [123] have a more detailed account of how to determine the instrument parameters
876 for synchrotron XRD experiments.

877
878 The instrument parameters were then fixed, and the high pressure XRD data was analyzed to
879 determine the lattice parameters. The background, scale, and lattice parameters were refined in
880 the range of 5 - 18° 2θ. The anisotropic thermal parameters were bound to 1 to avoid refining
881 to unreasonable values. Likewise, the lattice parameter b was constrained to be 1.00069x the
882 lattice parameter a, which was their ratio given by Calos et al. [35]. This was done to avoid the
883 refinement from arbitrarily changing the a or b lattice parameters (depending on which lattice
884 parameter began lower, it would be decreased and the other would be increased without the
885 constraint).

886 **2.2.2 C₄A₃\$ Hydration in the Presence of Gypsum and Calcium Hydroxide**

887 **2.2.2.1 Soft X-ray Microscopy**

888 Soft X-ray microscopy operating in the water window (between 2.34 and 4.40 nm photon
889 wavelength) combines a high lateral resolution (few tens of nm range) with the ability to
890 penetrate several μm of aqueous solution, which makes it an ideal in-situ technique to study wet
891 nanostructured materials. To allow for sufficient transmission of the soft X-rays a small droplet
892 of the suspension to be examined was placed in the sample holder, where it was squeezed
893 between two silicon nitride windows. Variations in window spacing account for most of the
894 variation in illumination time. The X-ray optical setup of the soft X-ray microscope, XM-1,
895 which is operated at the Advanced Light Source in Berkeley CA is illustrated in Figure 5 and is
896 described in more detail elsewhere [124]. All samples were analyzed three times with multiple
897 sites being observed per sample.
898



899

900 Figure 5: Transmission X-ray microscope schematic from [125].

901

902 The amount of time that each site was observed was kept to a minimum (~30-60s to focus) to
 903 limit introducing artifacts from the X-ray beam. No artifacts, such as accelerated dissolution of
 904 cement or hydration products or the formation of precipitates due to localized heating of the
 905 observation site, were observed in any of the experiments presented. Carbonation was not
 906 observed in any of the samples presented. The selected images presented in this paper
 907 summarize the behavior shown in all samples. Two different suspensions were investigated.
 908 Suspension one (S1) was prepared by adding 0.0400 ± 0.0001 g of C_4A_3 to 2.00 ml of the pre-
 909 saturated solution of C_2H_2 and CH, hand-mixing for 50 s and then centrifuging in an Eppendorf
 910 vial for 15 s to remove most of the particles larger than $5\mu\text{m}$ in diameter, so the suspension
 911 would fit between the windows of the microscope cell. In a second series of suspensions,
 912 suspension two (S2) was prepared by adding 0.0040 g solid CH to 0.0400 g of C_4A_3 to 2.00 ml
 913 of the pre-saturated solution of C_2H_2 and CH to assure that sufficient excess CH would be
 914 present during the early hydration, which essentially guarantees that no AH_3 will form and better
 915 simulates the conditions found at early ages in many real CSA cements such as ASTM Type K
 916 shrinkage-compensating cement.

917 2.2.2.2 Scanning Electron Microscopy

918 The scanning electron microscopy investigations used the same suspensions and mixing protocol
 919 as the soft X-ray microscopy investigations. The suspensions were then poured onto sample
 920 stubs and allowed to hydrate for 2 hours before being dried in a vacuum desiccator for 24 hours.
 921 The samples were then coated in Au or C depending on whether the samples were intended for
 922 topographic or spectroscopic investigations. The SEM used was a Zeiss EVO MA10[®]. Energy
 923 dispersive spectrometry (EDS) was conducted utilizing a 15-25 keV accelerating voltage and 1-2
 924 nA beam current. Quantitative stereo microscopy was conducted to make accurate length and
 925 angle measurements from the SEM images. Two images were taken of the same site with a 5°
 926 tilt angle difference, α , between the 2 images to create a stereo pair, see Figure 6. The electron
 927 beam was assumed to be moving parallel to the optic axis (Magnifications $\gg 100\times$), and eqs. (9)-
 928 (12) were utilized to determine the 3D positions of features from the 2D images where M is the

929 magnification, X_L denotes the X position on the left image, and uppercase letters (X_{3d} , Y_{3d} , Z_{3d})
 930 denote the 3D coordinates [126].

931

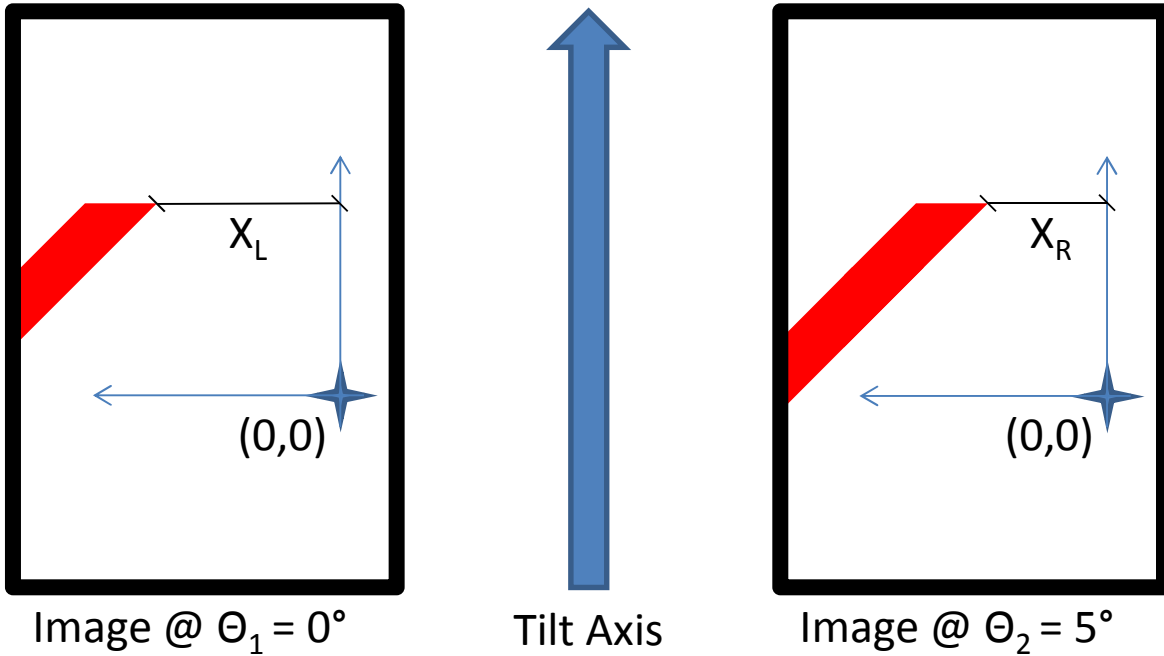
932 $P = X_L - X_R$ (9)

933 $M \cdot Z_{3d} = P / (2 \sin(\alpha/2))$ (10)

934 $M \cdot X_{3d} = X_L - P/2 = X_R + P/2$ (11)

935 $M \cdot Y_{3d} = Y_L = Y_R$ (12)

936



937

938 Figure 6: Schematic of quantitative stereo SEM setup after [126].

939 **2.2.2.3 In-Situ X-ray Diffraction**

940 In-situ XRD investigations on the suspension without excess CH (S1) were carried at the X-ray
 941 powder diffraction (XPD) beamline in the Brazilian Synchrotron Light Laboratory (LNLS) at
 942 Campinas, São Paulo, Brazil. The solution was mixed at LNLS then a capillary was filled with
 943 the liquid media and analyzed utilizing a X-ray wavelength of 1.5418 \AA in the angle ranges of 7°
 944 to $13^\circ 2\theta$ and 20° to $27^\circ 2\theta$, to follow the ettringite formation and the C_4A_3 peaks, respectively.
 945 The solution to solids ratio was lowered from 50 to 10 to generate a larger signal from the X-rays
 946 diffracting off the crystalline phases. The method was based on Dreele (2006) [127]. The X-ray
 947 source is a 1.67 T bending magnet of the LNLS ring operating at 1.37 GeV [128] with a typical
 948 initial average current of about 270 mA and 20 h lifetime. The critical energy of the emitted
 949 photons is 2.08 keV. The beamline operates in the energy range between 4.5 to 15 keV ($2.76 -$
 950 0.83 \AA) with a maximum horizontal acceptance of about 10 mrad. The X-ray optical setup of
 951 XPD is described elsewhere [129].

952 **2.2.2.4 Isothermal Conduction Calorimetry**

953 To better understand the effect of CH on C_4A_3 in the presence of C_2H_2 , pastes were prepared by
 954 mixing C_4A_3 with mass replacements of 15% C_2H_2 and 0, 1, 2, 5, or 10% CH. All C_4A_3

955 pastes were prepared with a water/solids (w/c) of 1, and when used as a comparison, PC pastes
 956 were produced from a Type I/II PC using a w/c of 0.5. Table 2 contains the five paste mix
 957 proportions. The paste mixes are labeled according to their CH content, such as P0 for the paste
 958 mix with 0% CH. Dry solids were first premixed to promote homogeneity. All pastes were
 959 hand mixed with a metal spatula for 2-3 min. All water used was de-ionized and de-aired.

960

961 Table 2: C₄A₃\$ paste mix proportions.

	0% CH		1% CH		2% CH		5% CH		10% CH	
	Wt (%)	Mol. Ratio	Wt (%)	Mol. Ratio	Wt (%)	Mol. Ratio	Wt (%)	Mol. Ratio	Wt (%)	Mol. Ratio
C ₄ A ₃ \$	85	1	84	1	83	1.00	80	1	75	1
CH	0	0.00	1	0.10	2	0.19	5	0.49	10	0.98
C\$H ₂	15	0.63	15	0.63	15	0.63	15	0.63	15	0.63
C / \$	2.8		2.9		3.0		3.1		3.4	
A / \$	1.8		1.8		1.8		1.8		1.8	

962

963 Pastes were tested for heat evolution using an isothermal conduction calorimeter (Thermometric
 964 TAM Air[®]). Two grams of solids, a w/c of 1, and internal mixing were utilized. The powders
 965 were dry mixed. Then the samples were placed in the calorimeter and allowed to equilibrate for
 966 48 hours, a 30 min. baselines were collected (<10μW/sample) before the mix water was
 967 injected, and the pastes were mixed for 2 min. via the injection ampoules. Hydration was
 968 evaluated for 9 hours at 23°C.

969 **2.2.2.5 X-ray Diffraction**

970 C₄A₃\$ pastes were prepared in the aforementioned manner in a nitrogen glove box to prevent
 971 carbonation and were kept sealed in Eppendorf vials until hydration was stopped by grinding in
 972 an excess of acetone. Hydration was stopped at 30 min., 1 h, 2.5 h, 1 d, and 7 d. XRD patterns
 973 were collected on a PANalytical X'Pert PRO with X'Celerator[®] position sensitive detector
 974 operating at 40 kV with 40 mA using a cobalt target (Co K α wavelength 1.79 Å) and an iron
 975 filter. Scans were collected from 5–75° 2 θ at a 0.6°/min scan rate.

976 **2.2.2.6 Dimensional Stability**

977 C₄A₃\$ pastes were prepared in the aforementioned manner and cast into bars (1x1x4 cm) with
 978 steel gauge studs in there ends. The polycarbonate molds were filled in two lifts tamping each
 979 lift approximately 25 times. After tamping, the excess was screeded off, the molds were
 980 covered with polyethylene film and placed in a room at 100% R.H. at 23°C. After 24 hrs, the
 981 paste bars were demolded and placed in 100 ml of deionized water. The samples were then
 982 measured daily for length changes. After 10 days of hydration the samples were allowed to air
 983 dry for 10 days and then were reimmersed in water, in order to determine the effects of a drying
 984 and rewetting cycle on the paste bars.

985 2.2.3 C₄A₃\$ Hydration in the Presence of Calcite and Vaterite with Varying Gypsum

986 The study utilized six mixes proportioned by weight where the mass of C₄A₃\$ was replaced by
987 percentages of C\$H₂ and calcite or vaterite. A naming convention was adopted to quickly
988 identify each sample where C4A3\$ was followed by the first letter of the reagent replacement
989 and its mass percent replacement. Note that the sample names are not subscripted to help
990 indicate them as samples and differentiate them from C₄A₃\$ as a material. For instance, the
991 sample C4A3\$ would be 100% C₄A₃\$, and the sample C4A3\$_G15_C10 would be 75% C₄A₃\$,
992 15% C\$H₂, and 10% calcite respectively. The six reagent proportions used in the study are
993 C4A3\$, C4A3\$_C10, C4A3\$_V10, C4A3\$_G15, C4A3\$_G15_C10, and C4A3\$_G15_V10.

994
995 Mortar samples were made using a sand to cementitious material ratio of 2.75 and a water to
996 cementitious material ratio (w/cm) of 0.5. Mortars were mixed by hand in a polyethylene cup
997 with a metal spatula for 1.5 min. on a vibration table. The sand and reagents were premixed to
998 better ensure homogeneity. The mortars were placed into molds in two lifts and tamped with a
999 2 x 6 mm cross section tamper, then vibrated for 15 s. After molding, the samples were covered
1000 with plastic film and placed in a room at 23°C and 100% R.H. After 24 hrs, the samples were
1001 demolded. For compression tests, the mortars cubes (1.27 cm [0.5 in.]) were stored at 23°C and
1002 100% R.H. with a bell shaped dome over them to minimize dripping on the samples and a
1003 plastic 1.2 cm plastic grid under them to ensure constant humidity. Ten mortar cubes per mix
1004 per testing date were tested in compression utilizing a loading rate of 0.34 MPa/s (50 psi/s).
1005 Compression tests were conducted at 1, 7, 28, and 84 d of hydration. For dimensional stability
1006 tests, mortar bars (1x1x4 cm) were cast simultaneously with the mortar cubes and were prepared
1007 utilizing the same procedure. The mortar bars were cast with threaded bars in their ends, so a
1008 comparator could be utilized to measure their length change with time. Three mortar bars were
1009 prepared for each mix. After 24 hrs of hydration, the mortar bars were demolded, initial length
1010 measurements were taken, and the bars were stored in 50 ml of deionized water in sealed glass
1011 jars until subsequent measurements. For set time, the same mortar compositions used in the
1012 compression and dimensional stability tests were tested using a modified version of ASTM
1013 C807 [130]. Initial set was taken to be a 10 mm penetration of the needle and final set was
1014 considered to be when the needle no longer left an impression on the mortar surface.

1015
1016 Pastes for the six mixes were prepared using a w/cm of 0.5 and were kept sealed in Eppendorf
1017 vials. Reagents were premixed dry and then mixed with water for 1 min in the vial using a
1018 metal spatula. After 1d, 1 ml of water was placed on top of the samples and then the samples
1019 were resealed. This was done to ensure adequate water was available for hydration. Hydration
1020 was stopped at 1, 7, 28 and 84 d by grinding in an excess of acetone. The acetone was then
1021 removed by vacuum. XRD patterns were collected on a PANalytical X'Pert PRO with
1022 X'Celerator[®] position sensitive detector operating at 40 kV with 40 mA using a cobalt target
1023 (Co K α wavelength 1.79 Å) and an iron filter. Scans were collected from 5–75° 2 θ at a
1024 0.6°/min scan rate. XRD results were quantified using the software X'Pert HighScore Plus[®].
1025 The scale factors, sample displacement, 2 θ shift, and cell parameters were refined for
1026 quantification. The pastes were also studied with Thermogravimetric (TGA) and differential
1027 thermal analysis (DTA) from 30 to 1000°C at a heating rate of 20°C/min.

1028

1029 Pastes were tested for heat evolution using an isothermal conduction calorimeter (Thermometric
 1030 TAM Air[®]). Four grams of solids and a w/cm of 0.8 were utilized to provide ample signal.
 1031 Before mixing 30 min. baselines were collected (<10 μ W/sample). The reagents were dry
 1032 mixed, then mixed for 2 min. externally. A larger sample mass, a w/cm of 0.8, and external
 1033 mixing were utilized because internal mixing with 2 g of solids and a w/cm of 1 was giving
 1034 inconsistent results which we believe arose from some difficulties in getting the vaterite to
 1035 disperse homogenously and not settle with internal mixing. Hydration was evaluated for 48 hrs
 1036 at 23°C.

1037 **CHAPTER 3: C₄A₃S STRUCTURE EVALUATION AND BULK MODULUS** 1038 **DETERMINATION**

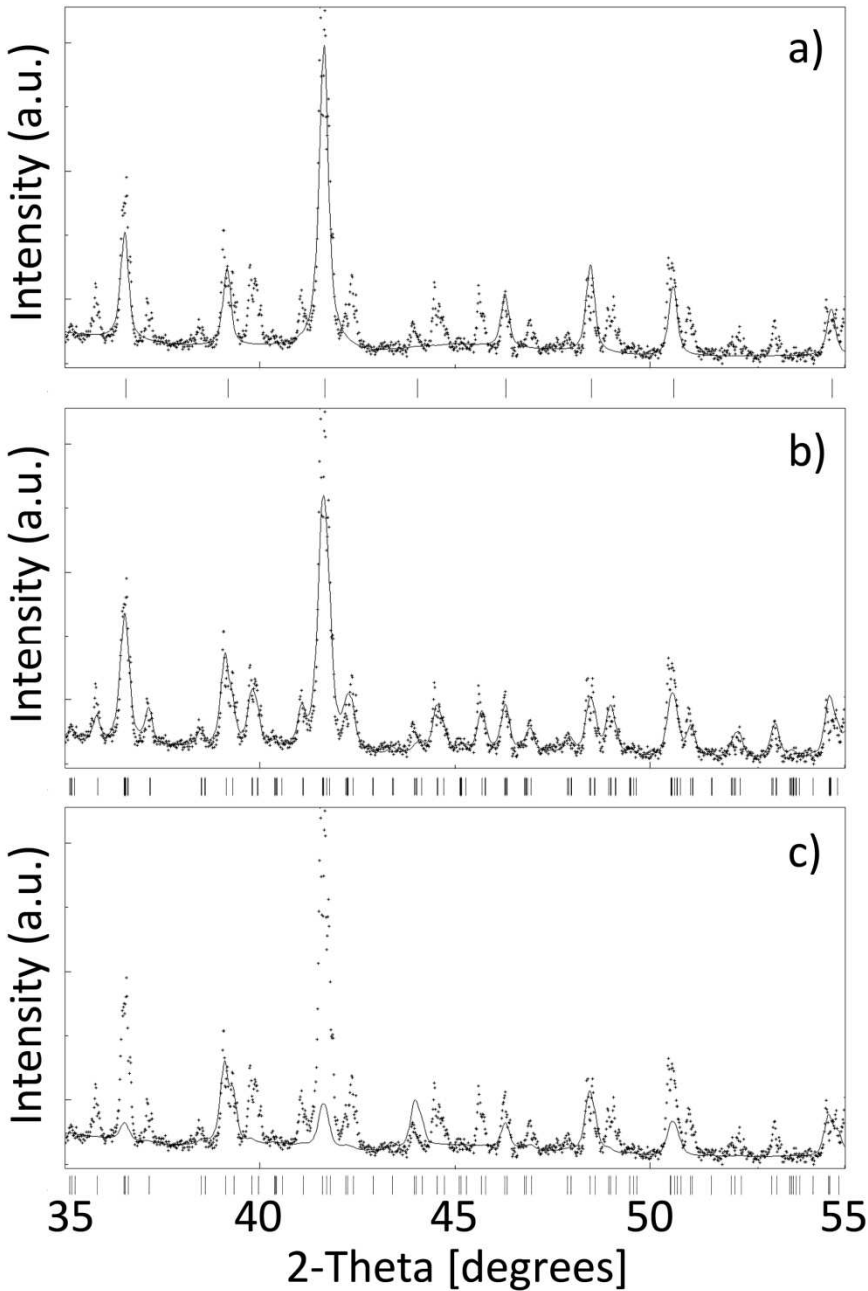
1039 **3.1 C₄A₃S Structure Evaluation**

1040 To determine how well the cubic subcell [34], orthorhombic unit-cell [35], and tetragonal unit-
 1041 cell [36] (Table 3) describe the synthesized C₄A₃S, Rietveld refinements were performed (Fig.
 1042 A2) using the MAUD program [121], and the only parameters refined were the background,
 1043 sample displacement, X-ray intensity, and lattice parameters. Only varying these parameters
 1044 allows the merit of a few of the published crystal structures to be evaluated. The cubic subcell
 1045 with space group $\bar{I}43m$ was selected instead of the full cubic unit cell because atomic positions
 1046 are not given for the space group I₄32. Figure 7 illustrates how many of the weaker reflections
 1047 (superstructure reflections) are not produced by the cubic subcell crystal structure. Comparing
 1048 Figure 7b and Figure 7c, one can see that both the orthorhombic and tetragonal crystal structures
 1049 produce reflections at all the observed peaks, but the orthorhombic crystal structure does a much
 1050 better job of matching the observed peak intensities. Consequently, the orthorhombic crystal
 1051 structure of Calos et al. [35] appears to be the most accurate crystal structure, presently
 1052 proposed, for C₄A₃S. This result is not unexpected since Calos et al. considered the probable
 1053 symmetry breakdowns from the space group $\bar{I}43m$ (which describes the maximal symmetry of a
 1054 collapsed aluminate sodalite cage) through the maximal subgroups that result from symmetry
 1055 reductions to select Pcc2 [51]. Likewise, they took into account the various distortions that
 1056 aluminate sodalites can undergo in order to accommodate various caged ions including: partial
 1057 collapse and tilting of the alumina framework tetrahedra, tetragonal orientation of the caged
 1058 XO₄²⁻ anion, twinning, and modulation of the structures [41].

1059
 1060 Table 3: Initial unit-cell parameters for the crystal structures.

Cubic [34]		Orthorhombic [35]				Tetragonal [36]		
a (Å)	Space Group	a (Å)	b (Å)	c (Å)	Space Group	a (Å)	c (Å)	Space Group
9.20	$\bar{I}43m$	13.028	13.037	9.161	Pcc2	13.031	9.163	$\bar{P}4c2$

1061



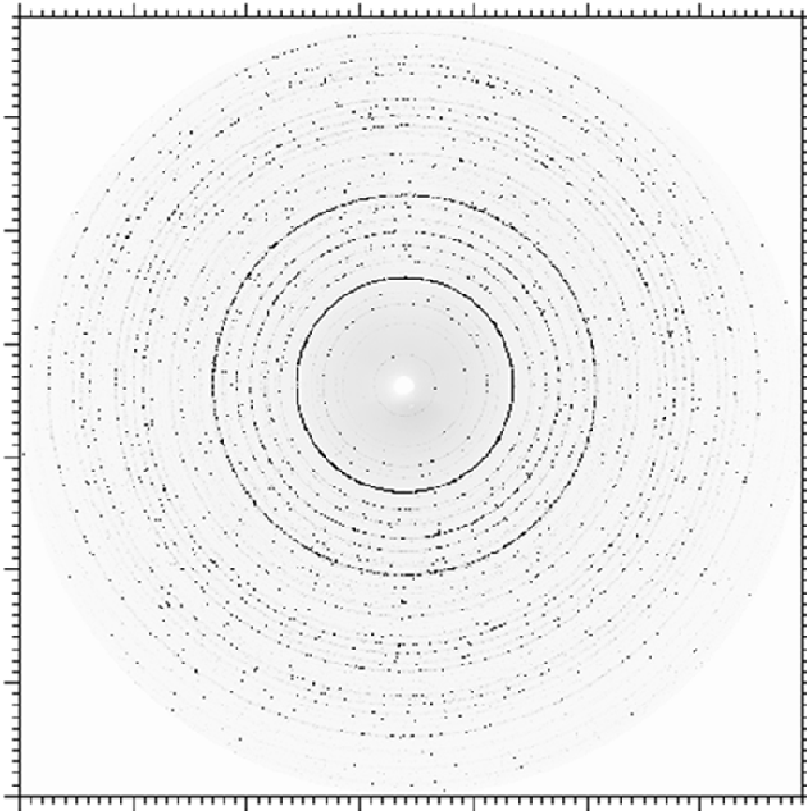
1062

1063 Figure 7: Comparison of calculated peak positions and intensities for a) cubic subcell [34], b)
 1064 orthorhombic unit-cell [35], and c) tetragonal unit-cell [36].

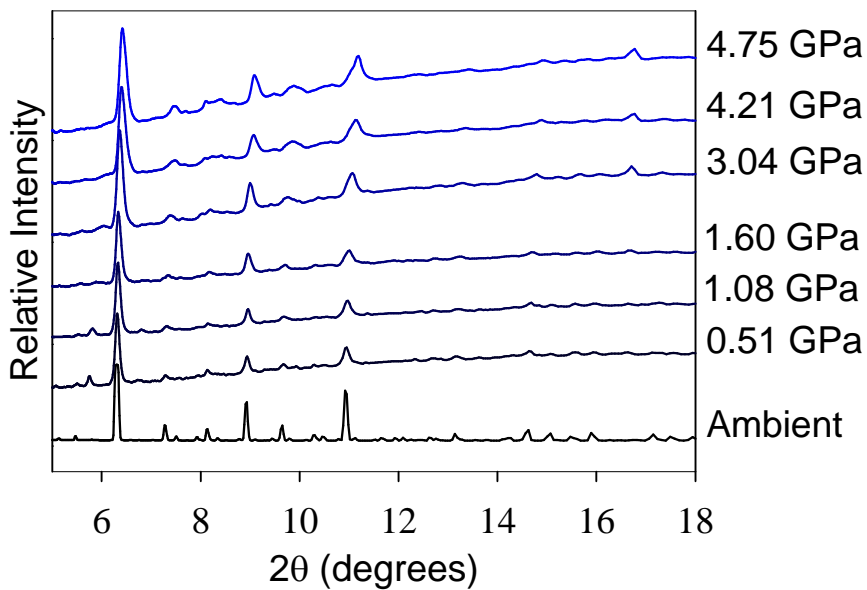
1065 3.2 C_4A_3 Bulk Modulus Determination

1066 Figure 8 shows the 2D diffraction pattern of C_4A_3 in ambient conditions. After integrating
 1067 radially, the plot of intensity vs. 2θ is obtained, Figure 9. Figure 9 shows the diffraction patterns
 1068 as a function of pressure, and the d-spacings of C_4A_3 decrease (peaks shifting to larger 2θ) with
 1069 increasing pressure as expected.

1070



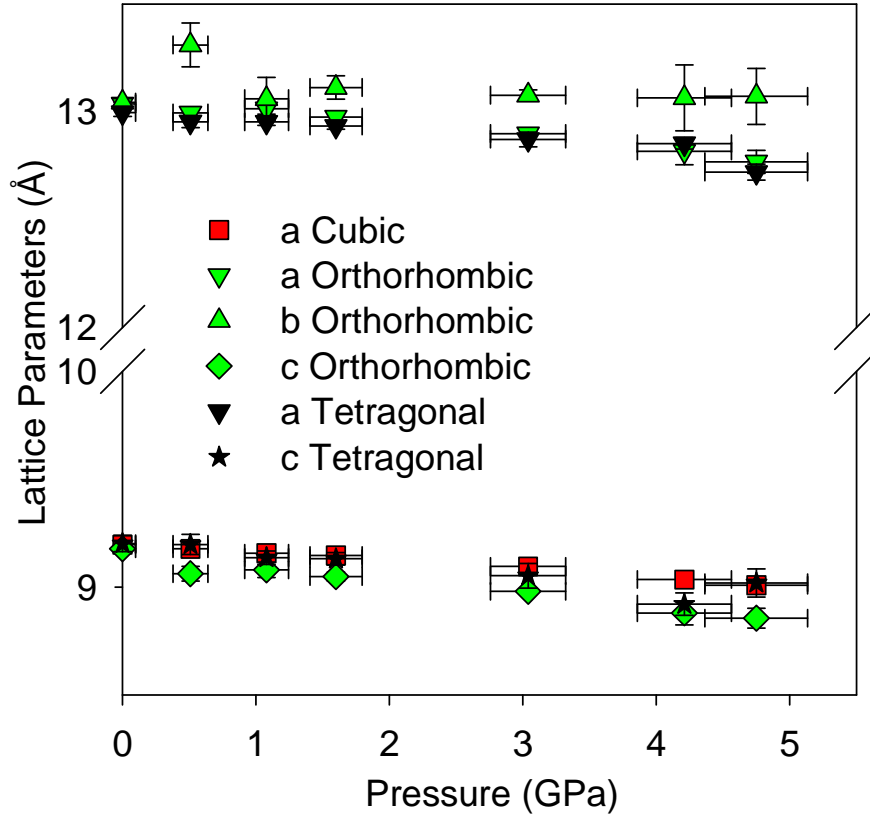
1071
1072 Figure 8: Ambient C_4A_3 X-ray powder diffraction pattern.



1073
1074 Figure 9: Integrated X-ray powder diffraction pattern for C_4A_3 from ambient pressure to 4.75
1075 GPa.

1076 Figure 10 shows how the lattice parameters change with pressure. The cubic lattice parameter, a ,
1077 appears to have a more uniform contraction than the orthorhombic cell parameters; however, the

1078 variability in the orthorhombic cell parameters is most likely a result in the difficulty of fitting
 1079 the lattice parameters to a crystal structure that has so many overlapping reflections; however the
 1080 variability in the orthorhombic lattice parameters averages out and all crystal structures volumes
 1081 show a contraction of approximately 5.5(2)% from 0.51 to 4.75 GPa.



1082
 1083 Figure 10: Change in lattice parameters as a function of pressure.

1084 Figure 11 illustrates the pressure dependent behavior of the unit-cell's volume. Additionally, the
 1085 Birch-Murnaghan equation of state (B.M. EOS) [131] assuming $K'_0=4$ is plotted, Eqn. 13.
 1086 Additionally, the Eulerian strain (Eqn. 14) and normalized pressure (Eqn. 15) can be defined and
 1087 used to reorganize the B.M. EOS into the simpler linear form (Eqn. 16).
 1088

1089
$$3^{\text{rd}} \text{ Order B.M. EOS: } P=1.5K_0 \left[(V_0/V)^{7/3} - (V_0/V)^{5/3} \right] \left[1+0.75(K'_0-4) \left\{ (V_0/V)^{2/3} - 1 \right\} \right] \quad (13)$$

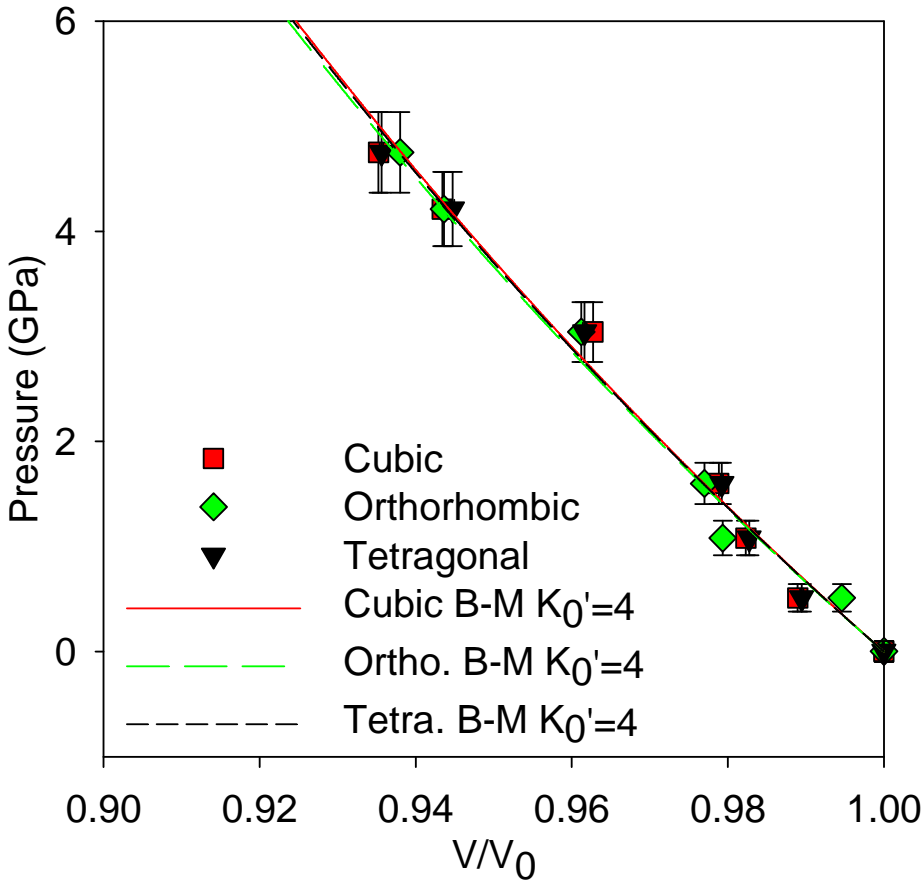
1090 Eulerian Strain:
$$f=0.5 \left[(V_0/V)^{2/3} - 1 \right] \quad (14)$$

1091 Normalized Pressure:
$$F=P/[1.5 \{ (V_0/V)^{7/3} - (V_0/V)^{5/3} \}] \quad (15)$$

1092 Linear form of B.M. EOS:
$$F(f)=K_0-1.5K_0(4-K'_0)f \quad (16)$$

1093
 1094 Due to different conditions in ambient XRD versus in high pressure XRD with the diamond anvil
 1095 cell, a g-G plot was used to find C_4A_3S 's initial state cell volume in the diamond anvil cell [132].
 1096 Second order B.M. EOS ($K'_0=4$) were fitted with $R^2 = 0.986, 0.990, 0.990$ for the cubic,
 1097 orthorhombic, and tetragonal cases, respectively. There was no sign of rearrangement or

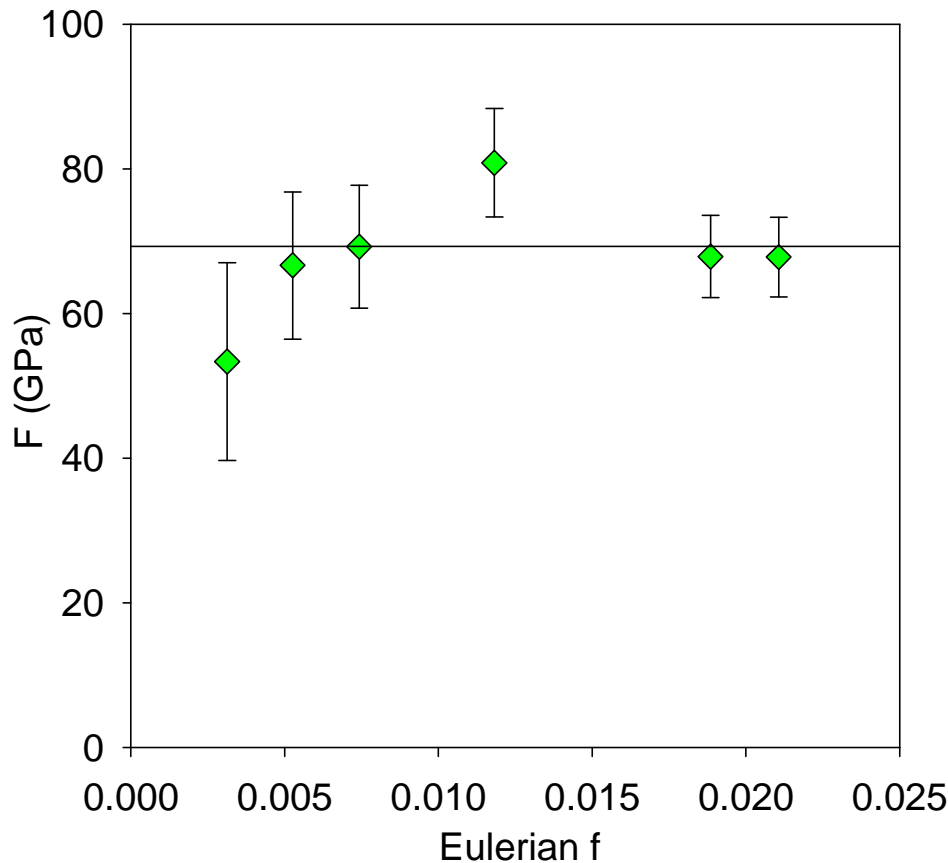
1098 abnormal compressibility in the diffraction patterns or in the pressure dependent response of the
 1099 volume. The largest propagated error from the refined lattice parameters to the cell volume was
 1100 0.01 \AA^3 .



1101
 1102 Figure 11: Pressure dependent unit-cell volume change normalized to the ambient volume.

1103 Figure 12 shows the normalized pressure, F , as a function of the Eulerian Strain, f , see Eqns. 14-
 1104 15. From the plot, it is clear that the bulk modulus (where the B.M. EOS intercepts the y-axis) is
 1105 $69(6) \text{ GPa}$. The propagated error mostly arises from the utilization of the ruby fluorescence
 1106 technique to determine the pressure offline. Due to the remaining uncertainty about the crystal
 1107 structure of C_4A_3 , the analysis was also performed utilizing the cubic subcell. The difference in
 1108 the bulk modulus calculated using the orthorhombic structure or the cubic subcell was less than 1
 1109 GPa. The bulk modulus is relatively low due to the open and tilted sodalite framework when
 1110 compared to other minerals that have denser packing such as $239(4) \text{ GPa}$ for corundum (α -
 1111 Al_2O_3) [133]. For a clinker mineral, the atomistic framework and the type of uptaken ion are
 1112 important in its compressibility and reactivity [134]. For example, in a unit cell of C_3A , there are
 1113 72 cavities consisting of Al_6-O_8 rings filled with a Ca atom and eight empty cavities. Even
 1114 though C_3A is quite incompressible $\{102(6) \text{ GPa}\}$, the 8 empty cavities make the whole system
 1115 quite reactive with water [134]. Likewise, C_4A_3 's large crystal structure porosity and relatively
 1116 higher internal energy and activity make it relatively unstable and reactive with water [44].
 1117 C_4A_3 's bulk modulus is higher than reported bulk moduli for hydrated cementitious phases,
 1118 $27(7)$, $37.8(1)$, $32(2)$, and $54(4) \text{ GPa}$ for ettringite, CH, hemicarboaluminate, and

1119 monocarboaluminate, respectively [135-138].



1120
1121 Figure 12: Normalized pressure, F, as a function of Eulerian strain, f, for orthorhombic crystal
1122 structure.

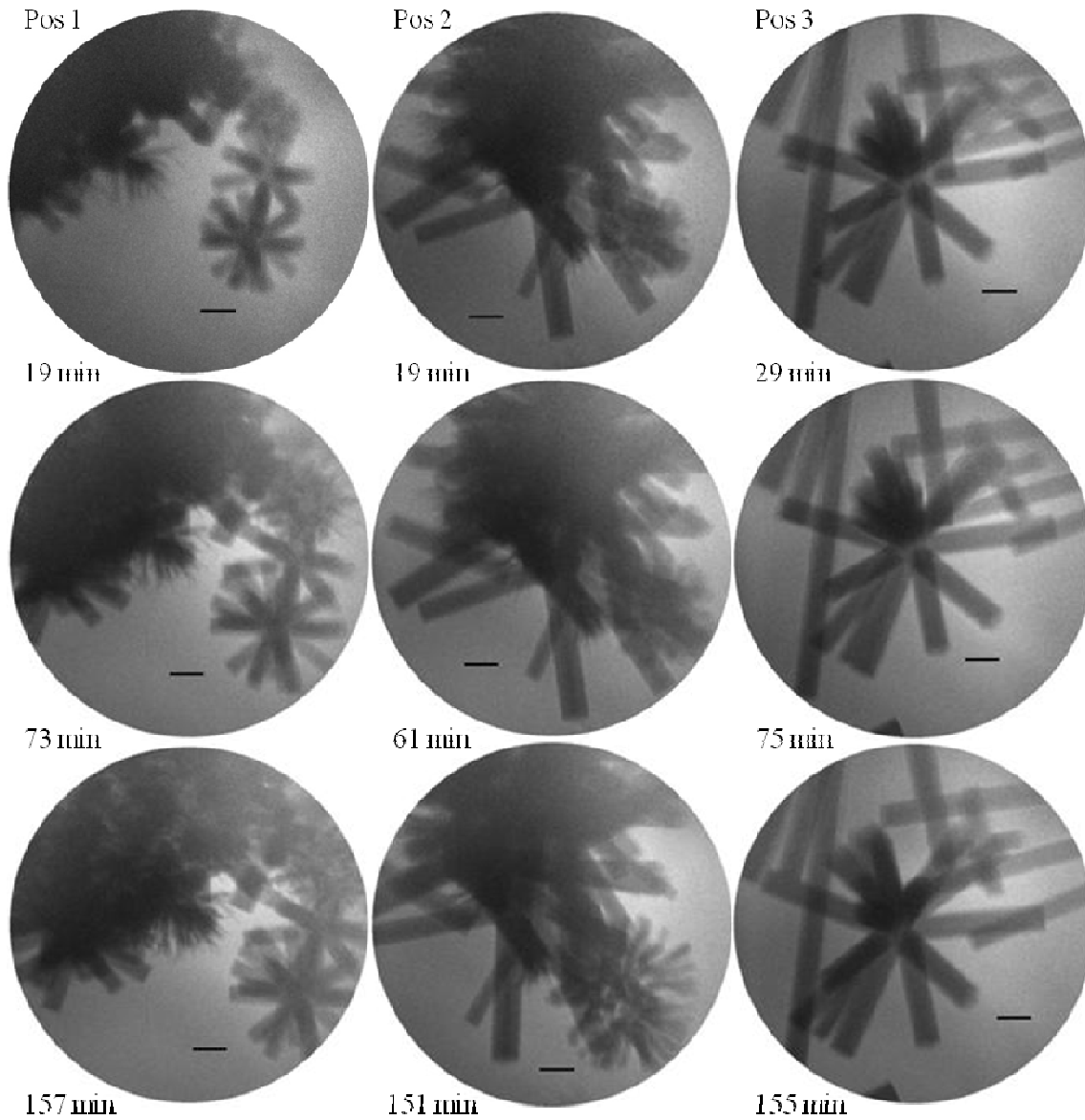
1123 C_4A_3 's bulk modulus is higher than some other sodalites' bulk moduli of 52(8) GPa for
1124 $Na_8(AlSiO_4)_6Cl_2$ [139] or 43(4) GPa for $Na_8(AlSiO_4)_6(OH)_2 \cdot H_2O$ [140], which have monovalent
1125 caged ions and silicon in the framework. The higher bulk modulus of C_4A_3 compared to the
1126 other sodalites listed can be in part explained by the higher charged anion and cation of C_4A_3
1127 compared to the other structures. As explained by Melzer et al. [141], with increasing charge of
1128 the anions and cations, the variation of lattice energy increases which decreases the
1129 compressibility of the lattice. By comparing the bulk modulus of C_4A_3 with
1130 $Sr_8(Al_{12}O_{24})(CrO_4)_2$ (72 GPa calculated from [141]), which has the same aluminate cage and
1131 divalent cage ions, the effect that the caged ions' sizes have on the lattice compressibility can be
1132 observed. Ca^{2+} and Sr^{2+} have effective ionic radii of 1.12 Å and 1.26 Å, respectively, for
1133 coordination numbers of 8, and sulfate and chromate ions have bond distances of 1.50 Å and
1134 1.65 Å, respectively [142-144]. As the size of the caged ions increases, the compressibility of
1135 the lattice decreases, this makes sense structurally.

1136 **CHAPTER 4: C_4A_3 HYDRATION IN THE PRESENCE OF GYPSUM**
1137 **AND CALCIUM HYDROXIDE**

1138 **4.1 Dilute Suspension Experiments**

1139 **4.1.1 Soft X-ray Microscopy**

1140 Figure 13 shows in-situ soft X-ray images of hydrating C_4A_3 particles suspended in S1. Each of
1141 the three columns in each figure corresponds to a single position in the cell viewed for almost
1142 three hours. The elapsed time after mixing is indicated below each image, so that the evolution
1143 of each sample position can be followed by scanning down the columns. The scale bar in each
1144 image corresponds to 1 μm .



1145
1146 Figure 13: In-situ soft X-ray images of hydrating C_4A_3 particles in a saturated $\text{CH-C}_2\text{H}_2$
1147 solution, liquid/solid = 50 ml/g. Hydration time is indicated. Scale bar corresponds to 1 μm .

1148 Figure 13 shows that the majority of ettringite formed in this system occurred before the first
1149 images were taken (taken 19-29 minutes after mixing); however, certain sites do show evolution
1150 with time. This suggests that the hydration of small ($< 5 \mu\text{m}$) $\text{C}_4\text{A}_3\text{S}$ particles is very rapid and
1151 was almost complete by the time the first image was recorded in the suspension without excess
1152 CH. However, some evolution with time occurs. The upper right hand corner of Position 1 and
1153 lower right hand corner of Position 2 show evidence of an amorphous hydrate evolving into a
1154 stellate (star-shaped) ettringite cluster. Most of the images in Figure 13 are dominated by large
1155 acicular crystals, typically of the order of $0.5\mu\text{m}$ in width and ranging from about $2\mu\text{m}$ to over
1156 $10\mu\text{m}$ in length. Based on what is already known about $\text{C}_4\text{A}_3\text{S}$ hydration and the morphology of
1157 the usual reaction products, there can be little doubt that this acicular phase is ettringite;
1158 however, this will be confirmed later in the discussion. What is somewhat more unusual,
1159 however, is the crystal habit of the ettringite clusters that are observed. Most of them are stellate
1160 polycrystalline clusters that give the appearance of having grown out from a single central point.
1161 Accordingly, the clusters on the bottom right hand side of the column representing Position 1 do
1162 show growth from the first image to the final image which confirms that the acicular crystals are
1163 lengthening by growing outwards from the center of the “star”. It thus appears likely that this
1164 stellate growth pattern represents growth from a single central nucleus.
1165

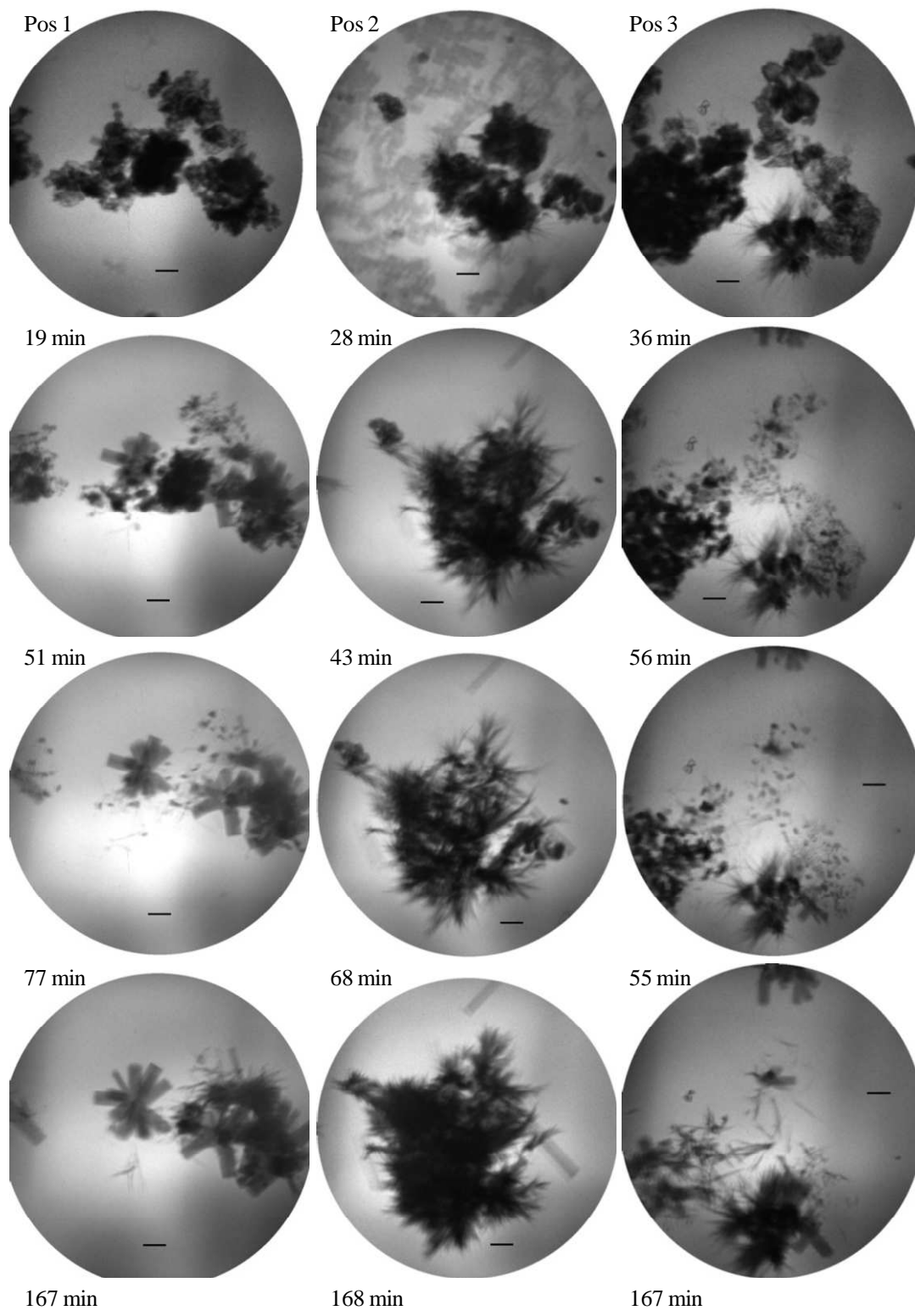
1166 The question then arises about why such a growth form should occur. It is not easy to tell by
1167 looking at two-dimensional images such as these, but it seems possible that there may be defined
1168 angular relationships between the “arms” of each cluster, which brings to mind the possibility
1169 that twinning might be involved in the early growth phases. The possibility of twinning and
1170 defined angles between ettringite crystals is discussed more in the SEM investigation. As to why
1171 a stellate growth pattern should be favored at early ages in this system, this is probably related to
1172 details of the nucleation process. We hypothesize that a layer of amorphous hydrates initially
1173 forms around $\text{C}_4\text{A}_3\text{S}$ due to its very rapid initial hydration. Due to surface energy considerations,
1174 the amorphous hydrate shells probably maintain a relatively spherical shape around small grains
1175 of $\text{C}_4\text{A}_3\text{S}$. After a period of nucleation, well-defined ettringite crystals begin to form on the
1176 surface of the amorphous hydrate and then grow out radially forming stellate structures.
1177 Previous research has also shown the development of stellate ettringite (often referred to as
1178 spherulites, although this term implies that the radiating crystals are surrounded by a matrix). In
1179 2009, Komatsu et al. [145], showed the in-situ formation of ettringite from the reaction of CH
1180 with aluminum sulfate. They also observed stellate structures and found that the presence of
1181 small calcite crystals increased the amount and rate of stellate ettringite formation. Likewise,
1182 they confirmed in a SEM that calcite was at the core of the stellate cluster. Mehta [146] in 1976
1183 also showed ettringite growing in a stellate manner from the surface of C_3A immersed in a $\text{C}\text{S}\text{H}_2$
1184 solution. Likewise, Lerch et al. in 1929 [147] presented a spherulite of ettringite that had grown
1185 in a mortar briquette, and Candlot [148] produced spherulites of 2 to 3 mm in diameter from
1186 mixed calcium aluminate and calcium sulfate solutions in 1890.
1187

1188 The images obtained from S2 with excess CH (Figure 14) are significantly different. At early
1189 ages (before about 40 minutes) we see almost no sign of the well-developed acicular crystals as
1190 seen in Figure 13. Well-developed ettringite crystals, which include some stellate clusters
1191 similar to but generally smaller than those seen in Figure 13, only become visible in the later
1192 images. We do see more of relatively dense clusters of very fine hair-like growths radiating from
1193 denser core particles which may well still contain anhydrous $\text{C}_4\text{A}_3\text{S}$. These growths are very

1194 reminiscent of the “sheaf-of-wheat” growth patterns seen around C_3S particles and PC grains in
1195 previous X-ray microscopy studies [149]. At the very early ages, we see what may well be the
1196 outlines of the original unreacted phases (C_4A_3 and also possibly solid CH) covered with a thin
1197 coating of what appears to be mainly an amorphous “gel” from which the hair-like crystals have
1198 already begun to grow at certain points such as the bottom center of Position 3. In the later
1199 images it is less easy to see any remnants of the original particles and a mixture of well-
1200 developed ettringite crystals similar to those of Figure 13 plus dense particles covered with a
1201 thick growth of fine hair-like products remain.

1202
1203 These observations suggest that the presence of excess CH initially retards the rate of ettringite
1204 formation, perhaps by stabilizing a gelatinous hydrate coating of poorly-crystalline phases on the
1205 hydrating grain’s surface and, also, changes the morphology of some of the hydration products
1206 formed. This is consistent with the work of Mehta, who suggested that lime somewhat retards the
1207 formation of ettringite from C_4A_3 at early ages and causes smaller ettringite crystals to form
1208 [150]. Moreover, while studying hydration kinetics, Hanic et al. [151] found that hydration rates
1209 in some C_4A_3 systems with C_2H_2 and CH became diffusion limited, which implied that a
1210 hydration layer surrounded the reacting C_4A_3 grains.

1211
1212 To help determine how Figure 13 and Figure 14’s high liquid/solids ratio was affecting the
1213 hydration products, a 5x lower liquid/solids of 10 was tested for S1, which lacked excess solid
1214 CH. A liquid/solids ratio of 10 approaches the limit of the wet cell experimental setup utilized.
1215 As was the case with the higher liquid/solids ratio, ettringite grew very rapidly and little growth
1216 occurred subsequently. Likewise, stellate and acicular ettringite crystal habits were observed.

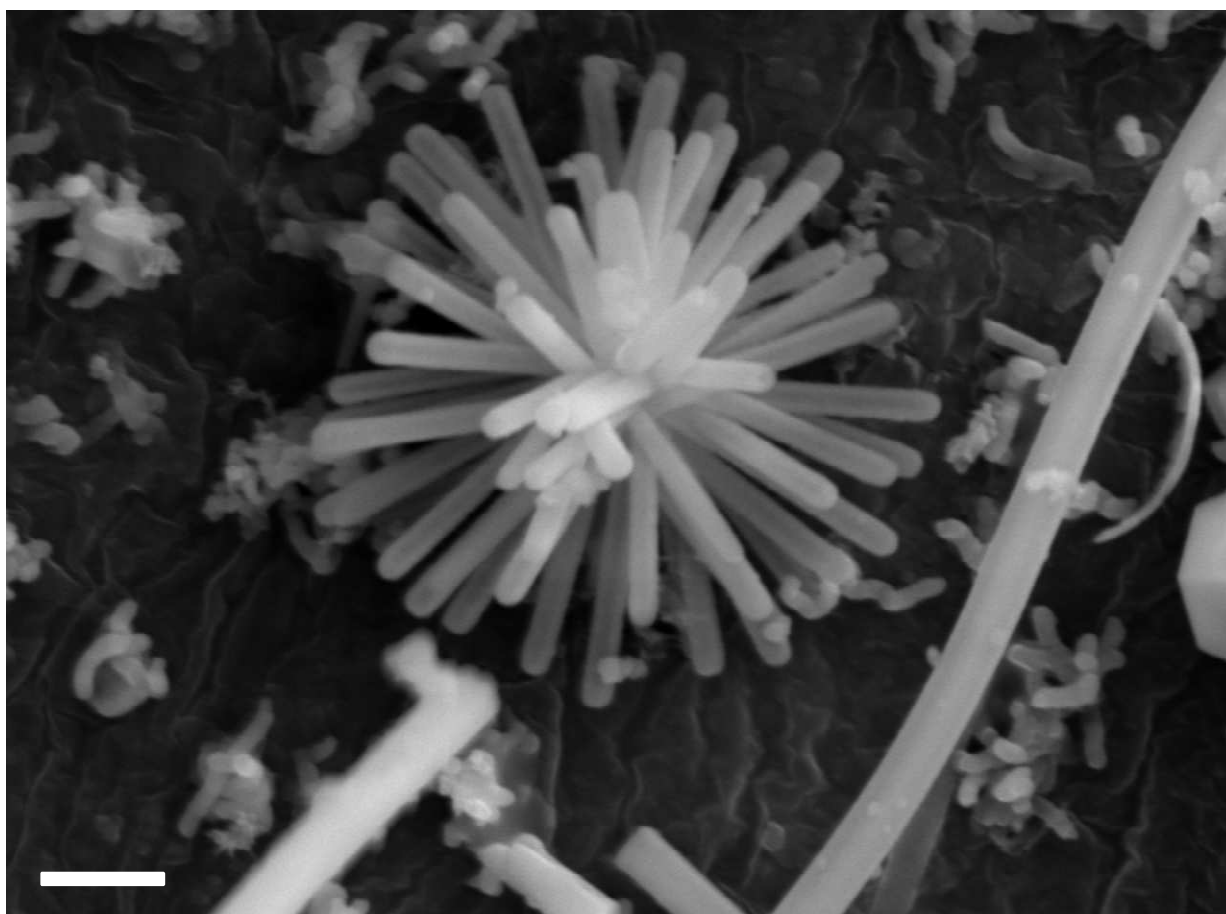


1217
1218
1219
1220

Figure 14: In-situ soft X-ray images of hydrating C_4A_3 particles plus 10% solid CH in a saturated CH- C_2H_2 solution, liquid/solid = 50 ml/g. Hydration time is indicated. Scale bar is 1 μm .

1221 **4.1.2 Scanning Electron Microscopy**

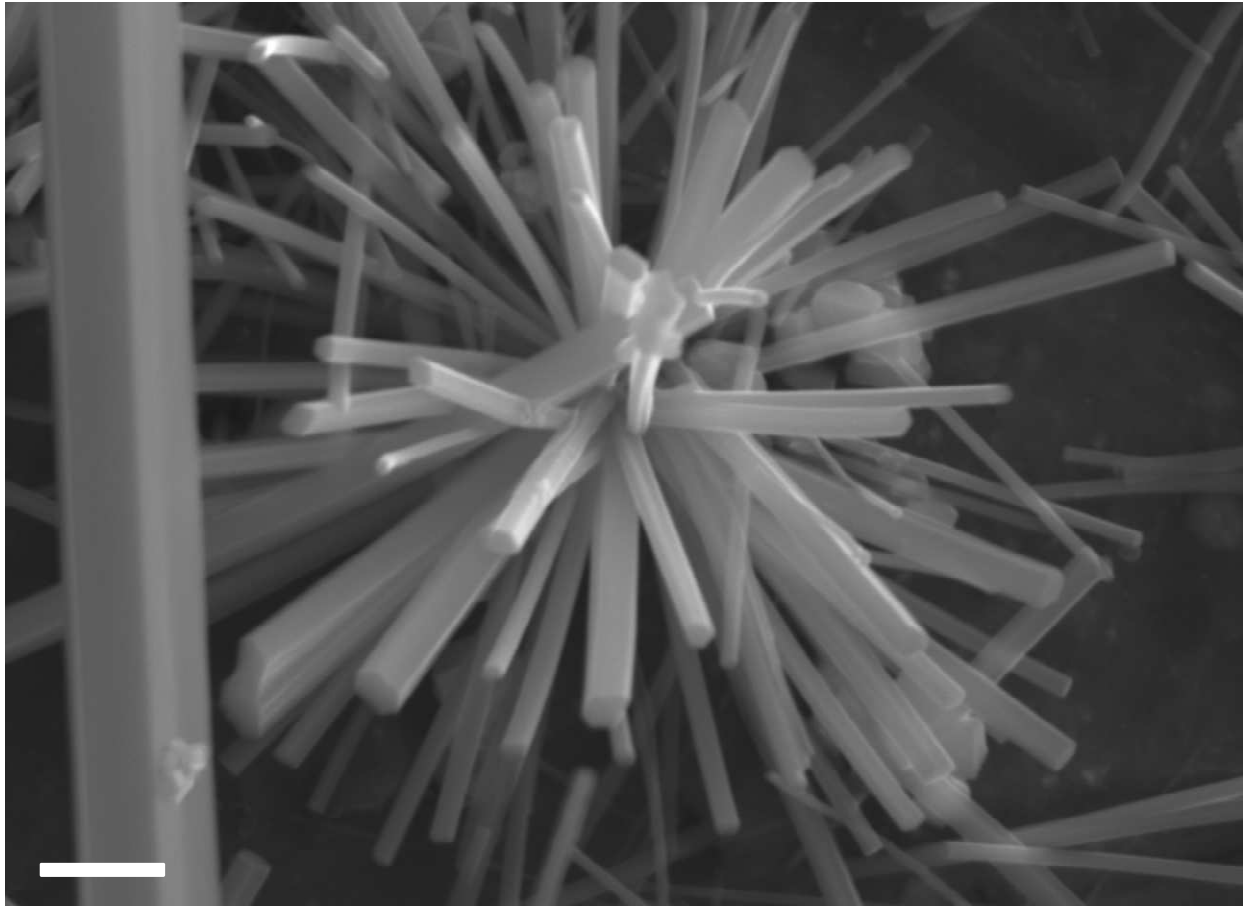
1222 To confirm the observations made with the soft X-ray microscope and provide additional
1223 compositional information, ex-situ dried dilute suspensions were investigated using a SEM.
1224 Stellate ettringite crystals were observed in samples made from suspensions with and without
1225 excess CH, see Figure 15 & Figure 16. In addition to the stellate ettringite cluster in Figure 15,
1226 worm-like hydrates can be seen in the background; these worm-like structures are most likely
1227 poisoned ettringite crystals from organic compounds in the carbon tape placed on the mounting
1228 stubs before the dilute suspensions were placed on the mounting stubs. Only Figure 15 contains
1229 images from samples that were hydrated on stubs covered in carbon tape, and it is presented here
1230 to show the type of artifacts that can be introduced by hydrating samples on carbon tape. The
1231 rest of the SEM images contain samples that were hydrated directly on the mounting stubs
1232 without carbon tape to avoid any contamination.
1233



1234 Figure 15: Ex-situ secondary electron (SE) SEM images of hydrating C_4A_3 particles in a
1235 saturated CH- C_2H_2 solution, liquid/solid = 50 ml/g. Hydration time was 2 hours. Accelerating
1236 voltage of 15.00 kV, a probe current of 248 pA, working distance of 12.0 mm, and scale bar is 2
1237 μ m.
1238

1239 In Figure 16, another ettringite crystal can be seen penetrating from the lower left to the upper
1240 right of the stellate ettringite cluster, illustrating the beginning of ettringite crystals that began in
1241

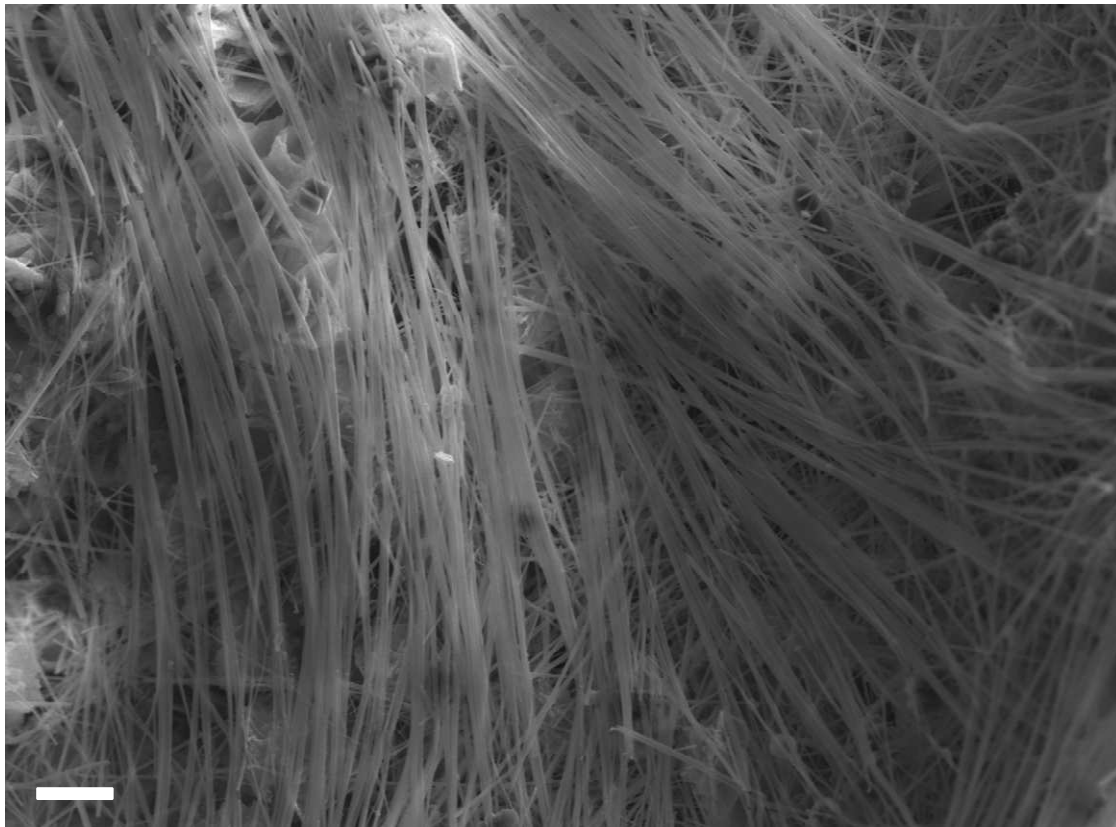
1242 separate regions and intergrew. Figure 17 presents an EDS spectrum from a stellate ettringite
1243 cluster. Several clusters were analyzed with EDS and were found to have similar compositions
1244 regardless of whether or not the suspension contained excess CH. The specimens were not flat,
1245 so the EDS results cannot provide accurate quantitative data, but they can be used to eliminate
1246 the possibility that the observed phases were other calcium aluminum hydrates with similar
1247 morphologies. The calculated Ca/S atomic ratio from Figure 17 was 2.2, which is close enough
1248 to the theoretical value of 2 for ettringite, considering the non-ideal EDS conditions.
1249



1250
1251 Figure 16: Ex-situ SE SEM images of hydrating C_4A_3 particles plus 10% solid CH in a
1252 saturated CH- C_2H_2 solution, liquid/solid = 50 ml/g. Hydration time was 2 hours. Accelerating
1253 voltage of 15.00 kV, a probe current of 248 pA, working distance of 14.0 mm, and scale bar is 2
1254 μm .

1255
1256
1257

Figure 17: EDS Spectrum of stellate ettringite cluster collected with an accelerating voltage of 15.00kV and a probe current of 2.0 nA.



1258
1259
1260

Figure 18: Ex-situ SE SEM images of hydrating C_4A_3 particles plus 10% solid CH in a saturated CH- C_2H_2 solution, liquid/solid = 50 ml/g. Hydration time was 2 hours. Accelerating

1261 voltage of 15.00 kV, a probe current of 248 pA, working distance of 13.5 mm, and scale bar is
1262 10 μm .

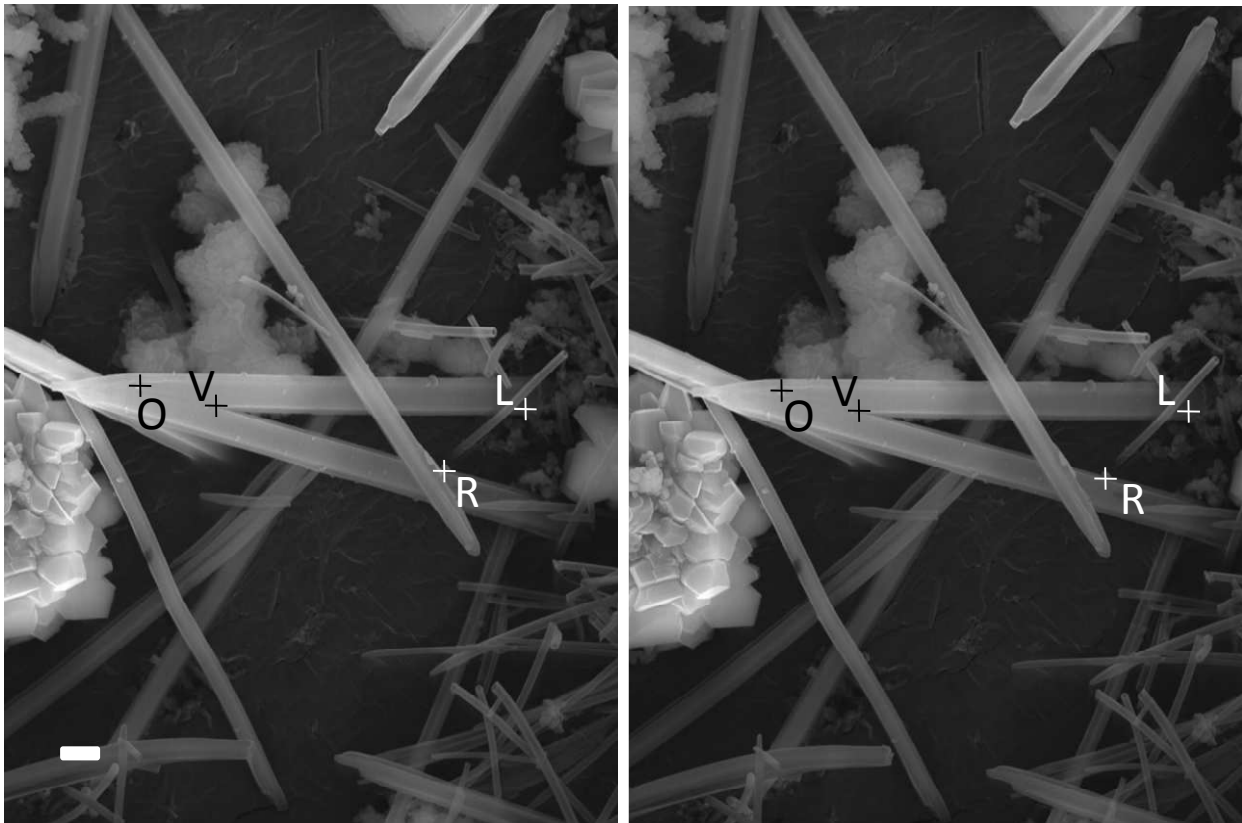
1263 In suspensions made with excess CH, filiform (very long thin, hair-like) ettringite needles were
1264 common, see Figure 18. This crystal habit was absent in the suspensions made without excess
1265 CH. Rosettes of AFm were also much more common in the suspensions made with excess CH
1266 as were fields of reticulated (slender crystals intergrown in a lattice-like array) ettringite, see
1267 Figure 19. Both the suspensions with and without excess CH produced the typical acicular
1268 ettringite crystals.
1269



1270
1271 Figure 19: Ex-situ SE SEM images of hydrating C_4A_3 particles plus 10% solid CH in a
1272 saturated CH- CH_2 solution, liquid/solid = 50 ml/g. Hydration time was 2 hours. Accelerating
1273 voltage of 15.00 kV, a probe current of 248 pA, working distance of 13.0 mm, and scale bar is
1274 10 μm .

1275 During the SEM and soft X-ray microscopy investigations many ettringite crystals were
1276 observed diverging and forming angles. These diverging crystals appeared to have originated
1277 from the same nucleus. Stellate ettringite clusters as well as small groups of crystals displayed
1278 this morphology. To determine if there was a common angle between all the diverging crystal
1279 groups which would imply that twinning could be the cause of the diverging crystals,
1280 stereoscopic measurements were made in the SEM to determine the true 3D angle between the
1281 crystals from the 2D images. Figure 20 shows a stereo pair of SE SEM images. The image on

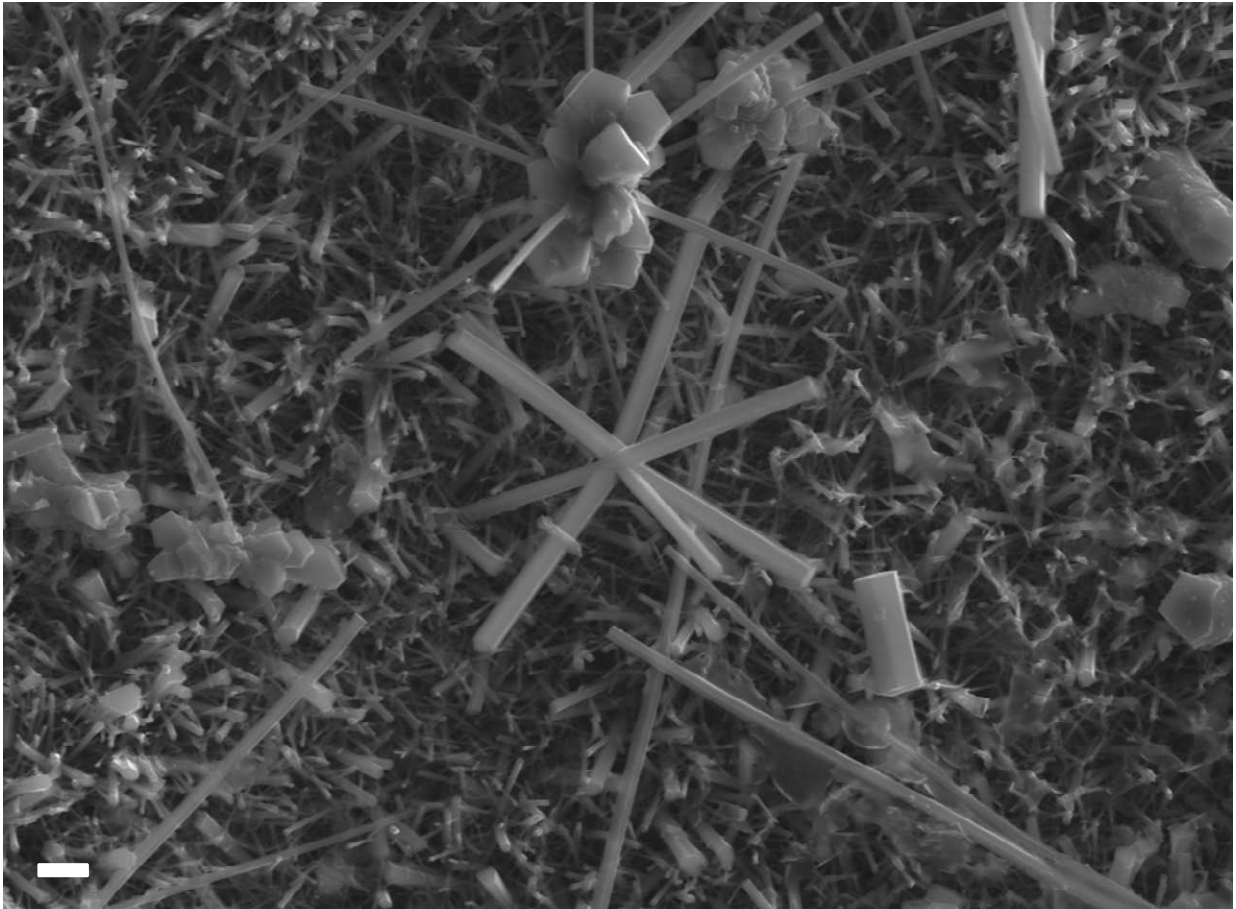
1282 the left is tilted 5° off the electron beam axis in relation to the image on the right, and the same
1283 positions on the crystals are marked in each image. Small surface deposits or imperfections on
1284 the crystals were used for locations so that the exact same positions could be located between the
1285 2 images. The origin is selected as a very recognizable spot in both images and is subtracted
1286 from all the other coordinates measured; this corrects the measurements in case the image has
1287 drifted horizontally or vertically. The positions of the image origin (O), crystal vertex (V), left
1288 (L), and right (R) crystals were determined, and the angle between the crystals was determined
1289 using the law of cosines. A wide distribution of angles (approximately $8^\circ - 37^\circ$) was found
1290 implying that twinning was not the principal mechanism for creating the diverging angles. If
1291 twinning had been the principal mechanism then exactly the same angle(s) would have been
1292 encountered repeatedly due to crystal twinning laws.
1293



1294
1295 Figure 20: Stereo pair of SE SEM images. Image on the left is tilted 5° off the electron beam
1296 axis. Accelerating voltage of 25.00 kV, probe current of 101 pA, working distance of 20.0 mm,
1297 and scale bar is 2 μm .

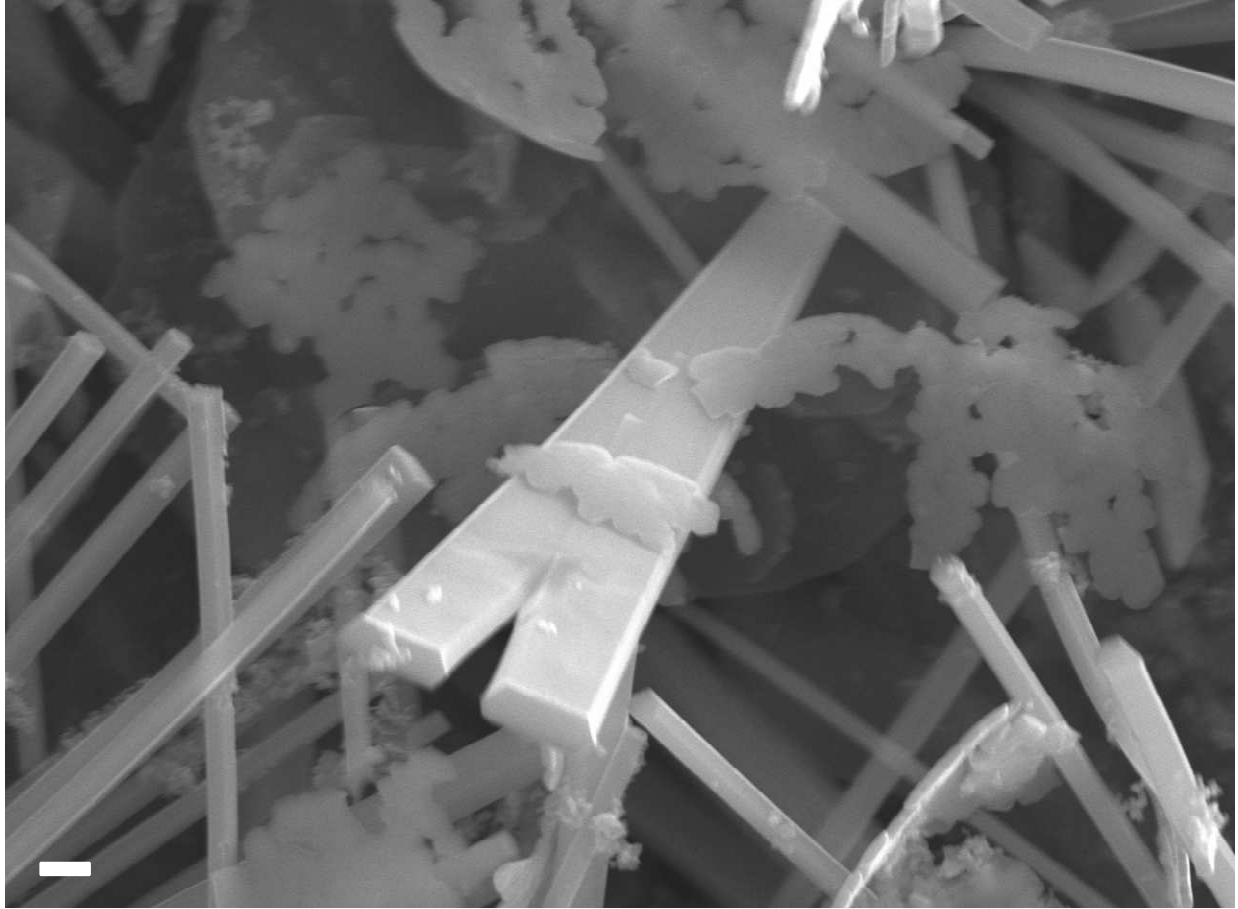
1298
1299 A possible explanation for the distribution of angles encountered for the diverging ettringite
1300 crystals can be formulated based upon differences in the nucleation site's curvature. If the
1301 nucleation site was a perfectly flat plane then one would expect that the crystals growing off its
1302 surface would be parallel for the most part; however, as the nucleating plane becomes curved and
1303 crystals continue to grow normal to its surface then angles begin to form between the crystals.
1304 As the curvature of nucleation site becomes sharper or in other words as the radius of the
1305 nucleating site becomes smaller, the angle between the diverging crystals would become greater.

1306 Figure 21 provides an example of a stellate ettringite cluster with very different angles between
1307 the ettringite crystals compared to those of Figure 15 & Figure 16. We hypothesize that stellate
1308 ettringite clusters exist in pastes that contain C_4A_3S as a result of ettringite nucleating from the
1309 surface of the gelatinous hydrates that form on the surface of C_4A_3S grains. Additionally, the
1310 interpenetration of adjacent stellate ettringite structures could contribute to the strength of the
1311 matrix. Future research is needed to definitively establish the existence/role of stellate structures
1312 in pastes.
1313



1314
1315 Figure 21: Ex-situ SE SEM image of hydrating C_4A_3S particles plus 10% solid CH in a
1316 saturated CH- CSH_2 solution, liquid/solid = 50 ml/g. Hydration time was 2 hours. Accelerating
1317 voltage of 15.00 kV, a probe current of 248 pA, working distance of 13.5 mm, and scale bar is 2
1318 μm .

1319
1320 Although twinning does not appear to be the dominant mechanism for the formation of stellate
1321 ettringite clusters, Figure 22 gives some visual evidence that twinning may also occur. The
1322 crystal appears to have grown wider as it grew away from its nucleation site, and eventually split
1323 into diverging crystals, perhaps due to a crystallographic offset which led to the crystal twinning
1324 [152]. A more detailed study utilizing electron backscattered diffraction (EBSD) or single
1325 crystals would be needed to definitively identify twinning in this system.
1326

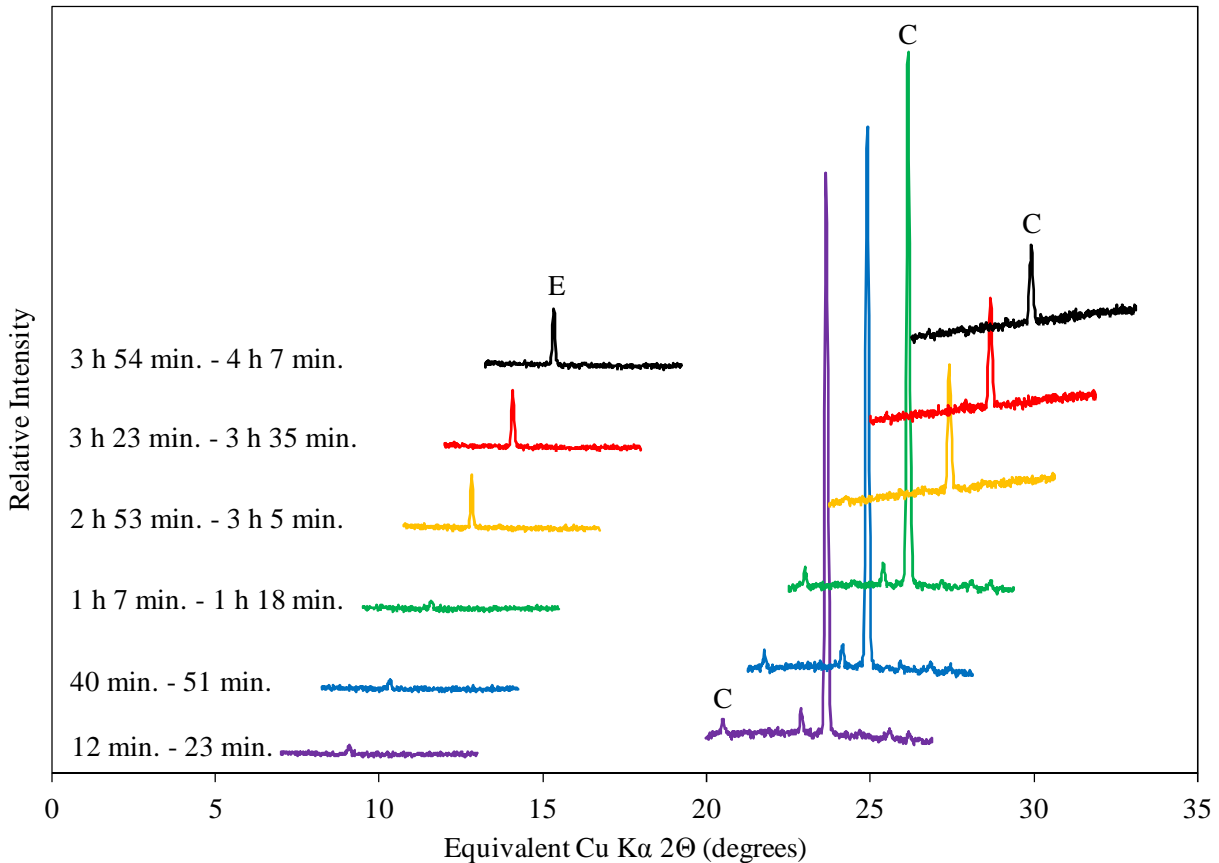


1327
1328 Figure 22: Ex-situ SE SEM image of hydrating C_4A_3 particles in a saturated CH- CSH_2
1329 solution, liquid/solid = 50 ml/g. Hydration time was 2 hours. Accelerating voltage of 15.00 kV,
1330 a probe current of 20 pA, working distance of 14.0 mm, and scale bar is 1 μm .

1331 4.1.3 X-ray Diffraction

1332 To confirm the observations with regard to ettringite formation in S1 (the sample without excess
1333 CH), an in-situ XRD experiment was performed on the supernatant phases of samples
1334 synthesized under the same experimental condition as were used in the soft X-ray microscopy
1335 studies. Figure 23 confirms that C_4A_3 decreases and ettringite increases with time, although the
1336 rate of ettringite formation appears to be slightly different than in the soft X-ray microscopy
1337 study. The difference in rates is probably in part a result of the different w/c and a potentially
1338 different particle size distribution in the supernatant phases since different centrifuges were
1339 utilized.

1340



1341
 1342 Figure 23: In-situ synchrotron X-ray diffraction recording the evolution of ettringite over time
 1343 from the hydration of $C_4A_3\$$ in a saturated CH-calcium sulfate solution, liquid/solid = 10 ml/g
 1344 (E = ettringite, C = $C_4A_3\$$).

1345 4.2 Paste Experiments

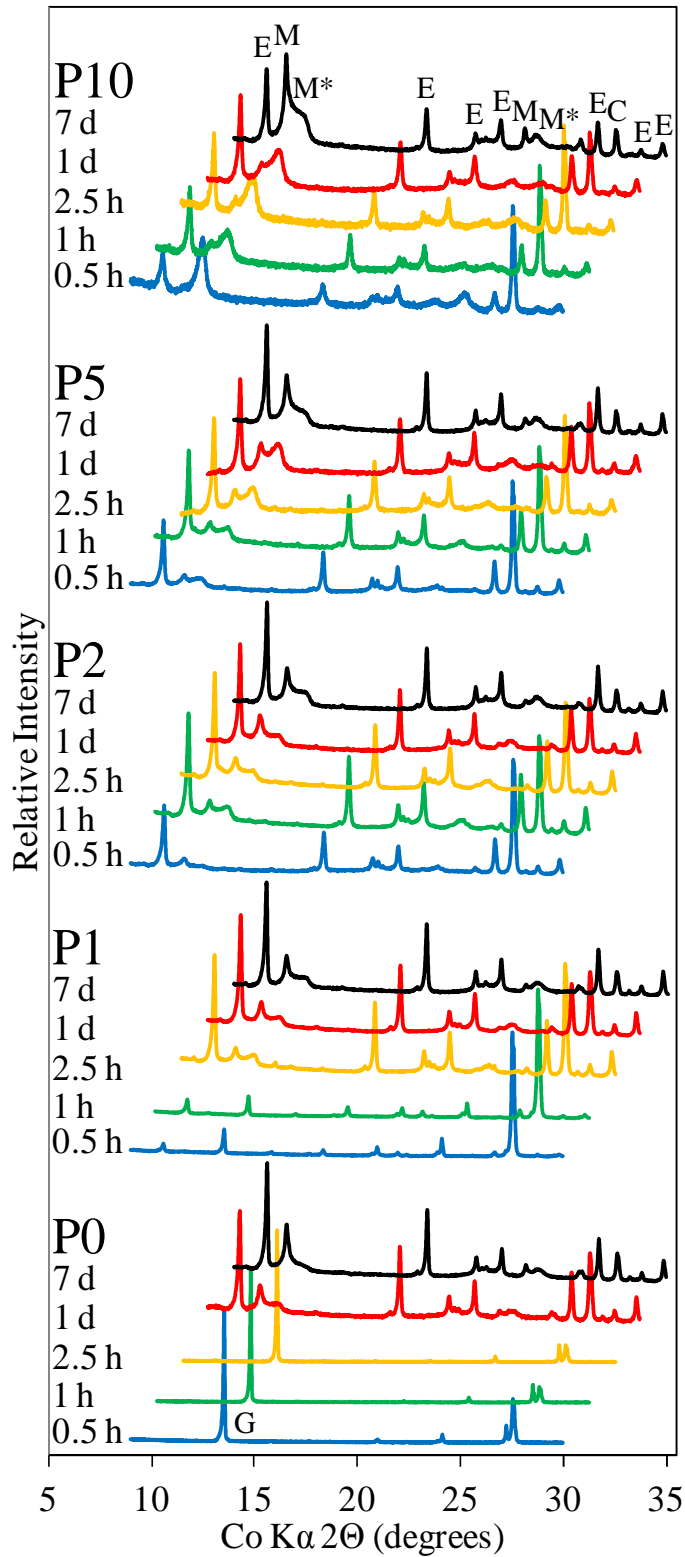
1346 When water was added to mixes with CH, clumps of reaction products formed immediately that
 1347 could be broken up by further mixing to give workable pastes, so this phenomenon could be
 1348 described as a “false set.” However, as the CH amount increased, the time to initial set reduced
 1349 rapidly. During mixing, the samples with higher amounts of CH could be felt to be releasing a
 1350 significant amount of heat very rapidly. This phenomenon could be described as a “flash set.”

1351 4.2.1 X-ray Diffraction

1352 XRD was performed to better understand which phases were forming over time when $C_4A_3\$$ was
 1353 hydrated in the presence of $C\$H_2$ and varying amounts of CH (Figure 24). The 0.5, 1, and 2.5 h
 1354 times were selected to correspond with the soft X-ray microscopy experiments, and the 1 and 7 d
 1355 times were chosen to show how the phases in the pastes evolve during the first week of curing.
 1356 CH was not observed in any of the samples. Increasing CH accelerated the rate of $C\$H_2$
 1357 depletion. This is easily seen comparing P0, P1, and P2. All pastes containing CH form
 1358 ettringite very rapidly. At 0.5 h, 2-5% CH seems to maximize the amount of ettringite formed.
 1359 At 0.5 h as the CH continues to increase from 5 to 10%, the dominant phase formed switches

1360 from ettringite to a solid solution (S.S.) AFm phase containing OH^- and SO_4^{2-} [153]. Moreover,
1361 P10 shows a significant increase in ettringite from 0.5 to 2.5h. This is consistent with the soft X-
1362 ray microscopy investigation which showed that in S2, the suspension with 10% excess CH, the
1363 formation of ettringite was somewhat delayed compared to S1, the suspension that only had CH
1364 from the saturated solution. From the composition of the dissolving $\text{C}_4\text{A}_3\text{S}$, the ions in the
1365 solution, and the XRD results, it is probable that the diffusion barrier observed in Figure 14 is a
1366 calcium hydroxyl-sulfoaluminate hydrate.

1367
1368 In the samples with CH after 1 d, there does not appear to be major changes in the amount of
1369 ettringite or solid solution AFm; however, there is a significant increase in the amount of
1370 monosulfate formed. This is because the CH needed to form the S.S. AFm and the C_2S needed to
1371 form ettringite was entirely consumed by 1 d of hydration. It is interesting to note that even P0
1372 contains humps where the S.S. AFm peaks appear. Potential explanations for this hump include:
1373 carbonation forming a S.S. AFm with CO_3^{2-} and SO_4^{2-} (this could only occur during preparing
1374 the sample for XRD, since the paste was mixed in a nitrogen glove box) or a poorly ordered
1375 monosulfate phase with a range of reduced interlayer spacings. Our experimental set up was
1376 unable to satisfactorily answer this question. Winnefeld and Barlag also had this hump in their
1377 XRD patterns at 1 and 7 d in their CSA sample with ~20% C_2S and 0% CH, but it appears to be
1378 gone by 28 d [63]. The hydration phases produced in our experiments are also fairly consistent
1379 with Klein and Mehta [154]; however, our $A/S = 1.8$ is slightly higher than the systems that they
1380 studied and for our range of $C/S = 2.8-3.4$ instead of ettringite, $\text{C}_x\text{A}_y\text{H}_z$, and monosulfate we
1381 observed S.S. AFm, monosulfate, and ettringite.



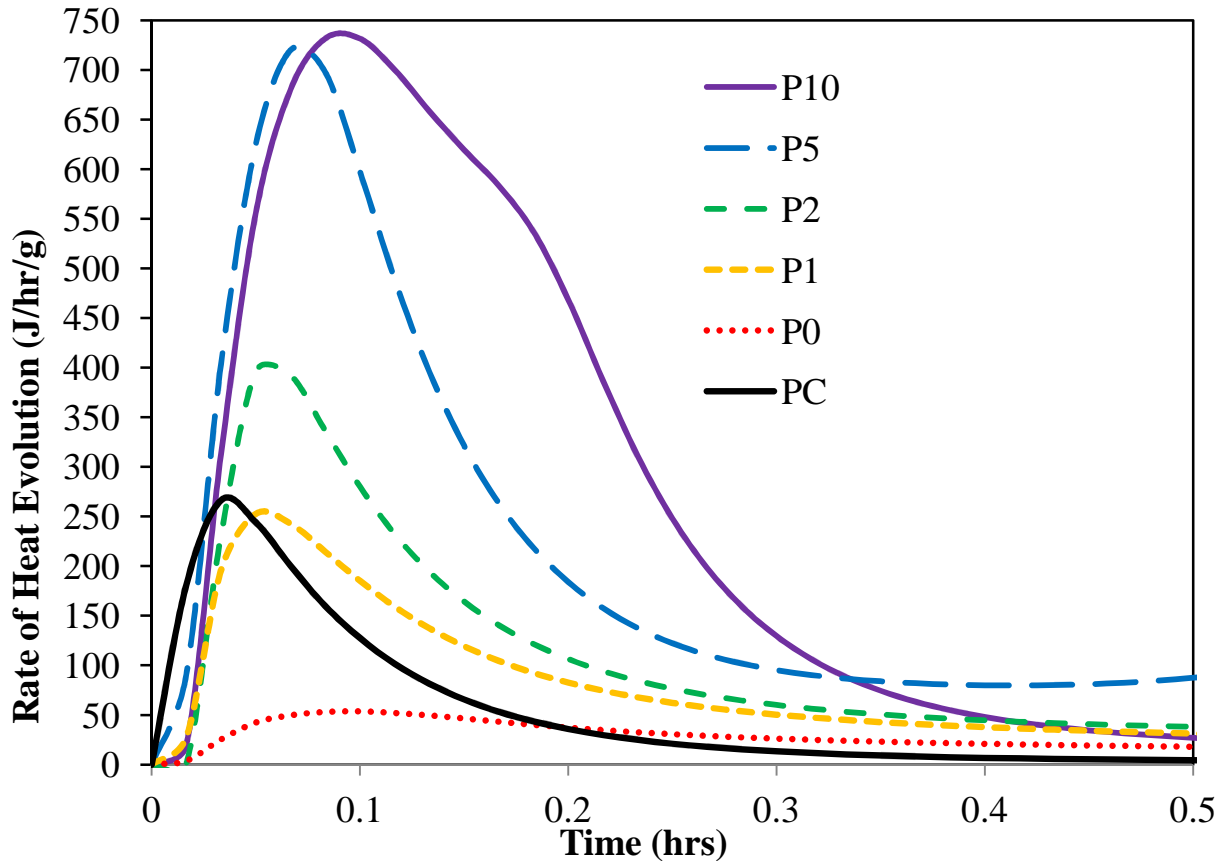
1382
1383
1384

Figure 24: X-ray diffraction patterns for hydrated pastes P0 - P10 from 0.5 h to 7 d (E = ettringite, M = monosulfate, M* = S.S. AFm, C = C_4A_3 , G = C_2H_2).

1385

1386 **4.2.2 Isothermal Conduction Calorimetry**

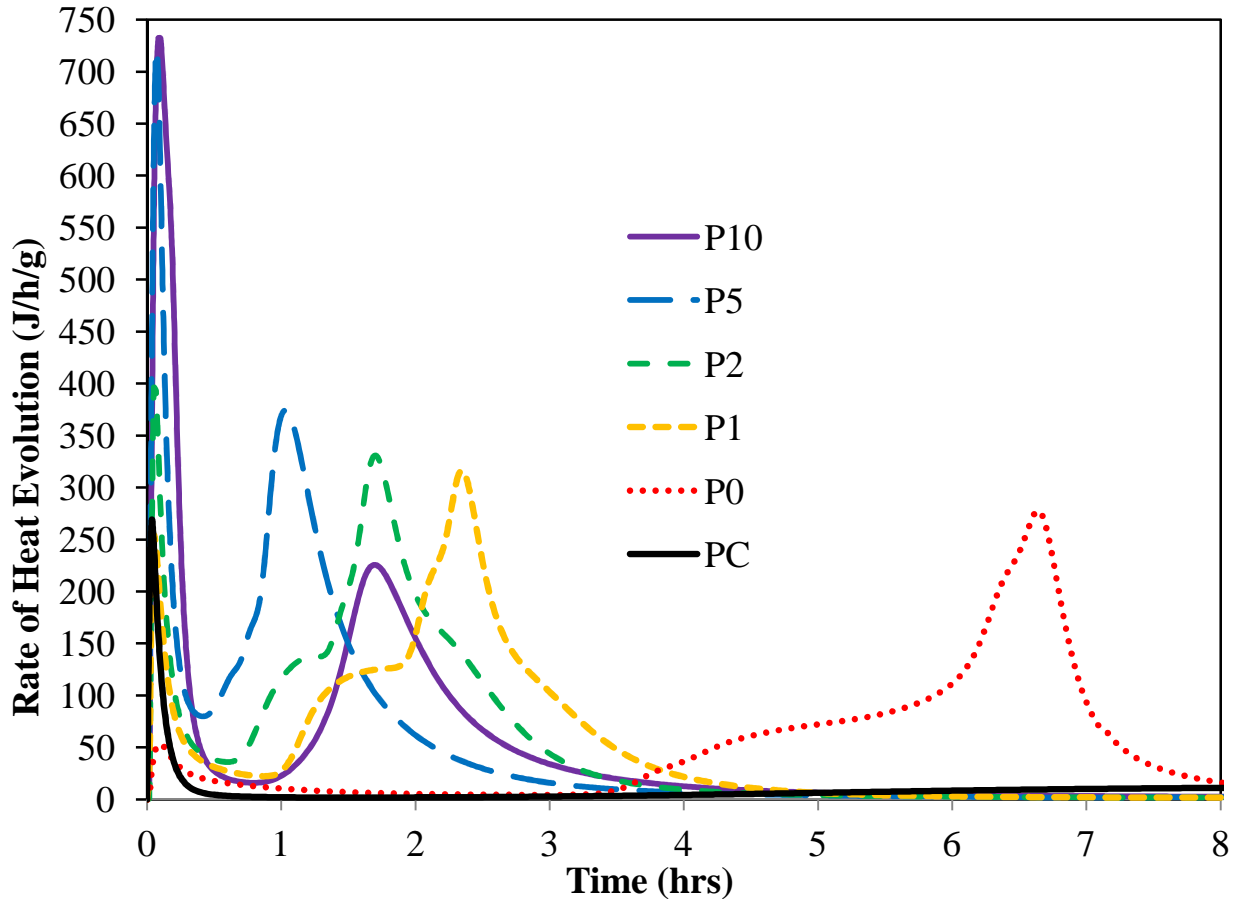
1387 Isothermal conduction calorimetry confirmed the empirical observations about heat evolution
1388 made during the casting of prior samples. Figure 25 shows how the initial rate and duration of
1389 heat evolution increases with increasing CH. This is consistent with the XRD results which
1390 showed that increasing CH increased the quantity of S.S. AFm produced and that all samples
1391 with CH produced ettringite at very early ages. The initial heat evolution peak can therefore be
1392 attributed to heat of wetting and S.S. AFm and ettringite formation.
1393



1394 Figure 25: Influence of increasing CH on the initial rate of heat flow due to C_4A_3S hydration
1395 with 15% C_2SH_2 .
1396

1397 Figure 26 shows how increasing CH generally reduces the time to the 2nd peak in the rate of heat
1398 evolution; with one exception, P10's 2nd peak occurs after P5's. This is probably due to the
1399 rapid formation of large amounts of S.S. AFm in P10 creating a diffusion barrier slowing
1400 hydration (analogous to blocking ettringite or outer C-S-H). This is consistent with the soft X-
1401 ray microscopy analysis which showed what appeared to be a gelatinous hydrate on the surface
1402 of a C_4A_3S grain in the sample with 10% solid CH (Fig. 3). The XRD results would suggest that
1403 P10 and P5's second peak are mostly attributable to the formation of additional ettringite and
1404 various AFm types. Likewise, the XRD results would suggest that the leading shoulder of P0,
1405 P1, and P2's 2nd peak is mostly attributable to ettringite formation, and the following peak is a
1406 C_2SH_2 depletion peak where the formation of monosulfate takes over. Winnefeld et al., also,
1407

1408 showed a reduction in the dormant period between the samples with CH compared to those
 1409 without [63]. Likewise, Palou and Majling [155] showed an increase in the initial rate of heat
 1410 evolution with increasing CH.
 1411



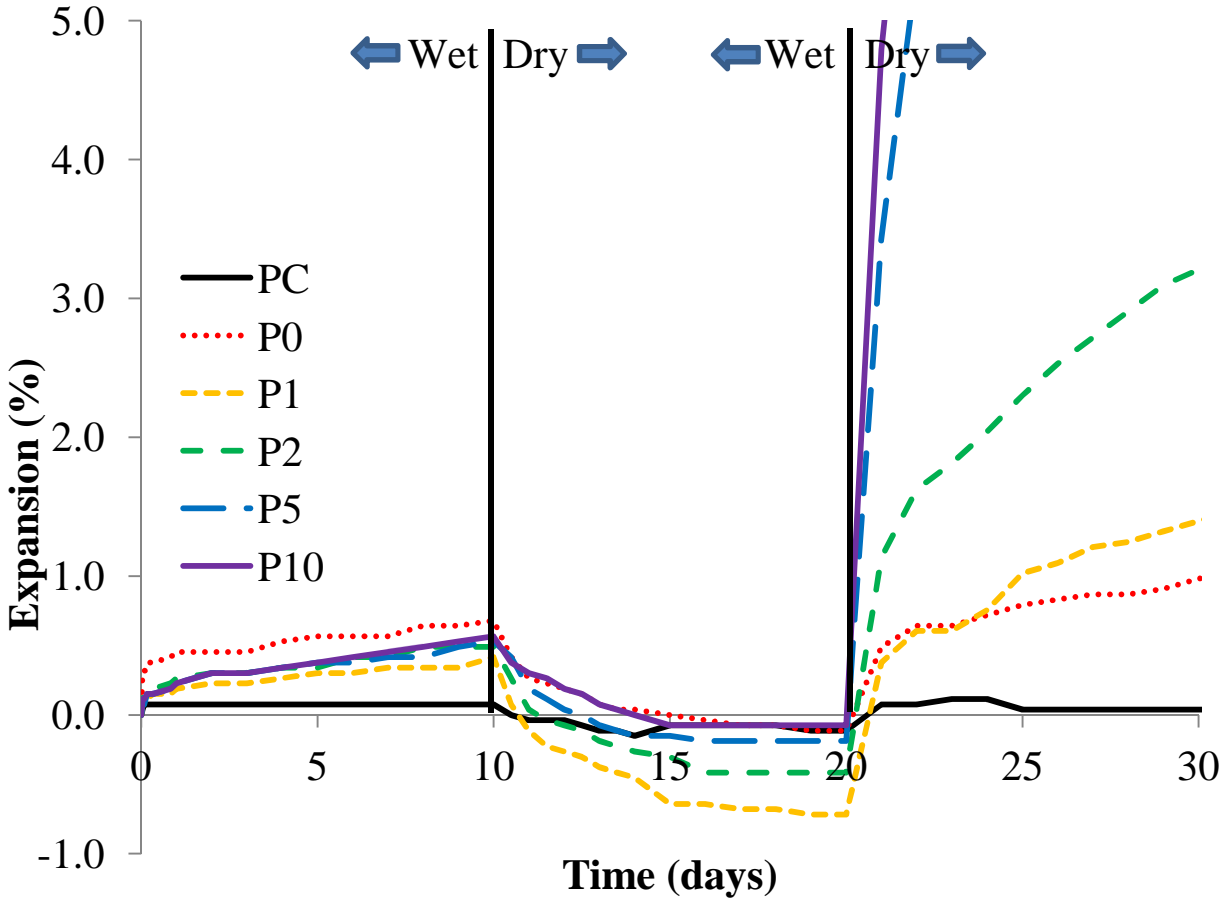
1412
 1413 Figure 26: Influence of increasing CH on the rate of heat flow due to C_4A_3 hydration with 15%
 1414 C_2S .

1415 In the soft X-ray microscopy experiments, gelatinous hydrates formed on what is most likely an
 1416 anhydrous C_4A_3 core, followed by crystalline hydrates growing out radially. This is consistent
 1417 with the reaction rims around C_4A_3 grains observed by Chen et al. [27] and Ogawa and Roy
 1418 [156]. Moreover, the observations lend visual evidence to the confined volumetric expansion
 1419 theory for CSA cements and is consistent with expansion mechanism of cement hydrating
 1420 discussed by Scherer [98] where a cement grain is coated in a crust of hydration products and
 1421 when the core continues to hydrate the crust must crack to accommodate the volume increase
 1422 that results from hydration. Many such microscopic hydration product crusts cracking and
 1423 expanding outward due to the volume increase of the hydration products and the crystallization
 1424 pressures could result in the expansion observed in the cement paste.

1425 4.2.3 Dimensional Stability

1426 All pastes showed the tendency to expand in water with length increases of approximately 0.5%
 1427 at 10 days (Figure 27). After 10 days when the pastes were allowed to dry in ambient

1428 conditions, the pastes with less CH showed more contraction than the pastes with more CH;
1429 however, this trend did not hold for the sample with no CH. After 10 days of air drying all the
1430 pastes had stopped shrinking and at that time the pastes were again immersed in water. All
1431 pastes resumed expanding. Additionally, the rate of expansion was much higher than during the
1432 initial 10 days of curing in water. The faster rate of expansion is most likely attributed to a
1433 change in the AH_3 . During the early age hydration, AH_3 precipitates out as a gel with additional
1434 water incorporated and could be represented as $AH_3 \cdot H_x$. This gel helps to block pores and limit
1435 water and ion mobility in the hydrating CSA paste microstructure. Upon drying, the $AH_3 \cdot H_x$
1436 loses some of its secondary bonded water and contracts. As the AH_3 contracts and goes through
1437 its leather hard point, it decreases in volume opening up porosity in the CSA matrix and more
1438 effectively glues its surroundings together. Upon reintroduction of water to the pastes, the
1439 unhydrated C_4A_3S cores resume hydration with easier access to the water. The hydration of the
1440 unhydrated cores causes localized volume increases which are restrained by the surrounding
1441 matrix. Stresses generated by the localized volume increases (strains) are relieved by
1442 microcracking around the hydrating C_4A_3S cores. As microcracks coalesce they form
1443 macrocracks which can be observed visually and are evidenced by macroscopic length changes.
1444 The transmission X-ray microscopy experiment provides a probable explanation for why
1445 expansion tended to increase with increasing CH content. Figure 14 shows that C_4A_3S
1446 hydration in an excess of CH develops a globular microstructure at early ages instead of forming
1447 ettringite. This globular microstructure is presumed to be the result of a coating product
1448 forming on the surface of the C_4A_3S grains. The XRD results indicate that this coating product
1449 is most likely a solid solution (SO_4^{2-}/OH^-) AFm phase. The coating is preventing the initial
1450 formation of ettringite causing ettringite to form at later ages. Ettringite forming after the
1451 cement matrix has hardened has been shown to cause expansion. It is proposed that the reason
1452 that prior researchers have correlated CSA expansion with CH content is because of this
1453 mechanism of coating the C_4A_3S surface with a solid solution (SO_4^{2-}/OH^-) AFm phase resulting
1454 in a delay of the ettringite formation. A coating forming on the C_4A_3S surfaces early during
1455 hydration would also be consistent with the confined volumetric expansion theory.
1456 Furthermore, a diffusion barrier forming on C_4A_3S 's surface would inhibit its reaction providing
1457 for additional anhydrous cement to react at later ages to cause expansion. Through particle size
1458 distribution studies, prior researchers have shown that anhydrous C_4A_3S persisting into later
1459 ages is correlated with expansion [27, 28].



1460 Figure 27: Dimensional stability changes with CH content and curing condition.
 1461

1462 **CHAPTER 5: C₄A₃\$ HYDRATION IN THE PRESENCE OF CALCITE**
 1463 **AND VATERITE WITH VARYING GYPSUM**

1464 **5.1 Early-Age Hydration**

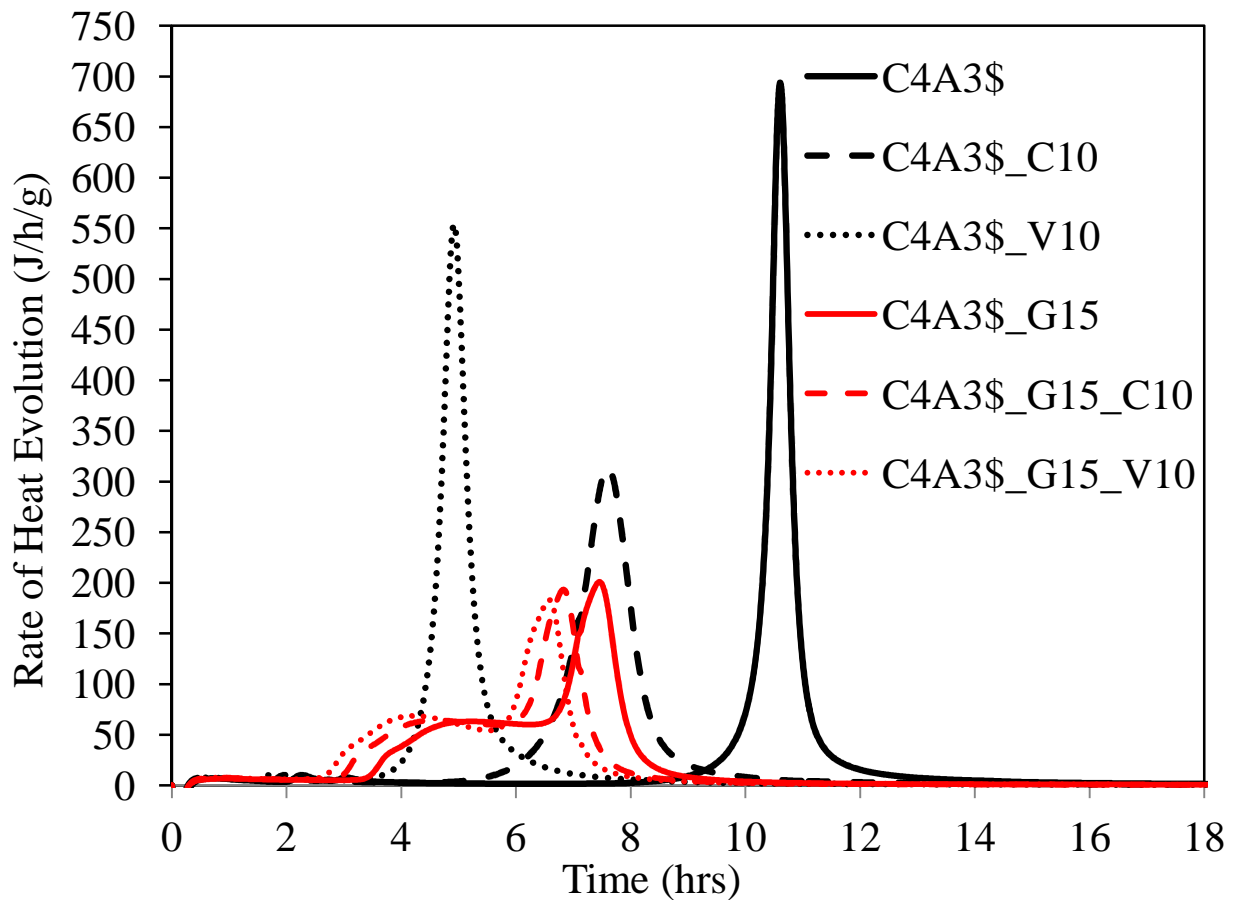
1465 The presence of C\$H₂, calcite and/or vaterite affected the set time of CSA pastes. Table 4
 1466 demonstrates that the inclusion of 15% C\$H₂ cut the initial set time approximately in half and
 1467 the final set time in a third. For all mixes, vaterite reduced the initial set time more than calcite
 1468 did. This is most probably due to vaterite's smaller particle size compared to calcite; vaterite
 1469 and calcite's D₅₀ are 2.0 and 4.5 μm, respectively. In the mixes without C\$H₂, calcite and
 1470 vaterite delayed the final set; whereas, in the mixes with C\$H₂, calcite and vaterite accelerated
 1471 the final set. This would suggest that calcite and vaterite act as better nucleation sites for
 1472 ettringite than monosulfate. Both with and without C\$H₂, the final set times for the mixes with
 1473 calcite were slightly less than the mixes with vaterite, which is a reversal from the initial set
 1474 trend.

1475
 1476

1477 Table 4: Set times for C₄A₃\$ with varying replacements.

Sample	Initial Set (min)	Final Set (min)
C4A3\$	34	126
C4A3\$_C10	29	148
C4A3\$_V10	25	150
C4A3\$_G15	18	42
C4A3\$_G15_C10	14	34
C4A3\$_G15_V10	13	37

1478
 1479 Isothermal conduction calorimetry (Figure 28) showed that calcium carbonates caused the
 1480 maximal rate of heat evolution to occur earlier than for the mixes without calcium carbonates.
 1481 Vaterite had a stronger effect than calcite, and this acceleratory effect on heat evolution was
 1482 more pronounced in the mixes without C\$H₂. This is consistent with calcium carbonates
 1483 reducing the initial set times.
 1484



1485
 1486 Figure 28: Rate of heat evolution for C₄A₃\$ with varying replacements.

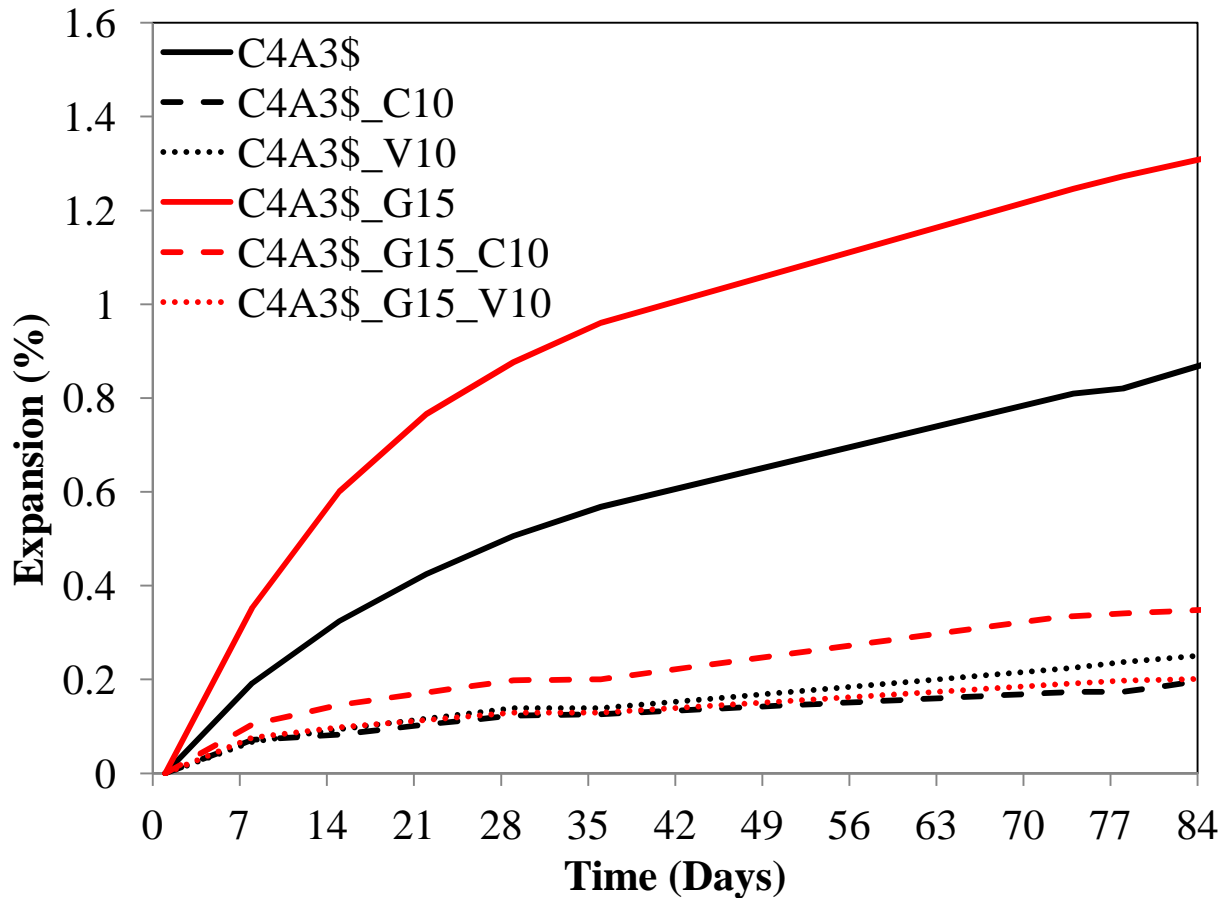
1487 **5.2 Mechanical Properties**

1488 At 1 d, including 15% C\$H_2\$ in the mix doubled the compressive strength of the mortars without
 1489 calcium carbonates, see Table 5. A 10% replacement of C₄A₃\$ with calcite or vaterite increases
 1490 the 1 d strength of the mortars containing C\$H_2\$. Vaterite had a more pronounced effect on 1 d
 1491 compressive strength than calcite. The mortars without C\$H_2\$ experienced decreases in 1 d
 1492 strength with calcite and vaterite replacements; the decrease was less pronounced for
 1493 C4A3\$_G0_V10\$ than for C4A3\$_G0_C10\$. At 1 d, the pure C₄A₃\$ mix has achieved its
 1494 maximum strength; however, C4A3\$_V10\$ continued to gain strength through 28 d then loses
 1495 7% of its strength at 84 d. Additionally, C4A3\$_C10\$ had a slower rate of strength gain than
 1496 C4A3\$_V10\$ and continued to gain strength through 84 d. C4A3\$_V10\$ achieved its maximum
 1497 strength of 45 GPa at 28 d, and C4A3\$_C10\$ achieved its maximum strength of 46 GPa at 84 d.
 1498 The timing of these maximal strengths will be further explained by XRD and DTA later. For
 1499 the mixes with C\$H_2\$, the discussion turns from increases in strength to reductions in
 1500 compressive strength losses. All mixes with C\$H_2\$ lost strength after 1 d. Between 1 and 84 d,
 1501 C4A3\$_G15\$, C4A3\$_G15_C10\$, and C4A3\$_G15_V10\$ lost 37, 20, and 13% of their strengths,
 1502 respectively. The differences in strength losses can in part be explained by the results of the
 1503 dimensional stability tests.

1504
 1505 Table 5: Compressive strength development of mortar cubes with time.

Time (Days)	C4A3\$ Strength (MPa)	C4A3\$_C10\$ Strength (MPa)	C4A3\$_V10\$ Strength (MPa)	C4A3\$_G15\$ Strength (MPa)	C4A3\$_G15_C10\$ Strength (MPa)	C4A3\$_G15_V10\$ Strength (MPa)
1	41 (1)	33 (5)	38 (5)	52 (5)	55 (4)	60 (8)
7	39 (5)	39 (5)	39 (5)	49 (6)	47 (7)	51 (9)
28	40 (1)	41 (5)	45 (5)	39 (3)	46 (3)	49 (6)
84	40 (5)	46 (5)	42 (4)	33 (2)	44 (5)	52 (4)

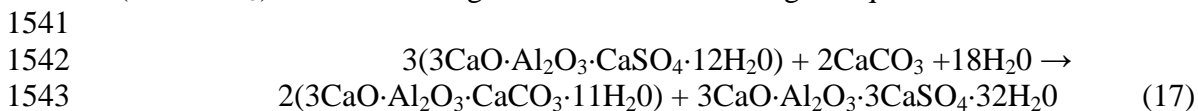
1506
 1507 C₄A₃\$ replacements with 10% calcium carbonates reduced the amount of expansion through 84
 1508 d in both the mixes with and without C\$H_2\$ (Figure 29). For C4A3\$_G15_C10\$ and
 1509 C4A3\$_G15_V10\$, the expansion was reduced approximately six fold compared to
 1510 C4A3\$_G15\$. C4A3\$_G15\$ expanded significantly more than C4A3\$, which is consistent with
 1511 prior research that shows expansion in CSA cements generally increases with increasing
 1512 calcium sulfate contents [8, 27, 90]. However, it is interesting to note that the pure CSA mortar
 1513 without any C\$H_2\$ or calcium carbonates expanded 0.9% by 84 d of hydration. XRD results
 1514 (Table 6) will later show that this mortar would contain little ettringite, which is the phase
 1515 normally assigned blame for deleterious expansion. The expansion of a CSA mortar without
 1516 additional ettringite production or without any of the fine/“colloidal” ettringite found during
 1517 hydration in the presence of hydroxides [150], strongly supports the confined volumetric
 1518 expansion theory for CSA cements [98]; however, the ability for AFm and AFt phases to
 1519 accommodate variable water contents could certainly play a role in expansion due to the uptake
 1520 of externally supplied water resulting in a volume increase. Scherer [98] explains how the
 1521 continued reaction of an anhydrous clinker core that is confined by hydration products could
 1522 result in localized volume increases and cracking. When aggregated, these micro volume
 1523 changes would result in macro dimension changes.



1525 Figure 29: Dimensional stability of C₄A₃\$ with varying replacements.
1526

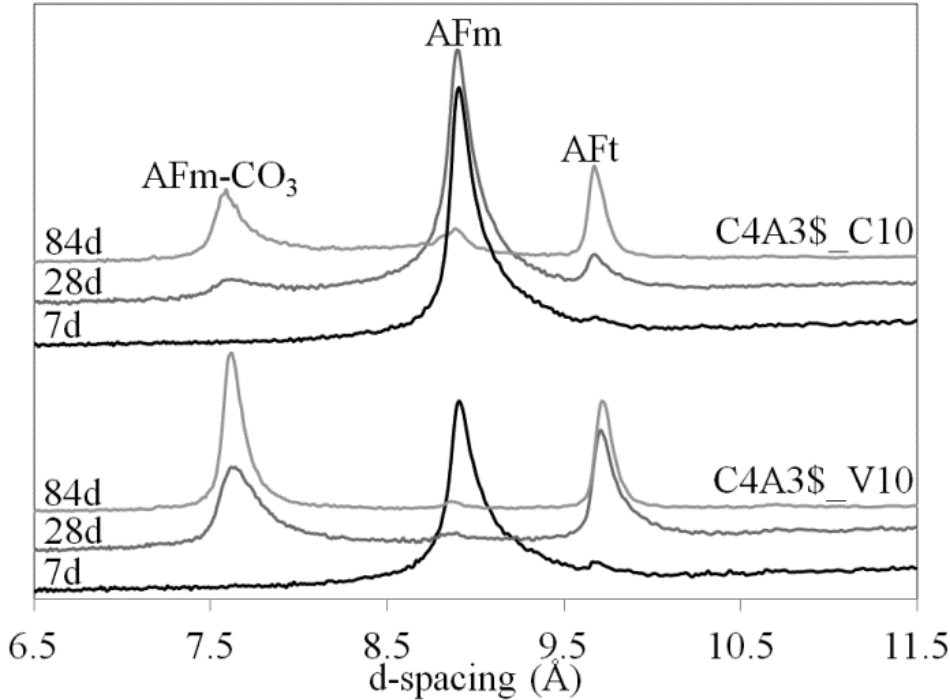
1527 5.3 Chemical Reactions

1528 Figure 30 shows a highlighted region of the XRD plots showing the monosulfate reduction and
1529 ettringite and monocarboaluminate production for C₄A₃\$_C10\$ and C₄A₃\$_V10\$ with time.
1530 Likewise from the figure it is clear that the kinetic of the monocarboaluminate producing
1531 reaction was faster for vaterite than calcite. Table 6 provides a summary of the quantitative
1532 XRD results. All pastes contain anhydrous C₄A₃\$ at 1 d, which is necessary for the confined
1533 volumetric expansion theory. Additionally, the pastes containing C\$H₂ retain C\$H₂ through 7 d
1534 of hydration. Although stoichiometrically the C\$H₂ should have been consumed before 7 d, it
1535 most probably persists due to the system becoming diffusion limited. As expected in the pastes
1536 without C\$H₂, C₄A₃\$ initially reacts to form monosulfate (AFm) and in the pastes with C\$H₂,
1537 C₄A₃\$ reacts with C\$H₂ to form ettringite (AFt). The solubility of calcium carbonates is too
1538 low to take part significantly in the early-age hydration reactions. By 28 d, C₄A₃\$_V10\$ had
1539 reacted 69% of its vaterite and 97% of its monosulfate to form 18% monocarboaluminate
1540 (AFm-CO₃) and 27% ettringite has formed according to Eqn 17.



1544

1545 Calcite is a more stable form of calcium carbonate than vaterite and thus it would be expected to
 1546 react slower with the monosulfate to form monocarboaluminate, and this is evidenced by
 1547 C4A3\$_C10 forming monocarboaluminate at a slower rate than C4A3\$_V10. Likewise,
 1548 C4A3\$_C10's slower rate of monocarboaluminate and ettringite formation corresponded to its
 1549 slower rate of strength gain. It is interesting that although all the mixes with calcium carbonates
 1550 produced significant quantities of ettringite, they expanded less than the mixes without calcium
 1551 carbonate additions that produced much less ettringite over the same time periods. C\$H_2\$ in the
 1552 pastes lead to ettringite formation and reduced the amount of monosulfate formed, thus C\$H_2\$
 1553 reduced the ability of the pastes to react the calcium carbonates and form monocarboaluminate.
 1554



1555
 1556 Figure 30: XRD results highlighting monocarboaluminate and ettringite formation with time for
 1557 mixes without C\$H_2\$.

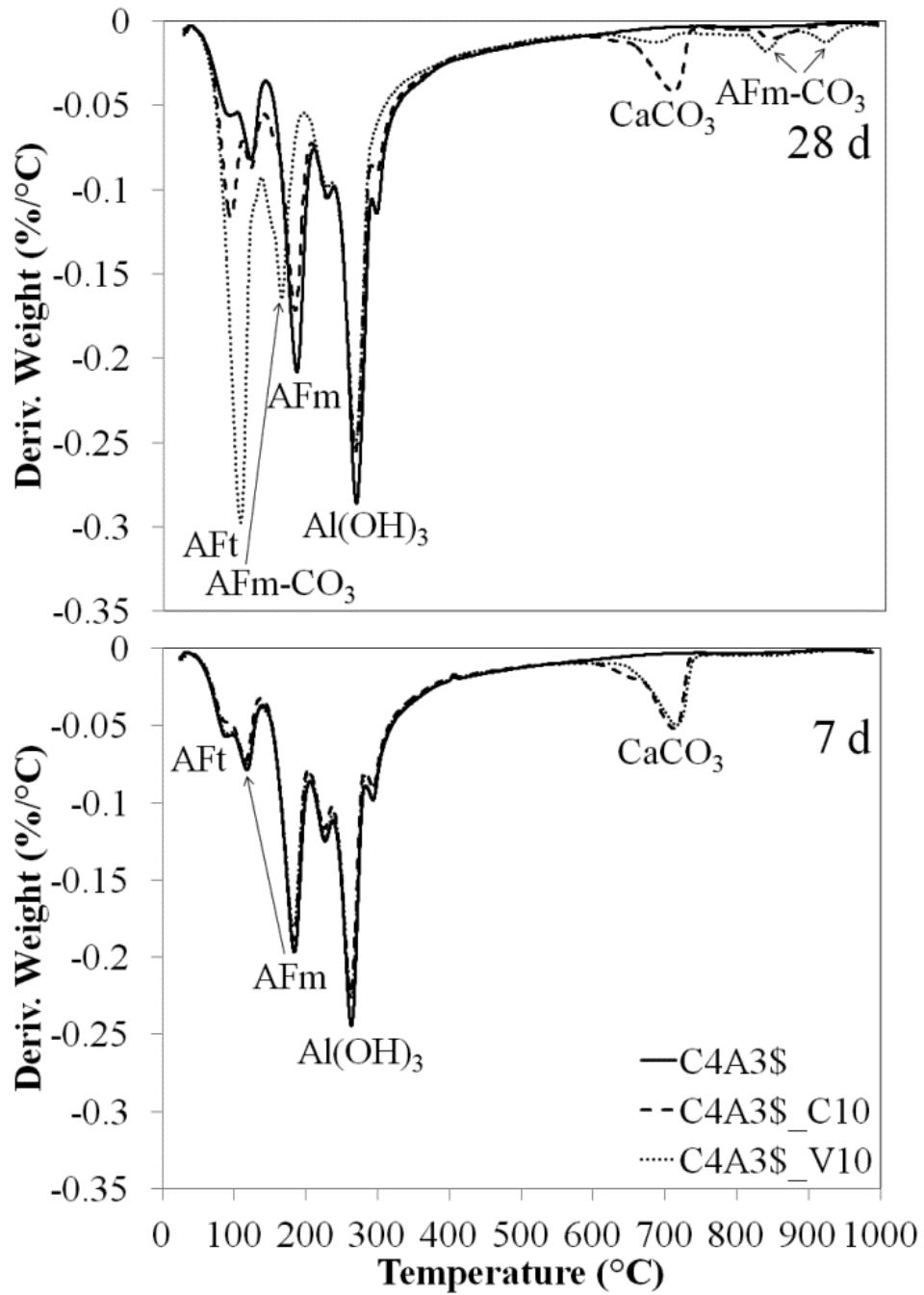
1558 Table 6: Quantitative XRD results in percent.

Paste	Day	C ₄ A ₃ \$	Gyp.	Calc.	Vater.	AFt	AFm	AFm-CO ₃	Gibbs.	Unchar.*
C4A3\$	1	16.2	n/a	n/a	n/a	5.6	29.7	0.0	6.9	41.7
C4A3\$	7	7.8	n/a	n/a	n/a	4.8	28.7	0.0	7.3	51.4
C4A3\$	28	2.7	n/a	n/a	n/a	4.6	42.4	0.0	10.0	40.4
C4A3\$	84	1.4	n/a	n/a	n/a	5.0	39.9	0.0	8.2	45.4
C4A3\$_C10	1	11.7	n/a	7.6	n/a	6.3	30.0	0.0	6.6	37.9
C4A3\$_C10	7	6.4	n/a	7.6	n/a	5.0	31.1	1.9	7.6	40.4
C4A3\$_C10	28	2.6	n/a	6.8	n/a	10.2	28.6	5.6	8.6	37.7
C4A3\$_C10	84	2.3	n/a	3.8	n/a	27.4	5.5	17.0	6.3	37.7
C4A3\$_V10	1	10.1	n/a	0.4	5.9	4.7	27.0	0.0	6.5	45.4
C4A3\$_V10	7	6.2	n/a	0.7	6.1	5.8	24.9	2.1	7.6	46.7
C4A3\$_V10	28	5.1	n/a	0.7	1.8	26.6	0.8	18.1	7.2	39.8
C4A3\$_V10	84	2.5	n/a	0.3	1.1	31.8	0.6	25.7	5.7	32.3
C4A3\$_G15	1	20.7	2.6	n/a	n/a	35.4	2.8	0.0	4.4	34.1
C4A3\$_G15	7	14.9	2.0	n/a	n/a	33.7	3.9	0.0	4.2	41.3
C4A3\$_G15	28	4.1	0.0	n/a	n/a	33.5	9.4	0.0	7.7	45.3
C4A3\$_G15	84	1.0	0.0	n/a	n/a	36.8	12.7	0.0	6.9	42.6
C4A3\$_G15_C10	1	15.0	2.1	7.1	n/a	37.0	2.7	0.0	3.3	32.8
C4A3\$_G15_C10	7	11.3	1.4	6.9	n/a	34.2	3.7	1.4	4.3	36.7
C4A3\$_G15_C10	28	3.0	0.0	5.3	n/a	35.9	1.0	3.9	5.3	45.6
C4A3\$_G15_C10	84	1.8	0.0	5.1	n/a	45.2	0.7	9.0	5.7	32.6
C4A3\$_G15_V10	1	16.7	2.7	0.0	5.1	33.0	1.0	0.0	3.1	38.4
C4A3\$_G15_V10	7	13.7	1.9	0.2	5.7	35.0	2.2	2.6	4.7	34.0
C4A3\$_G15_V10	28	3.8	0.0	0.4	3.7	41.4	1.2	8.1	5.2	36.1
C4A3\$_G15_V10	84	1.2	0.0	0.4	3.3	46.5	0.4	11.8	5.8	30.6

1559 *Includes amorphous material (mainly Al(OH)₃) and contributions from AFm phases with
 1560 variable d-spacings due to variable interlayer molecules/ions.

1561
 1562 Thermal analysis confirms the trends established by XRD. The DTA results in Figure 31 show
 1563 that at 7 d of hydration the hydrated phases for C4A3\$, C4A3\$_C10 and C4A3\$_V10 were
 1564 monosulfate and aluminum hydroxide and calcium carbonate was still mainly unreacted. At 28
 1565 d of hydration, C4A3\$_V10 had reacted more of its calcium carbonate and monosulfate and
 1566 produced more ettringite and monocarboaluminate than C4A3\$_C10. Finally, the absence of
 1567 hemicarboaluminate in all samples can probably be attributed to the low hydroxide
 1568 concentration present in our system.

1569



1570
1571

Figure 31: DTA results for specimens without C\$H_2\$ at 7 and 28 d.

1572 **CHAPTER 6: CONCLUSION**

1573

1574 Rietveld refinements showed the orthorhombic crystal structure [35] to best match the observed
1575 peak intensities and positions for pure C_4A_3 ; however, a future single crystal study is still
1576 needed to confirm/identify the actual space group and symmetries of the crystal structure. A
1577 high-pressure synchrotron XRD experiment was successfully carried out on C_4A_3 at the
1578 Advanced Light Source. The isothermal bulk modulus of C_4A_3 was found to be 69(6) GPa.
1579 Whether the orthorhombic unit-cell or cubic subcell was used to calculate the compressibility of
1580 C_4A_3 had little effect on the value obtained for the bulk modulus. The higher charge of the
1581 anion, SO_4^{2-} , and the cation, Ca^{2+} , of C_4A_3 may contribute to C_4A_3 having a higher bulk
1582 modulus than other sodalites with smaller charged ions such as Na^+ , Cl^- and OH^- . Similarly, by
1583 comparing the bulk modulus of C_4A_3 with $Sr_8(Al_{12}O_{24})(CrO_4)_2$ (72 GPa calculated from [141]),
1584 the effect that the caged ions' sizes have on the lattice compressibility can be observed. As the
1585 size of the caged ions increases, the compressibility of the lattice decreases. C_4A_3 is more
1586 compressible than other cement clinker phases such as C_3A {102(6) GPa} [134] and less
1587 compressible than hydrated cement phases such as ettringite 27(7) GPa [135]. The elastic
1588 constants for many phases in this system are now known such as ettringite and
1589 monocarboaluminate, but determining the elastic properties of amorphous phases in the system
1590 such as AH_3 will be challenging and should be a focus of future research in this area.
1591 Determining the elastic constants of the remaining phases will enable future micromechanical
1592 modeling that will allow expansion models to be validate and will enable cement formulations
1593 to be validated and optimized on the microstructural scale. This will allow high performance
1594 cements and more durable/sustainable cements to be formulated.

1595

1596 CSA cement hydration produces a large amount of crystalline hydrates which contribute to the
1597 cement's early-age strength gain, and how polycrystalline binders develop strength is still not
1598 fully understood. This work demonstrated that the addition of solid CH to a very dilute (50:1)
1599 suspension of C_4A_3 in water pre-saturated with respect to both C_2S and CH tends to reduce
1600 the initial rate of formation of well-crystallized ettringite needles. This reduction in rate seems
1601 to be associated with the stabilization of a layer of hydrates on the surface of the C_4A_3
1602 particles. This hydrate layer has a rather gelatinous appearance but it is also covered with fine
1603 "hairy" outgrowths which are probably fine ettringite. From the composition of the dissolving
1604 C_4A_3 , the ions in the solution, and the XRD results, it seems possible that this initial diffusion
1605 barrier might be a poorly crystalline calcium hydroxyl-sulfoaluminate hydrate.

1606

1607 Relatively large acicular crystals of ettringite (typically of the order of 0.5 μm in width and
1608 ranging from about 2 μm to over 10 μm in length) also appear to have grown from individual
1609 nuclei in the suspension fluid, especially in the system without added CH. An interesting
1610 observation is that many of these acicular crystals are joined together in the form of stellate
1611 clusters which appear to radiate from a central point which we assumed to be either a single
1612 original nucleus or else a particle, presumably of C_4A_3 , that serves as a site for multiple surface
1613 nucleation points. The lack of evidence for any regular form of twinning between the arms of
1614 the stellate clusters suggests that the multiple surface nucleation points hypothesis is the more
1615 likely explanation.

1616
1617 It is hypothesized that such stellate clusters may make an important contribution to the
1618 mechanical properties of hydrated C_4A_3S pastes. It is easy to imagine that an assembly of such
1619 stellate clusters would have significant rigidity due to the interlocking of the “arms” from
1620 adjacent clusters. This type of model is consistent with models that have been proposed to
1621 explain the mechanical strengths of other polycrystalline hydraulic binders, such as hardened
1622 C_3S plasters [112]. It would be interesting to know whether the type of “domain” that is formed
1623 by all of the arms of a single stellate cluster might be identifiable in more dense hydrated paste
1624 systems. Techniques exist nowadays to do this fairly efficiently in certain cases, e.g. by means of
1625 “3D XRD,” coupled with X-ray tomography [157]. The observations of gelatinous hydrates
1626 forming on what is most likely an anhydrous C_4A_3S core, followed by crystalline hydrates
1627 growing out radially is consistent with the confined volumetric expansion theory in CSA
1628 cements.

1629
1630 In the C_4A_3S pastes containing 15% C_3S upon adding increasing amounts of solid CH, the
1631 pastes showed greatly increased rates of hydration at very early ages (evidenced by a dramatic
1632 increase in the rate of heat evolution), producing what XRD showed to be mainly an AFm solid
1633 solution hydrate phase and ettringite. After a brief decline in the rate of heat evolution in the
1634 pastes highest in CH (P5 & P10), C_4A_3S hydrated to form monosulfate as the major phase, since
1635 the C_3S had been depleted during the prior formation of AFm solid solution. Likewise,
1636 increasing CH accelerated the consumption of C_3S and generally decreased the induction
1637 period. At zero and lower levels of CH (P0 – P2) after an induction period, the heat evolution
1638 can be attributed to the continued hydration of C_4A_3S to form ettringite followed by the
1639 formation of monosulfate upon the depletion of C_3S .

1640
1641 The transmission X-ray microscopy experiment provides a probably explanation for why
1642 expansion tended to increase with increasing CH content. C_4A_3S hydration in an excess of CH
1643 develops a globular microstructure at early ages instead of forming ettringite. This globular
1644 microstructure is presumed to be the result of a coating product forming on the surface of the
1645 C_4A_3S grains. The XRD results indicate that this coating product is most likely a solid solution
1646 (SO_4^{2-}/OH^-) AFm phase. The coating is preventing the initial formation of ettringite causing
1647 ettringite to form at later ages. Ettringite forming after the cement matrix has hardened has been
1648 shown to cause expansion. It is proposed that the reason that prior researchers have correlated
1649 CSA expansion with CH content is because of this mechanism of coating the C_4A_3S surface
1650 with a solid solution (SO_4^{2-}/OH^-) AFm phase resulting in a delay of the ettringite formation. A
1651 coating forming on the C_4A_3S surfaces early during hydration would also be consistent with the
1652 confined volumetric expansion theory. Furthermore, a diffusion barrier forming on C_4A_3S 's
1653 surface would inhibit its reaction providing for additional anhydrous cement to react at later
1654 ages to cause expansion, and C_4A_3S persisting into later ages is correlated with expansion [27,
1655 28].

1656
1657 Although CSA cements are promoted as a more environmentally friendly alternative to PC, their
1658 manufacture still consumes a large quantity of resources and energy. One way to reduce CSA
1659 cement's environmental impact is to blend it with calcium carbonate. This study demonstrated
1660 that although calcium carbonate solubility is not high enough to take place in the initial
1661 hydration reactions significantly, calcium carbonate does react with monosulfate to produce

1662 monocarboaluminate and ettringite. The reaction is approximately three times faster for vaterite
1663 than calcite because of vaterite's lower stability. Vaterite showed significant reaction by 28 d;
1664 whereas, calcite showed significant reaction by 84d. C₂H₂ promotes the early age formation of
1665 ettringite at the expense of monosulfate; thus, limiting calcium carbonate's ability to react.
1666

1667 Vaterite and calcite also benefited the mortar's mechanical properties. In the mortars without
1668 C₂H₂, both calcium carbonates reduced mortar expansion and increased the mortar's
1669 compressive strength. The timing of the increase in strength corresponded to when the calcium
1670 carbonate reacted. In the samples with C₂H₂, both calcium carbonates reduced expansion and
1671 reduced the compressive strength lost with time due to expansion. Vaterite was more effective
1672 at mitigating the compressive strength loss than calcite. The mortar without C₂H₂ or calcium
1673 carbonate also expanded significantly despite a low ettringite content (~5%). This strongly
1674 supports that the confined volumetric expansion theory where an anhydrous C₄A₃S core
1675 continues to react with water after being surrounded by a confining matrix causing localized
1676 volume increases and results in a macro expansion. When formulating an industrial CSA
1677 cement, it is imperative to impose restrictions on the amount of C₄A₃S in the clinker, the particle
1678 size distribution of the clinker, w/c and the amount of C₂H₂ added to achieve the desired
1679 amount of expansion. The incorporation of calcium carbonates into CSA cements appears to be
1680 very promising from both an environmental and performance standpoint. Particularly, if a
1681 cement plant could capture its CO₂ emissions and utilize them to make vaterite, the
1682 sustainability of the cement could be greatly advanced.
1683

1684 **REFERENCES**

- 1685
1686 [1] National Oceanic & Atmospheric Administration, Trends in Atmospheric Carbon Dioxide,
1687 <http://www.esrl.noaa.gov/gmd/ccgg/trends/> , accessed 7/11/2013.
- 1688 [2] T.M.L. Wigley, The pre-industrial carbon dioxide level, *Climatic Change* 5 (1983) 315-320.
- 1689 [3] R.A. Feely, C.L. Sabine, K. Lee, W. Berelson, J. Kleypas, V.J. Fabry, F.J. Millero, Impact of
1690 anthropogenic CO₂ on the CaCO₃ system in the oceans. *Science* 305 (2004) 362–366.
- 1691 [4] C.A. Hendriks, E. Worrell, D. deJager, K. Block, P. Riemer, Emission reduction of
1692 greenhouse gases from the cement industry, IEA Greenhouse Gas R&D Programme. Available
1693 from:< <http://www.ieagreen.org.uk/prghgt42.htm> >; 2000.
- 1694 [5] U.S. Environmental Protection Agency. Inventory of U.S. greenhouse gas emissions and
1695 sinks. EPA 430-R-04–003; 4/15/ 2004.
- 1696 [6] P.K. Mehta, P.J.M. Monteiro, *Concrete in the Era of Global Warming and Sustainability*; in
1697 *Concrete Microstructure, Properties, and Materials*, 4th ed., McGraw-Hill, New York, in press.
- 1698 [7] W. Shively, P. Bishop, D. Gress and T. Brown, Leaching tests of heavy metals stabilized
1699 with portland cement, *J. Water Pollution Control Federation* 58 (1986) 234-241.
- 1700 [8] F.P. Glasser, L. Zhang, High-Performance cement matrices based on calcium sulfoaluminate-
1701 belite compositions, *Cem. Concr. Res.* 31 (2001) 1881-1886.
- 1702 [9] P.K. Mehta, Investigation on energy-saving cements, *World Cem. Technol.* 11 (1980) 167-
1703 177.
- 1704 [10] I.A. Chen, M.C.G. Juenger, Incorporation of coal combustion residuals into calcium
1705 sulfoaluminate-belite cement clinkers, *Cem. Concr. Res.* 34 (2012) 893-902.
- 1706 [11] S. Sahu, J. Majling, Preparation of sulphoaluminate belite cement from fly ash, *Cem. Concr.*
1707 *Res.* 24(1999) 1065–1072.
- 1708 [12] P. Arjunan, M.R. Silsbee, D.M. Roy, Sulfoaluminate-belite cement from low calcium fly
1709 ash and sulfur-rich and other industrial by-products, *Cem. Concr. Res.* 29 (1999) 1305–1311.
- 1710 [13] K. Wu, H. Shi, X. Guo, Utilization of municipal solid waste incineration fly ash for
1711 sulfoaluminate cement clinker production, *Waste Manage.* 31 (2011) 2001–2008.
- 1712 [14] J. Beretka, B. de Vito, L. Santoro, N. Sherman, G.L. Valenti, Hydraulic behavior of calcium
1713 sulfoaluminate-based cements derived from industrial process wastes, *Cem. Concr. Res.* 23
1714 (1993) 1205–1214.

- 1715 [15] M. Singh, S.N. Upadhyay, P.M. Prasad, Preparation of special cements from red mud,
1716 Waste Manage. 16 (1996) 665-670.
- 1717 [16] G. Bernardo, M. Marroccoli, F. Montagnaro, G.L. Valenti, Use of fluidized bed combustion
1718 wastes for the synthesis of low energy cements, Proc. 11th Int. Congr. Chem. Cem., Durban,
1719 South Africa, 2003, vol. III, pp. 1227-1236.
- 1720 [17] M. Marroccoli, F. Montagnaro, M. Nobili, A. Telesca, G. L. Valenti, Synthesis, hydration
1721 properties and environmentally friendly features of calcium sulfoaluminate cements, Proc. 12th
1722 Int. Congr. Chem. Cem., Montréal, Canada, 2007, paper W3-11.2.
- 1723 [18] M.L. Pace, A. Telesca, M. Marroccoli, G.L. Valenti, Use of industrial byproducts as
1724 alumina sources for the synthesis of calcium sulfoaluminate cements, Environ. Sci. Technol. 45
1725 (2011) 6124-6128.
- 1726 [19] P.K. Mehta, P.J.M. Monteiro, Hydraulic cements; pp. 238-239 in Concrete Microstructure,
1727 Properties, and Materials, 3rd ed., McGraw-Hill, New York, 2006.
- 1728 [20] A. Klein, Calciumaluminosulfate and expansive cements containing same, US Patent No. 3,
1729 155, 526, 1963, 4 pp.
- 1730 [21] G. C. Bye, Portland Cement 2nd Ed, Thomas Telford, London, 1999, p 206.
- 1731 [22] Y. Wang, M. Su, The third cement series in China, World Cem. 25(8) (1997) 6-10.
- 1732 [23] Y.M. Wang, M.Z. Su, L. Zhang, Sulphoaluminate Cement, Peking, China, Peking
1733 University Press (1990)
- 1734 [24] L. Zhang, M. Su, Y. Wang, Development of the use of sulfo- and ferroaluminate cements in
1735 China, Adv. Cem. Res. 11 (1999) 15-21.
- 1736 [25] J. Diao, Z. Xin, Q. Zhang, Production and Application of Sulfo-aluminate Cement in China,
1737 Beijing Industrial Construction Materials Press, Beijing, 2006.
- 1738 [26] I. Odler, Cements containing calcium sulfoaluminate; pp. 69-87 in Special Inorganic
1739 Cements, 3rd ed., E & FN Spon, London, 2000.
- 1740 [27] I.A. Chen, C.W. Hargis, M.C.G. Juenger, Understanding expansion in calcium
1741 sulfoaluminate-belite cements, Cem. Concr. Res. 42 (2012) 51-60.
- 1742 [28] M. Cohen, C. Richards, Effects of the particle sizes of expansive clinker on strength-
1743 expansion characteristics of Type K expansive cements, Cem. Concr. Res. 12 (1982) 717 – 725.
- 1744 [29] J. Beretka, M. Marroccoli, N. Sherman, G.L. Valenti, The influence of $C_4A_3\bar{S}$ content and
1745 w/s ratio on the performance of calcium sulfoaluminate-based cements, Cem. Concr. Res. 26

- 1746 (1996) 1673-1681.
- 1747 [30] L. Pelletier, F. Winnefeld, B. Lothenbach, The ternary system portland cement-calcium
1748 sulphoaluminate clinker-anhydrite: hydration mechanism and mortar properties, *Cem. Concr.*
1749 *Compos.* 32 (2010) 497-507.
- 1750 [31] M.C.G. Juenger, F. Winnefeld, J.L. Provis, J.H. Ideker, Advances in alternative
1751 cementitious binders, *Cem. Concr. Res.* 41 (12) (2011) 1232-1243.
- 1752 [32] L. Wang, F.P. Glasser, Hydration of calcium sulfoaluminate cements, *Adv. Cem. Res.* 8
1753 (1996) 127-134.
- 1754 [33] P.E. Halstead, A.E. Moore, The composition and crystallography of an anhydrous calcium
1755 aluminosulphate occurring in expanding cement, *J. Appl. Chem.* 12 (1962) 413-417.
- 1756 [34] H. Saalfeld, W. Depmeier, Silicon-Free compounds with sodalite structure, *Kristall und*
1757 *Technik* 7 (1972) 229-233.
- 1758 [35] N.J. Calos, C.H.L. Kennard, A.K. Whittaker, R.L. Davis, Structure of calcium aluminate
1759 sulfate $\text{Ca}_4\text{Al}_6\text{O}_{16}\text{S}$, *J. Solid State Chem.* 119 (1995) 1-7.
- 1760 [36] Z. Peixing, C. Yimin, S. Liping, Z. Guanying, H. Wenmei, W. Jianguo, The crystal structure
1761 of $\text{C}_4\text{A}_3\bar{\text{S}}$, *Proc. 9th ICCG Vol. 3, New Delhi, India, 1992*, pp. 201-208.
- 1762 [37] I. Krstanović, A. Radaković, Lj. Karanović, X-ray powder data for $\text{Ca}_4\text{Al}_6\text{O}_{12}\text{SO}_4$, *Powder*
1763 *Diffraction* 7 (1) (1992) 47-48.
- 1764 [38] T.A. Ragozina, Reaction of calcium sulphate with aluminate at 1200°C, *Zh. Prikl. Khim.* 30
1765 (1957) 1682.
- 1766 [39] A. Klein, C.E. Troxell, Studies of calcium sulfoaluminate admixtures for expansive
1767 cements, *Proc. A.S.T.M.* 58 (1958) 986-1008.
- 1768 [40] N. Fukuda, On the constitution of sulfo-aluminous clinker, *Bull. Chem. Soc. Japan* 34 (1961)
1769 138-139.
- 1770 [41] W. Depmeier, Aluminate sodalites – a family with strained structures and ferroic phase
1771 transitions, *Phys. Chem. Minerals* 15 (1988) 419-426.
- 1772 [42] R. Kondo, The synthesis and crystallography of a group of new compounds belonging to the
1773 hauyne type structure, *J. Ceram. Assoc. Japan* 73 (1965) 1-8.
- 1774 [43] R.X. Fischer, W.H. Baur, Symmetry relationships of sodalite (SOD) – type crystal
1775 structures, *Z. Kristallogr.* 224 (2009) 185-197.

- 1776 [44] X. Feng, G. Liao, S. Long, On the structure and the hydration rate of $3\text{CaO}\cdot 3\text{Al}_2\text{O}_3\cdot \text{CaSO}_4$,
1777 *Il Cemento* 88(1) (1991) 29-35.
- 1778 [45] Y.G. Wang, H.Q. Ye, K.H. Kuo, X.J. Feng, G.L. Lao, S.Z. Long, Electron diffraction and
1779 HREM studies of the new phase and superstructures in $\text{Ca}_4\text{Al}_6\text{SO}_{16}$, *J. Mat. Sci.* 25 (1990) 5147-
1780 5156.
- 1781 [46] Y.G. Wang, H.Q. Ye, K.H. Kuo, X.J. Feng, G.L. Lao, S.Z. Long, Electron microscopy of
1782 domains in $\text{Ca}_4\text{Al}_6\text{SO}_{16}$, *J. Mat. Sci. Let.* 9 (1990) 997-999.
- 1783 [47] Y.G. Wang, H.Q. Ye, K.H. Kuo, X.J. Feng, G.L. Lao, S.Z. Long, An HREM study of
1784 domain structures and grain boundaries in $\text{Ca}_4\text{Al}_6\text{SO}_{16}$, *J. Mat. Sci.* 26 (1991) 814-820.
- 1785 [48] Y.G. Wang, H.Q. Ye, K.H. Kuo, X.J. Feng, G.L. Lao, S.Z. Long, High-resolution electron
1786 microscopy of the twinning and intergrowth in $\text{Ca}_4\text{Al}_6\text{SO}_{16}$ and $\text{Ca}_3\text{SrAl}_6\text{SO}_{16}$, *J. Mat. Sci.* 26
1787 (1991) 6325-6330.
- 1788 [49] D.B. Williams, C.B. Carter, Phase-contrast images; pp. 392-6 in *Transmission Electron*
1789 *Microscopy: a Textbook for Materials Science*, Springer, New York, 2009.
- 1790 [50] P. Mondal, J. W. Jeffery, The crystal structure of tricalcium aluminate, $\text{Ca}_3\text{Al}_2\text{O}_6$. *Acta*
1791 *Cryst. B* 31 (1975) 689-697.
- 1792 [51] W. Depmeier, Remarks on symmetries occurring in the sodalite family, *Z. Kristallogr.* 199
1793 (1992) 75-89.
- 1794 [52] K. Ikeda, K. Kishimoto, H. Shima, Structure refinement of calcium sulfoaluminate, $\text{C}_4\text{A}_3\bar{\text{S}}$,
1795 with emphasis to Oxygen Deficiency, *Cem. Concr. Res.* (5) 26 (1996) 743-748.
- 1796 [53] G. Álvarez-Pinazo, A. Cuesta, M. García-Maté, I. Santacruz, E.R. Losilla, A.G. De la Torre,
1797 L. León-Reina, M.A.G. Aranda, Rietveld quantitative phase analysis of Yeelimite-containing
1798 cements, *Cem. Concr. Res.* 42 (2012) 960-971.
- 1799 [54] H.S. Kim, G.C. Han, J.W. Ahn, K.H. Cho, H.C. Cho, Identification of calcium
1800 sulfoaluminate formation between alunite and limestone, *Sensors* 9 (2009) 5059-5067.
- 1801 [55] J.J. van der Klink, W.S. Veeman, H. Schmid, Al NMR studies of the aluminate sodalites
1802 $\text{Sr}_8[\text{Al}_{12}\text{O}_{24}](\text{CrO}_4)_2$ and $\text{Ca}_8[\text{Al}_{12}\text{O}_{24}](\text{WO}_4)_2$, *J. Phys. Chem.* 95 (1991) 1508-1511.
- 1803 [56] C.M.B. Henderson, D. Taylor, Infrared spectra of aluminogermanate- and aluminate-
1804 sodalites and a re-examination of the relationship between T-O bond length, T-O-T angle and the
1805 position of the main I.R. absorption band for compounds with framework structures,
1806 *Spectrochimica Acta* A35 (1979) 929-935.
- 1807 [57] X. Hu, W. Depmeier, Pitfalls in the X-ray structure determination of pseudosymmetric

- 1808 sodalites, and possibly zeolites, *Z. Kristallogr.* 201 (1992) 99-111.
- 1809 [58] W. Depmeier, Phase transitions and modulated structures in aluminite sodalites, *J. Alloys*
1810 *Compd.* 188 (1992) 21-26.
- 1811 [59] W. Depmeier, Tetragonal tetrahedra distortions in cubic sodalite frameworks, *Acta Cryst.*
1812 B40 (1984) 185-191.
- 1813 [60] M.E. Brenchley, M.T. Weller, Synthesis and structure of sulfide aluminite sodalites, *J.*
1814 *Mater. Chem.* 2 (10) (1992) 1003-1005.
- 1815 [61] G.S. Li, G. Walenta, E.M. Gartner, Formation and hydration of low-CO₂ cements based on
1816 belite, calcium sulfoaluminate and calcium aluminoferrite, *Proc. 12th ICCO*, Montreal, Canada,
1817 2007.
- 1818 [62] V. Kasselouri, P. Tsakiridis, Ch. Malami, B. Georgali, C. Alexandridou, A study on the
1819 hydration products of a non-expansive sulfoaluminate cement, *Cem. Concr. Res.* 25 (1995)
1820 1726-1736.
- 1821 [63] F. Winnefeld, S. Barlag, Influence of calcium sulfate and calcium hydroxide on the
1822 hydration of calcium sulfoaluminate clinker, *ZKG Int.* 12 (2009) 42-53.
- 1823 [64] C.W. Hargis, A.P. Kirchheim, P.J.M. Monteiro, E.M. Gartner, Early age hydration of
1824 calcium sulfoaluminate (synthetic ye'elinite, C₄A₃S̄) in the presence of gypsum and varying
1825 amounts of calcium hydroxide, *Cem. Concr. Res.* 48 (2013) 105-115.
- 1826 [65] T. Matschei, B. Lothenbach, F.P. Glasser, The role of calcium carbonate in cement
1827 hydration, *Cem. Concr. Res.* 37 (2007) 551-558.
- 1828 [66] P. Lawrence, M. Cyr, E. Ringot, Mineral admixtures in mortars —effect of inert materials
1829 on short-term hydration, *Cem. Concr. Res.* 33(12) (2003) 1939-1947.
- 1830 [67] M. Cyr, P. Lawrence, E. Ringot, Mineral admixtures in mortars —quantification of the
1831 physical effects of inert materials on short-term hydration, *Cem. Concr. Res.* 35 (2005) 719-
1832 730.
- 1833 [68] P. Lawrence, M. Cyr, E. Ringot, Mineral admixtures in mortars —effect of type, amount
1834 and fineness of fine admixtures on compressive strength, *Cem. Concr. Res.* 35 (2005) 1092-
1835 1105.
- 1836 [69] M. Cyr, P. Lawrence, E. Ringot, Efficiency of mineral admixtures in mortars: quantification
1837 of the physical and chemical effects of fine admixtures in relation with compressive strength,
1838 *Cem. Concr. Res.* 36 (2006) 264-277.
- 1839 [70] L. Pelletier-Chaignat, F. Winnefeld, B. Lothenbach, C. J. Müller, Beneficial use of

- 1840 limestone filler with calcium sulfoaluminate cement, *Constr. Build. Mater.* 26 (2012) 619–627.
- 1841 [71] C.S. Neto, V.C. Campiteli, The Influence of limestone additions on the rheological
1842 properties and water retention value of portland cement slurries, pp.24-29 in: P. Klieger and R.D.
1843 Hooton (Eds.), *Carbonate Additions to Cement*, ASTM STP 1064, American Society for Testing
1844 and Materials, Philadelphia, 1990.
- 1845 [72] A.P. Barker, J.D. Matthews, Heat release characteristics of limestone-filled cements, paper
1846 presented at a BRE seminar on Performance of Limestone-filled Cements, Nov. 1989.
- 1847 [73] M. Schmidt, Cement with interground additives—capabilities and environmental relief, part
1848 2, *Zement-Kalk-Gips* 45 (6) (1992) 296-301.
- 1849 [74] E.J. Sellevold, D.H. Bager, E. Klitgaard-Jensen, T. Knudsen, Silica fume-cement pastes:
1850 hydration and pore structure, pp. 19-50 in: *Condensed Silica Fume in Concrete*, Institutt for
1851 Bygningmateriellære, Norges Tekniske Høgskole, Universitetet i Trondheim, Trondheim,
1852 Norway, BML 82.610, Feb. 1982.
- 1853 [75] V.C. Campiteli, M.C. Florindo, The influence of limestone additions on optimum sulfur
1854 trioxide content in portland cements, pp.30-40 in : P. Klieger and R.D. Hooton (Eds.), *Carbonate*
1855 *Additions to Cement*, ASTM STP 1064, American Society for Testing and Materials,
1856 Philadelphia, 1990.
- 1857 [76] L.D. Adams, R.M. Race, Effect of limestone additions upon drying shrinkage of portland
1858 cement mortar, *Carbonate Additions to Cement*, pp. 41-50 in: P. Klieger and R.D. Hooton (Eds.),
1859 *Carbonate Additions to Cement*, ASTM STP 1064, American Society for Testing and Materials,
1860 Philadelphia, 1990.
- 1861 [77] A.P. Barker, D.W. Hobbs, Performance of portland limestone cements in mortar prisms
1862 immersed in sulfate solutions at 5°C, *Cem. Concr. Compos.* 21 (1999) 129-137.
- 1863 [78] L. Zhang, F.P. Glasser, New concretes based on calcium sulfoaluminate cement, pp. 261-
1864 274 in: R.K. Dhir, T.D. Dyer (Eds.), *Modern Concrete Materials: Binders, Additions and*
1865 *Admixtures*, Thomas Telford, London, 1999.
- 1866 [79] K. Quillin, Performance of belite-sulfoaluminate cements, *Cem. Concr. Res.* 31 (2001)
1867 1341-1349.
- 1868 [80] V. Zivica, I. Janotka, Chemical resistance of sulfoaluminate belite cement based materials,
1869 *Build. Res. J.* 47 (1999) 117-134.
- 1870 [81] N. Sherman, J. Beretka, L. Santoro, G.L. Valenti, Long-Term behaviour of hydraulic
1871 binders based on calcium sulfoaluminate and calcium sulfosilicate, *Cem. Concr. Res.* 25 (1995)
1872 113-126.
- 1873 [82] E. Gartner, Industrially interesting approaches to “Low-CO₂” cements, *Cem. Concr. Res.*

- 1874 34 (2004) 1489-1498.
- 1875 [83] M. Santhanam, M.D. Cohen, J. Olek, Mechanism of sulfate attack: a fresh look: part 1;
1876 summary of experimental results, *Cem. Concr. Res.* 32 (2002) 915-921.
- 1877 [84] Y. Fu, J.J. Beaudoin, Mechanisms of delayed ettringite formation in portland cement
1878 systems, *ACI Mater. J.* 93 (1996) 327-333.
- 1879 [85] K. Ogawa, D.M. Roy, C_4A_3S hydration, ettringite formation, and its expansion
1880 mechanisms: III. effect of CaO, NaOH, and NaCl; conclusions, *Cem. Concr. Res.* 12 (1982)
1881 247-256.
- 1882 [86] I. Janotka, L. Krajci, S.C. Mojumdar, Performance of sulphoaluminate-belite cement with
1883 high C_4A_3S content, *Ceramics-Silikaty.* 51 (2007) 74-81.
- 1884 [87] D. Min, T. Mingshu, Formation and expansion of ettringite crystals, *Cem. Concr. Res.* 24
1885 (1994) 119-126.
- 1886 [88] G. Bernardo, A. Telesca, G.L. Valenti, A porosimetric study of calcium sulfoaluminate
1887 cement pastes cured at early ages, *Cem. Concr. Res.* 36 (2006) 1042-1047.
- 1888 [89] I. Odler, J. Colan-Subauste, Investigations on cement expansion associated with ettringite
1889 formation, *Cem. Concr. Res.* 29 (1999) 731-735.
- 1890 [90] W. Yanmou, S. Muzhen, Y. Renhe, L. Baoyuan, A quantitative study of paste
1891 microstructures and hydration characters of sulphoaluminate cement, *Proc. 9th ICC*, New Delhi,
1892 India, 1992.
- 1893 [91] A. Klein, Expansive and shrinkage-compensated cements, US Patent 3251701, 1966.
- 1894 [92] W. Kurdowski, A. Thiel, On the role of free calcium oxide in expansive cements, *Cem.*
1895 *Concr. Res.* 11 (1981) 29-40.
- 1896 [93] P.K. Mehta, Mechanism of expansion associated with ettringite formation, *Cem. Concr.*
1897 *Res.* 3 (1973) 1-6.
- 1898 [94] I. Jawed, J. Skalny, Alkalies in cement: a review, *Cem. Concr. Res.* 8 (1978) 37-51.
- 1899 [95] P.K. Mehta, P.J.M. Monteiro, *Concrete Microstructure, Properties, and Materials*, third ed.,
1900 McGraw-Hill, New York, 2006, p. 213.
- 1901 [96] E.J. Garboczi, Stress, displacement, and expansive cracking around a single spherical
1902 aggregate under different expansive conditions, *Cem. Concr. Res.* 27(4) (1997) 495-500.
- 1903 [97] M.D. Cohen, Theories of expansion in sulfoaluminate – type expansive cements: schools of
1904 thought, *Cem. Concr. Res.* 13 (1983) 809-818.

- 1905 [98] G.W. Scherer, Stress from crystallization of salt, *Cem. Concr. Res.* 34 (2004) 1613-1624.
- 1906 [99] C.W. Richards, R.A. Helmuth, Expansive cement concrete — micromechanical models for
1907 free and restrained expansion, Technical Report TR 191, January 1977, 36 pp.
- 1908 [100] M. Ish-Shalom, A. Bentur, Properties of type K expansive cement of pure components,
1909 *Cem. Concr. Res.* 4 (1974) 519-532.
- 1910 [101] M. Ish-Shalom, A. Bentur, Properties of type K expansive cement of pure components – II.
1911 proposed mechanism of ettringite formation and expansion in unrestrained paste of pure
1912 expansive component, *Cem. Concr. Res.* 4 (1974) 709-721.
- 1913 [102] G.L. Kalousek, E. Benton, Mechanism of sea water attack on cement pastes, *J. Am. Concr.*
1914 *Inst.* 67 (1970) 187-192.
- 1915 [103] P.K. Mehta, Mechanism of expansion associated with ettringite formation, *Cem. Concr.*
1916 *Res.* 3 (1973) 1-6.
- 1917 [104] P.K. Mehta, F.J. Hu, Further evidence for expansion of ettringite by water adsorption, *J.*
1918 *Am. Cer. Soc.* 61 (1978) 179-181.
- 1919 [105] Y. Wang, J. Deng, M. Su, An investigation into cement CaO-SiO₂-Al₂O₃-Fe₂O₃-SO₃
1920 system, *Proc. 8th ICCC*, Rio de Janeiro, Brazil, vol. 2, 1986, pp. 300-305.
- 1921 [106] F. Winnefeld, S. Barlag, Calorimetric and thermogravimetric study on the influence of
1922 calcium sulfate on the hydration of ye'elimite, *J. Therm. Anal. Calorim.* 101 (2010) 949–957.
- 1923 [107] M. Su, Y. Wang, L. Zhang, D. Li, Preliminary study on the durability of sulfo/ferro-
1924 aluminate cements, *Proc. 10th ICCC*, Göteborg, Sweden, vol. 4, 1997, 41v029.
- 1925 [108] S. Abdul-Maula, I. Odler, SO₃-rich portland cements: synthesis and strength development,
1926 *Mat. Res. Soc. Symp. Proc.* 245 (1992) 315-320.
- 1927 [109] J. Beretka, L. Santoro, N. Sherman, G.L. Valenti, Synthesis and properties of low energy
1928 cements based on C₄A₃S, *Proc. 9th ICCC*, New Delhi, vol. 3, 1992, pp. 195-200).
- 1929 [110] J. Beretka, N. Sherman, M. Marroccoli, A. Pompo, G. L. Valenti, Effect of composition on
1930 the properties of rapid hardening sulfoaluminate cement, *Proc. 10th ICCC*, Göteborg, Sweden,
1931 vol. 10, 1997, 2ii029.
- 1932 [111] C.K. Park, B. K. Kim, S. Y. Hong, G. Y. Shin. Microstructural change of calcium
1933 sulfoaluminate cement paste due to temperature, *Proc. 10th ICCC*, Göteborg, Sweden, vol. 4,
1934 1997, 41v068.
- 1935 [112] E. M. Gartner, Cohesion and expansion in polycrystalline solids formed by hydration
1936 reactions - the case of gypsum plasters, *Cem. Concr. Res.* 39 (2009) 289–295.

- 1937 [113] D. Biello, Cement from CO₂: a concrete cure for global warming, *Sci. Am.* Aug. 7, 2008,
 1938 <http://www.scientificamerican.com/article.cfm?id=cement-from-carbon-dioxide&sc=rss>,
 1939 accessed 3/29/2013.
- 1940 [114] B. Franke, Bestimmung von calciumoxid und calciumhydroxid neben wasserfreiem und
 1941 wasserhaltigem calciumsilicat, *Z anorg allg Chem.* 247 (1941) 180–184.
- 1942 [115] S. Gross, Occurrence of ye'elimite and ellestadite in an unusual cobble from the “pseudo-
 1943 conglomerate” of the Hatrurim Basin, Israel, *Geol. Surv. Israel, Current Research 1983–84*
 1944 (1984) 1–4.
- 1945 [116] D.A. Silva, P.J.M. Monteiro, Analysis of C₃A hydration using soft X-rays transmission
 1946 microscopy: effect of EVA copolymer, *Cem. Concr. Res.* 35(10) (2005) 2026-2032.
- 1947 [117] P.J.M. Monteiro, A.P. Kirchheim, S. Chae, P. Fischer, A.A. MacDowell, E. Schaible, H.-
 1948 R. Wenk. Characterizing the nano and micro structure of concrete to improve its durability. *Cem.*
 1949 *Concr. Compos.* 31 (2009) 577–584.
- 1950 [118] M. Kunz, A.A. MacDowell, W.A. Caldwell, D. Cambie, R.S. Celestre, E.E. Domning,
 1951 R.M. Duarte, A.E. Gleason, J.M. Glossinger, N. Kelez, D.W. Plate, T. Yu, J.M. Zaugg, H.A.
 1952 Padmore, R. Jeanloz, A.P. Alivisatos, S.M. Clark, A beamline for high pressure studies at the
 1953 Advanced Light Source with a superconducting bending magnet as the source, *J. Synchrotron*
 1954 *Radiat.* 12 (2005) 650–658.
- 1955 [119] H.K. Mao, J. Xu, P.M. Bell, Calibration of the ruby pressure gauge to 800 kbar under
 1956 quasi-hydrostatic conditions, *J. Geophys. Res.* 91 (1986) 4673–4676.
- 1957 [120] A.P. Hammersley, S.O. Svensson, M. Hanfland, A.N. Fitch, D. Hausermann, Two-
 1958 dimensional detector software: From real detector to idealised image or two-theta scan, *High*
 1959 *Pressure Res.* 14 (1996) 235–248.
- 1960 [121] L. Lutterotti, S. Matthies, H.-R. Wenk, A.J. Schultz and J.W. Richardson, Combined
 1961 texture and structure analysis of deformed limestone from time-of-flight neutron diffraction
 1962 spectra, *J. Appl. Phys.* 81 (1997) 594-600.
- 1963 [122] G. Caglioti, A. Paoletti, F.P. Ricci, Choice of collimators for a crystal spectrometer for
 1964 neutron diffraction, *Nucl. Instrum.* 3 (1958) 223-228.
- 1965 [123] H.-R. Wenk, R. Vasin, L. Lutterotti, Rietveld texture analysis from synchrotron diffraction
 1966 images: I. Basic analysis, *Powder Diffr.*, in press.
- 1967 [124] W. Meyer-Ilse, H. Medeck, J. Brown, J. Heck, E.H. Anderson, C. Magowan, A.D. Stead,
 1968 T.W. Ford, R.L. Balhorn, D. Arndt-Jovin, T. Jovin, C. Petersen, D.T. Attwood, X-ray
 1969 microscopy in Berkeley, in: J. Thieme, et al. (Eds.), *X-ray Microscopy and Spectromicroscopy*,
 1970 Springer, Berlin, 1998.

- 1971 [125] Center for X-ray Optics, XM-1 Schematic, <http://cxro.lbl.gov/XM1>, accessed 7/27/2013.
- 1972 [126] J. Goldstein, D. Newbury, D. Joy, C. Lyman, P. Echlin, E. Lifshin, L. Sawyer, J. Michael,
1973 Scanning electron microscopy and X-ray microanalysis, 3rd ed., Springer, New York, pp 217-
1974 220.
- 1975 [127] R.B.V., Dreele, A rapidly filled capillary mount for both dry powder and polycrystalline
1976 slurry samples, *J. Applied Crystallography* 39 (2006) 124-126.
- 1977 [128] A.F. Craievich, A.R. Rodrigues, The Brazilian synchrotron light source, *Hyperfine*
1978 *Interactions* 113 (1998) 465-475.
- 1979 [129] F.F. Ferreira, E. Granado, W. Carvalho Jr., S.W. Kycia, D. Bruno, R. Droppa Jr., X-ray
1980 powder diffraction beamline at D10B of LNLS: application to the Ba₂FeReO₆ double perovskite,
1981 *J. Synchrotron Radiation* 13 (2006) 46-53.
- 1982 [130] ASTM C807-08, Standard Specification for Time of Setting of Hydraulic Cement Mortar
1983 by Modified Vicat Needle, ASTM International, West Conshohocken, PA, (2008) 3 pp.
- 1984 [131] F. Birch, Finite strain isotherm and velocities for single-crystal and polycrystalline NaCl at
1985 high pressures and 300K, *J. Geophys. Res.* 83 (1978) 1257-1268.
- 1986 [132] R. Jeanloz, Finite-strain equation of state for high-pressure phases, *Geophysical Research*
1987 *Letters* 8 (1981) 1219–1222.
- 1988 [133] Y. Sato, S. Akimoto, Hydrostatic compression of four corundum-type compounds:
1989 α -Al₂O₃, V₂O₃, Cr₂O₃, and α -Fe₂O₃, *J. Appl. Phys.* 50 (1979) 5285-5291.
- 1990 [134] J. Moon, S. Yoon, R.M. Wentzcovitch, S.M. Clark, P.J.M. Monteiro, Elastic properties of
1991 tricalcium aluminate from high-pressure experiments and first-principles calculations, *J. Am.*
1992 *Ceram. Soc.* 95(9) (2012) 2972–2978.
- 1993 [135] S.M. Clark, B. Colas, M. Kunz, S. Speziale, P.J.M. Monteiro, Effect of pressure on the
1994 crystal structure of ettringite, *Cem. Concr. Res.* 38 (2008) 19–26.
- 1995 [136] H.E. Petch, The hydrogen positions in portlandite, Ca(OH)₂, as indicated by the electron
1996 distribution, *Acta Crystallogr.* 14 (1961) 950–957.
- 1997 [137] J. Moon, J.E. Oh, M. Balonis, F.P. Glasser, S.M. Clark, P.J.M. Monteiro, High pressure
1998 study of low compressibility tetracalcium aluminum carbonate hydrates
1999 3CaO·Al₂O₃·CaCO₃·11H₂O, *Cem. Concr. Res.* 42 (2011) 105-110.
- 2000 [138] J. Moon, J.E. Oh, M. Balonis, F.P. Glasser, S.M. Clark, P.J.M. Monteiro, Pressure induced
2001 reactions amongst calcium aluminate hydrate phases, *Cem. Concr. Res.* 41(6) (2011) 571-578.
- 2002 [139] R.M. Hazen, Z.D. Sharp, Compressibility of sodalite and scapolite, *Am. Mineral.* 73 (1988)

- 2003 1120–1122.
- 2004 [140] J.E. Oh, J. Moon, M. Mancio, S.M. Clark, P.J.M. Monteiro, Bulk modulus of basic
2005 sodalite, $\text{Na}_8(\text{AlSiO}_4)_6(\text{OH})_2 \cdot \text{H}_2\text{O}$, a possible zeolitic precursor in coal-fly-ash based
2006 geopolymers, *Cem. Concr. Res.* 41 (2011) 107-112.
- 2007 [141] R. Melzer, W. Depmeier, T. Vogt, E. Gering, Neutron and synchrotron radiation high
2008 pressure experiments on aluminate sodalite $\text{Sr}_8(\text{Al}_{12}\text{O}_{24})(\text{CrO}_4)_2$, *Cryst. Res. Technol.* 30 (1995)
2009 767-773.
- 2010 [142] R.D. Shannon, Revised effective ionic radii and systematic studies of interatomic distances
2011 in halides and chalcogenides, *Acta Cryst. A*32 (1976) 751-767.
- 2012 [143] K. Toriumi, Y. Saito, Electron-density distribution in crystals of $\alpha\text{-K}_2\text{CrO}_4$, *Acta Cryst.*
2013 B34 (1978) 3149-3156.
- 2014 [144] L. Pauling, Interatomic distances and bond character in the oxygen acids and related
2015 substances, *J. Phys. Chem.* 56(3) (1952) 361–365.
- 2016 [145] R. Komatsu, N. Mizukoshi, K. Makida, K. Tsukamoto, In-situ observation of ettringite
2017 crystals, *J. Crystal Growth* 311 (2009) 1005-1008.
- 2018 [146] P.K. Mehta, Scanning electron micrographic studies of ettringite formation, *Cem. Concr.*
2019 *Res.* 6 (1976) 169-182.
- 2020 [147] W. Lerch, F.W. Ashton, R.H. Bogue, The sulphoaluminates of calcium, Bureau of
2021 Standards *J. Res.* 2(4) (1929) 715-731.
- 2022 [148] E. Candlot, Properties of cements and hydraulic binders (French), *Bulletin de la Société*
2023 *d'encouragement pour l'industrie nationale* 5(4) (1890) 682-716.
- 2024 [149] M.C.G. Juenger, V.H.R. Lamour, P.J.M. Monteiro, E.M. Gartner, G.P. Denbeaux, Direct
2025 observation of cement hydration by soft X-ray transmission microscopy, *J. Mat. Sci. Let.* 22
2026 (2003) 1335-1337.
- 2027 [150] P.K. Mehta, Effect of lime on hydration of pastes containing gypsum and calcium
2028 aluminates or calcium sulfoaluminate, *J. Am. Ceram. Soc.* 56(6) (1973) 315-319.
- 2029 [151] F. Hanik, I. Kaprálik, A. Garisová, Mechanism of hydration reactions in the system $\text{C}_4\text{A}_3\text{S}-$
2030 $\text{C}\$\text{-CaO-H}_2\text{O}$ referred to hydration of sulfoaluminate cements, *Cem. Concr. Res.* 19 (1989)
2031 671-682.
- 2032 [152] J. Sinkankas, *Mineralogy: a first course*, D. Van Nostrand Company, New Jersey, 1966.
- 2033 [153] T. Matschei, B. Lothenbach, F.P. Glasser, The AFm phase in portland cement, *Cem.*
2034 *Concr. Res.* 37 (2007) 118-130.

- 2035 [154] A. Klein, P.K. Mehta, Nature of hydration products in the system $4\text{CaO}\cdot 3\text{Al}_2\text{O}_3\cdot \text{SO}_3\text{-}$
2036 $\text{CaSO}_4\text{-CaO-H}_2\text{O}$, Proc. 5th Int. Symp. Chem. Cem. Vol. IV, 1969, pp. 336-340.
- 2037 [155] M.T. Palou, J. Majling, Hydration in the system $\text{C}_4\text{A}_3\text{-C}\text{H}_2\text{-CH-H}$, J. Therm. Anal. 46
2038 (1996) 557-563.
- 2039 [156] D.M. Roy and K. Ogawa, C_4A_3 hydration, ettringite formation, and its expansion
2040 mechanism: II. microstructural observation of expansion, Cem. Concr. Res. 12 (1982) 101-109.
- 2041 [157] K. Thornton, H.F. Poulsen, Three-dimensional materials science: an intersection of three-
2042 dimensional reconstructions and simulations, MRS Bulletin 33 (2008) 587-592.